SWANSEA UNIVERSITY

PHD THESIS

Novel approaches to the study of the heavy meson spectrum at finite temperature

Author:

BENJAMIN T. PAGE

Under the supervision of:

PROF. C. R. ALLTON

**Prifysgol Abertawe
Swansea University**

A thesis submitted in fulfilment of the requirements

for the degree of PhD in Physics as outlined by the

DEPARTMENT OF PHYSICS,

FACULTY OF SCIENCE AND ENGINEERING
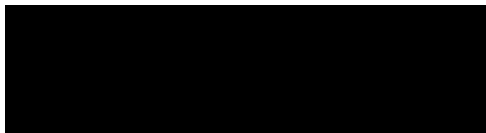
January 31, 2024

DECLARATION OF AUTHORSHIP

- This work has not previously been accepted in substance for any degree and is not being concurrently submitted in candidature for any degree.

- This thesis is the result of my own investigations, except where otherwise stated. Other sources are acknowledged by explicit references and a full bibliography is appended.

- I hereby give consent for my thesis, if accepted, to be available for electronic sharing, inter-library loan and/or for the thesis, title and summary to be made available outside organisations.

- The University's ethical procedures have been followed and, where appropriate, that ethical approval has been granted.

Signed: ███████████████ (candidate)

Date: January 31, 2024

"If you thought that science was certain - well, that is just an error on your part."

R. P. FEYNMAN

Abstract

This thesis is structured in three broad sections. The first presents a brief introduction to the field of quantum chromodynamics (QCD) and regularisation methods, which precedes a more thorough description of the lattice field theoretic approach to QCD and its non-relativistic formalism, NRQCD, which is used in the analysis contained within this document.

The second section introduces the first problem of interest, spectral reconstruction in the case of bottomonium mesons. We focus in particular on the Laplacian nature of the problem and present the Backus-Gilbert method as a means of producing regularised solutions. The resolving power of the method is discussed and the overall approach is then extended with the inclusion of a novel technique known as Laplace shifting, which takes advantage of the structure of the problem to provide a controlled resolution improvement to the method. A study of this technique is presented and applied to results obtained from Fastsum's anisotropic NRQCD ensembles from which connections with a known phenomenon in Monte-Carlo based physics called Parisi-Lepage statistical scaling are elucidated.

The third and final section focuses on probing the temperature dependence of the gluon propagator again calculated using the Fastsum Gen-2L ensembles. We begin by showing results for the propagator in the Coulomb gauge, before extending to the Landau gauge where we discuss the necessary modifications to support the lattice anisotropy.

CONTENTS

LIST OF FIGURES

LIST OF TABLES

Acronyms

BCD	–	Body-Centred Diagonal
BG	–	Backus-Gilbert
BR	–	Bayesian Reconstruction
FGR	–	First Gribov Region
FMR	–	First Modular Region
FWHM	–	Full-Width (at) Half-Maximum
HLT	–	Hansen-Lupo-Tantalo
KMS	–	Kubo-Martin-Schwinger
KRR	–	Kernel Ridge Regression
(MC)MC	–	(Markov Chain) Monte Carlo
MEM	–	Maximum Entropy Method
PDG	–	Particle Data Group
(NR)QCD	–	(Non-Relativistic) Quantum chromodynamics
QED	–	Quantum electrodynamics
QGP	–	Quark-Gluon Plasma
SVD	–	Singular Value Decomposition

Conventions

- Unless specified otherwise, $\hbar = c = 1$.

- All logarithms have their bases explicitly written except for $\ln(x)$ will be used to denote the natural log, $\log_e(x)$.

- Unless stated otherwise, Greek letters such as μ, ν, etc. run over the Euclidean indices 1-4, where we define $\mu = (x, y, z, t)$. Comparison with Minkowski equivalents will be explicitly denoted with an M (e.g. $\gamma_\mu^M = \gamma_0 \ldots \gamma_3$, where $\mu^M = (t, x, y, z)$).

- Momenta topped with a caret (e.g. $|\hat{p}|$ or $\hat{q}$) denote the lattice momenta (i.e. the Fourier transform of the lattice coordinate). To highlight the difference in discussions between Coulomb (Chapter 5) and Landau gauge (Chapter 6), we denote the momentum by $|p|$ and q respectively.

Acknowledgements

Chapter 1

Introduction

1.1 The Foundation of QCD

The emergence of quantum mechanics in the early 20th century spurred the rapid development of radical new theories in opposition to the long-established classical approaches to physics. Early developments such as the solution to the ultraviolet catastrophe by Max Planck and the description of the photoelectric effect by Albert Einstein paved the way for a fully-fledged development of a quantum-mechanical interpretation of physics starting in the 1920s.

Theoretical studies of the internal forces of the atomic nucleus led Hideki Yukawa to hypothesise in 1934 the existence of an intermediary 'carrier' particle which generates a force acting in opposition to the Coulombic repulsion between protons in the nucleus [18]. This particle was called the 'meson', derived from the Greek word *mesos* ("intermediate"). The first true[1] meson, the charged pion, was discovered in 1947 by a collaboration led by Cecil Powell [19]. Subsequent meson discoveries in the following decade uncovered shared properties between mesons, classified by their charge q, isospin I and strangeness s. This connection was codified by Yuval Ne'eman and Murray Gell-Mann into a scheme dubbed the *eightfold way* [20, 21], and is regarded as one of the earliest attempts to describe the underlying symmetries of QCD.

The emergence of the "subnuclear zoo" of particles in the mid 20th century made it increasingly improbable that they could each be elementary, and so it was clear that particle theory needed to be modified to support the existence of so many new types of particle. The discovery [22] of the Δ^{++} baryon required the introduction

---

[1]The first candidate for Yukawa's 'meson' was discovered in 1936 by Carl David Anderson, but was later found to be what is now known as the muon, the leptonic cousin of the electron.

of an additional, hidden degree of freedom to rectify the apparent noncompliance of the Δ^{++} with the Fermi exclusion principle. This degree of freedom was later identified as the SU(3) color charge, when quantum chromodynamics (QCD) was properly formalised [23, 24].

As with almost every other type of matter present in nature, the quest to map out the phase diagram of quark matter became of significant interest. Unlike the phase diagrams of chemistry which are usually in terms of the temperature and pressure of the system, the analogous quantities in our case are temperature and chemical potential. At low temperature and chemical potential (as is the current state of nature here on Earth) one anticipates quark matter to be bound, or *confined*, to a hadronic state. As the temperature and chemical potential increase (as was the case in the early Universe) the quark matter melts and enters a plasma-like state known as the quark-gluon plasma (QGP). However, arguably the most exotic behaviour (and the one which eludes researchers the most) exists at lower temperatures but very high chemical potentials, beyond that of the densest objects known in our universe: neutron stars. In such conditions, it is theorised [25] that quark matter enters a color-flavour-locked superconducting state, which we anticipate will exhibit a similar departure from the properties of 'conventional' quark matter to that seen when metals enter electrically-superconducting states. Further discussion of the phases of QCD is given in §1.3.

1.2 QCD in the Continuum

Before we can begin to discuss the various properties and phenomena exhibited by QCD, we must first define it in terms of a quantum field theory. QCD describes the dynamics of quarks and gluons, and the action which describes their interactions may be split into two parts:

$$S_{\text{QCD}} = S_F[\bar{\psi}, \psi, A_\mu] + S_G[A_\mu], \tag{1.2.1}$$

where $\bar{\psi}(x), \psi(x)$ are spinor fields describing the antiquarks and quarks respectively and A_μ are the gluon fields. S_F describes the fermionic component of the QCD action, whereas S_G encodes the gauge field dynamics. The fermionic action, coupled

with some strength g to the gauge field A_μ, is given by

$$
\begin{aligned}
S_F[\psi, \bar{\psi}, A_\mu] &= \sum_{i=1}^{N_f} \int d^4x \; \bar{\psi}^{(i)}(x) \left[\gamma_\mu(\partial_\mu + igA_\mu(x)) + m^{(i)} \right] \psi^{(i)}(x) \\
&= \sum_{i=1}^{N_f} \int d^4x \; \bar{\psi}^{(i)}(x) \left[\slashed{D} + m^{(i)} \right] \psi^{(i)}(x),
\end{aligned}
\tag{1.2.2}
$$

where (i) denotes the flavor of the fermion when we consider theories with the number of flavors $N_f > 1$. The γ_μ are the 4×4 Dirac matrices, that introduce mixing between the spinor components of the quark fields $\bar{\psi}$ and ψ. The covariant derivative is defined as $D_\mu = \partial_\mu + igA_\mu$. The gauge action is a function only of the gluon fields A_μ:

$$
S_G[A] = \frac{1}{2g^2} \int d^4x \; \text{Tr} \left[F_{\mu\nu} F^{\mu\nu} \right],
\tag{1.2.3}
$$

where we define the antisymmetric field strength tensor as

$$
\begin{aligned}
F_{\mu\nu}(x) &= -i[D_\mu(x), D_\nu(x)] \\
&= \partial_\mu A_\nu(x) - \partial_\nu A_\mu(x) + ig[A_\mu(x), A_\nu(x)]. \\
&= \sum_a T_a \left(\partial_\mu A_\nu^a(x) - \partial_\nu A_\mu^b(x) - gf_{bc}^a A_\mu^b(x) A_\nu^c(x) \right) \\
&= \sum_a T_a F_{\mu\nu}^a(x)
\end{aligned}
\tag{1.2.4}
$$

where we have used the definition of the adjoint representation of the gluon fields, given by

$$
A_\mu = \sum_{a}^{N_c^2-1} A_\mu^a T_a
\tag{1.2.5}
$$

where N_c is the number of color charges described by the theory and $T_a = \lambda_a/2$ with λ the Gell-Mann matrices. The quantities f_{bc}^a are the structure constants of the representation, defined by $[T_a, T_b] = if_{ab}^c T_c$.

At first glance, both the fermionic and gauge actions appear similar in form to their counterparts in quantum electrodynamics (QED). However, the presence of the commutator in Eq. (1.2.4) which is a result of the non-Abelianness of the theory provides the first hint of the richness of the interactions described by the gauge action. Unlike the case of QED where the action is invariant under Abelian U(1) transformations, the equivalent symmetry for the QCD action is given instead by

local, non-Abelian SU(3) rotations:

$$\psi(x) \longrightarrow \Omega(x)\psi(x), \tag{1.2.6}$$

$$\bar{\psi}(x) \longrightarrow \bar{\psi}(x)\Omega^\dagger(x), \tag{1.2.7}$$

$$A_\mu(x) \rightarrow \Omega(x)\left(A_\mu(x) - \frac{i}{g}\partial_\mu\right)\Omega^\dagger(x), \tag{1.2.8}$$

where $\Omega(x) \in$ SU(3). One can see that the gauge action Eq. (1.2.4) is invariant under the above gauge transformation provided that the covariant derivative $D_\mu(x) = \partial_\mu + igA_\mu$ transforms as

$$D_\mu(x) \longrightarrow \Omega(x)D_\mu(x)\Omega^\dagger(x). \tag{1.2.9}$$

Expectation values for any QCD operator, O, are calculated via the path integral

$$\langle O \rangle = \frac{1}{Z}\int \mathcal{D}\bar{\psi}\mathcal{D}\psi\mathcal{D}A \; O[\bar{\psi}, \psi, A]e^{iS_{QCD}}, \tag{1.2.10}$$

$$Z = \int \mathcal{D}\bar{\psi}\mathcal{D}\psi\mathcal{D}Ae^{iS_{QCD}}, \tag{1.2.11}$$

with

$$S_{QCD}[\bar{\psi}, \psi, A] = S_F[\bar{\psi}, \psi, A] + S_G[A]. \tag{1.2.12}$$

1.3 EXPLORING THE PHASE DIAGRAM OF QCD

Attention is paid to the temperature, T, at which our dynamics take place and the chemical potential, μ, which describes the net density of particles in our system. Figure 1.1 shows the simplified QCD phase diagram, with some interesting phases noted. The QCD phase diagram is still mostly unexplored, with large swathes of the phase space being inaccessible using current techniques. The introduction of a finite chemical potential causes a sign problem wherein the interpretation of the exponentiated Euclidean action $e^{-S[\bar{\psi}, \psi]}$ as a probability measure is compromised and Monte Carlo importance sampling (which is the crux of lattice methods and will be outlined in §1.4.1) cannot be used. The solution to the sign problem is itself highly sought after by physicists and mathematicians alike. Recent approaches aimed at circumventing the sign problem have been introduced, the most notable being Taylor expansions of the action in powers of μ [26] and stochastic quantization methods using Langevin dynamics [27]. Both approaches work to some limited degree, but are
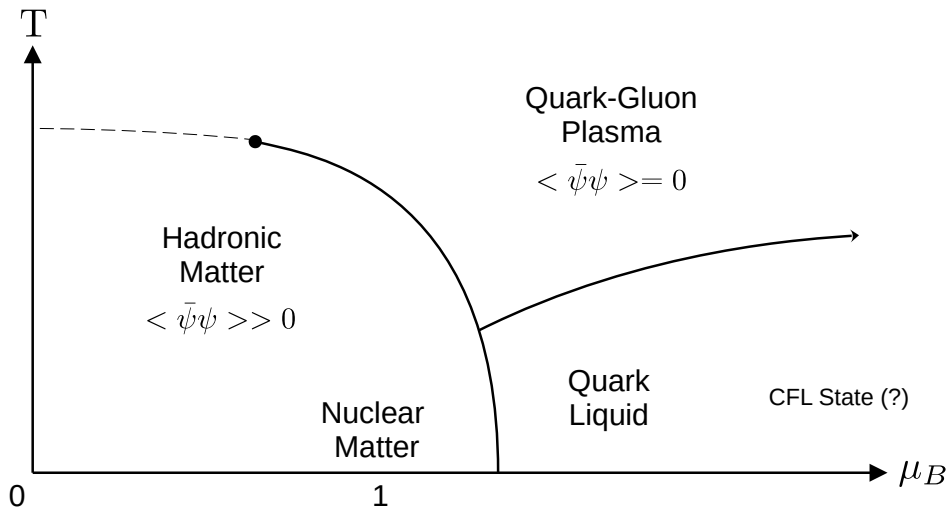
Figure 1.1: Simplified phase diagram for QCD in terms of the temperature T and baryonic chemical potential μ_B. Shown are the known and putative phases of quark matter. Adapted from [1].

still affected by constraints such as exponentially increasing compute requirements (the Taylor expansion) or inability to describe fermion dynamics (the Langevin method). In this work, we shall focus solely on the finite-temperature aspect at zero chemical potential.

1.4   LATTICE QCD

One of the difficulties which arises in the study of QCD is the handling of strong coupling constant, α_s, at the GeV scale. Unlike quantum-electrodynamics which may be expanded perturbatively in powers of $\alpha \simeq 1/137$, the strong coupling, α_s, grows with decreasing energy scale and is roughly unity at the scale of hadronic processes, meaning that we cannot probe this regime via perturbative methods. Several approaches have been formulated in an attempt to study QCD, with each possessing their respective strengths and weaknesses, but one of the most successful remedies to this problem comes in the form of lattice QCD.

Lattice field theory as a means of simulating QCD was first proposed by K.G. Wilson in 1974 [28]. In lattice QCD, the continuum QCD theory is discretised and embedded into a Euclidean lattice, Λ, using Wick rotated time $t \to i\tau$. The lattice is characterised by some spacing, a, and volume, $V = |\Lambda|$. The fermionic fields are located at each site $x \in \Lambda$ and are connected in each direction μ by a quantity

called a link variable $U_\mu(x)$, where $U_\mu = e^{iga_\mu A_\mu(x)}$. Fig. 1.2 shows the interpretation of the link variable, $U_\mu(x)$, as a quantity connecting two lattice sites x and $x + \hat{\mu}$ (Fig. 1.2-*Left*), with the convention for the reversed link shown in Fig. 1.2-*Right*. The link variables connecting the sites transform via

$$U_\mu(x) \rightarrow \Omega(x) U_\mu(x) \Omega^\dagger(x + \hat{\mu}). \tag{1.4.1}$$

Figure 1.2: *Left*: Diagram of the link field $U_\mu(x)$ connecting two lattice sites, x and $x + \mu$. *Right*: Backward link field $U_{-\mu}(x)$, the reverse of the link shown in *Left*.

The continuum fermion action of Eq. (1.2.2) can be cast onto the lattice by discretising the partial derivative

$$\partial_\mu \psi(x) \approx \frac{\psi(x + \hat{\mu}) - \psi(x - \hat{\mu})}{2a}, \tag{1.4.2}$$

such that the naive lattice fermion action becomes

$$S_F[\psi, \bar{\psi}, U] = a^4 \sum_{x \in \Lambda} \bar{\psi}(x) \left(\sum_\mu \gamma_\mu \frac{U_\mu(x)\psi(x + \hat{\mu}) - U_{-\mu}(x)\psi(x - \hat{\mu})}{2a} + m\psi(x) \right). \tag{1.4.3}$$

The naive lattice gauge action is given by

$$S_G[U] = \frac{2}{g^2} \sum_{x \in \Lambda} \sum_{\mu < \nu} \mathrm{ReTr}[\mathbb{1} - U_{\mu\nu}(x)], \tag{1.4.4}$$

where $U_{\mu\nu}(x)$ is a quantity known as the plaquette, given by a closed loop of link variables:

$$U_{\mu\nu} = U_\mu(x) U_\nu(x + \hat{\mu}) U_\mu^\dagger(x + \hat{\nu}) U_\nu^\dagger(x). \tag{1.4.5}$$

Fig. 1.3 shows the plaquette as constructed from the gauge like variables. It can be shown that $U_{\mu\nu} = \exp[ia^2 F_{\mu\nu} + \mathcal{O}(a^3)]$ and thus a small-a expansion Eq. (1.4.4) yields the continuum gauge action of Eq. (1.2.4).

The term 'naive' is often used to describe the fermion and gauge actions of Eq. (1.4.3) and Eq. (1.4.4) as they are shown without applying any of the improvement techniques which are common practice in lattice studies. These techniques include (but are not limited to) the Symanzik improvement scheme [29], which
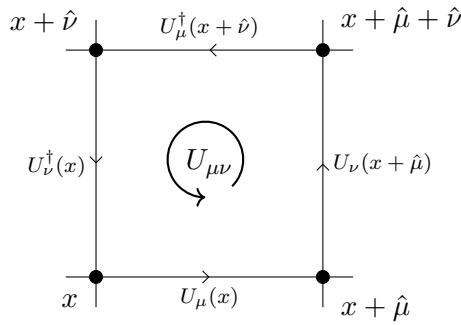
Figure 1.3: Diagram showing the plaquette, $U_{\mu\nu}(x)$.

leverages higher-order terms in the discretized form of the derivative to remove corrections up to some order in a, and clover-term improvement [30], which uses factors of the field strength tensor to deliver $\mathcal{O}(a)$ improvement on the Wilson action.

The link fields, $U_\mu(x)$, are arguably the most fundamental component of the lattice prescription. One can see that, by the transformation property of the link fields given in Eq. (1.4.1), the trace of the plaquette is gauge invariant. This property holds for any closed loop of link variables, regardless of size or construction. Two commonly studied objects similar in form to the plaquette are the Wilson and Polyakov loops. In the continuum, the Wilson loop is created by the parallel transport of the A_μ fields along a closed contour $\mathcal{C}$,

$$\mathcal{W}[\mathcal{C}] = \mathrm{Tr}\left[\mathcal{P}\exp\left(i\oint_{\mathcal{C}} A_\mu dx^\mu\right)\right]. \tag{1.4.6}$$

Consider the example where the Wilson loop is represented by a simple rectangular contour, $\mathcal{C} = R \times T$, with R and T the spatial and temporal segments respectively. On the lattice, this corresponds to a simple product of link variables along the path represented by $\mathcal{C}$:

$$\mathcal{W}(R,T) = \mathrm{Tr}\left[\prod_{\{x,\mu\}\in\mathcal{C}} U_\mu(x)\right]. \tag{1.4.7}$$

The static quark potential can be related to the expectation value of the Wilson loop via

$$\langle\mathcal{W}(R,T)\rangle \stackrel{T\to\infty}{\propto} e^{-V(R)T} \tag{1.4.8}$$

$$\propto \quad e^{-\sigma RT + \mu(R+T)} \tag{1.4.9}$$

where the second line is the result of a strong coupling expansion [31], with σ

the string tension and μ the perimeter coefficient. The expectation value of the Wilson loop can act as an order parameter for confinement. In the confined phase, the quantity $-\log \langle \mathcal{W}(R,T) \rangle$ scales proportionally with the area of the loop, RT, whereas in the deconfined phase it scales proportionally with the perimeter, $R+T$.

We may also modify the Wilson loop such the extent of the temporal contour equals the temporal extent of the lattice. In this case, the spatial segments are positioned atop one another, oriented in opposite directions. This results in a reduction of the Wilson loop into two disconnected paths oriented in opposite ways along the temporal direction. This path which winds the temporal direction is known as the Polyakov loop (also known in the literature as the thermal Wilson line) and is defined by

$$P(x) = \text{Tr}\left[\prod_{\tau=0}^{N_\tau - 1} U_4(\tau, x) \right]. \tag{1.4.10}$$

This quantity may then be related to the static quark potential, $V(R)$, by taking the product of the disconnected paths and using the relation given in Eq. (1.4.8):

$$\langle P(x)P^\dagger(y) \rangle \propto e^{-a_\tau N_\tau V(R)}, \tag{1.4.11}$$

where we have used $T = a_\tau N_\tau$, with a_τ the temporal lattice spacing, and $R = |\boldsymbol{x} - \boldsymbol{y}|$ [32].

The expectation value of a single Polyakov loop, $\langle P(x) \rangle$, may also serve as an order parameter for center symmetry breaking. Consider the center transformation

$$U_4(\tau, x) \rightarrow z U_4(\tau, x) \tag{1.4.12}$$

for all x corresponding to some timeslice τ, where $z \in \{\exp(2n\pi i/N_c)\,\mathbb{1}$ for $n \in [0, \ldots N_c)\}$ is an element of the cyclic group $\mathbb{Z}(N_c)$. The plaquette is trivially invariant under the transformation given in Eq. (1.4.12), but the Polyakov loop instead transforms as $P \rightarrow zP$. Since z is a member of the cyclic group, $\langle zP \rangle$ will vanish in the phase where the centre symmetry holds, but will acquire a finite value when the center symmetry is broken. The connection between center symmetry and deconfinement becomes manifest when one notes that the Polyakov loop expectation value obeys

$$|\langle P \rangle| \propto e^{-N_\tau F_q}, \tag{1.4.13}$$

with F_q the free energy of a color charge [31]. It is now evident that the link fields themselves encode a tremendous amount of information about the state of the lattice. Although the path integral has now been discretized into a finite series of integrals by the introduction of the link field formulation, the number of degrees of freedom are still large and the Euclidean probability function e^{-S} is sharply peaked about the classical minimum of the action, S, meaning that traditional integration methods would waste a lot of computation time calculating in regions where e^{-S} is small. This issue is side-stepped by using Monte Carlo integration with importance sampling.

1.4.1 Monte Carlo Integration

In order to measure the expectation value of some observable as in Eq. (1.2.10), one must perform an integral over an infinitely large space of group elements, U, and thus it is impossible to evaluate such an integral via analytic means. One can attempt to instead evaluate Eq. (1.2.10) numerically by taking the approximation

$$\langle \mathcal{O} \rangle \simeq \frac{1}{N} \frac{1}{Z} \sum_i^N \mathcal{O}[U_i] e^{-S[U_i]}, \tag{1.4.14}$$

where the fields U_i are uniformly sampled from the set of all configurations $\{U\}$. Although this would indeed produce the desired value of the path integral as $N \to \infty$, in practise (for high-dimensional systems) the action contribution $e^{-S[U]}$ is almost negligible for a large portion of the group space, thus making Eq. 1.4.14 an inefficient way of evaluating an integral over $\mathcal{D}U$. This may be remedied by instead generating our U_i via importance sampling, wherein U_i are chosen with probability

$$p[U_i] = \frac{e^{-S[U_i]}}{Z} \tag{1.4.15}$$

and thus the expectation value may be simply evaluated across the set of chosen samples:

$$\langle \mathcal{O} \rangle \simeq \frac{1}{N} \sum_i^N \mathcal{O}[U_i]. \tag{1.4.16}$$

A popular method for generating importance-sampled configurations is Markov chain Monte Carlo (MCMC). This involves starting with a random choice for U_i and then generating a new set of configurations U_{i+1} with a transition probability

P satisfying the so-called detailed balance condition

$$P[U_i \rightarrow U_j]p[U_j] = P[U_j \rightarrow U_i]p[U_i] \qquad (1.4.17)$$

where $U_i, U_j \in \{U\}$. This ensures that the target distribution $p[U]$ is obtainable from any arbitrary starting distribution $p_0[U]$ given a sufficiently long chain of configurations.

There exist additional subtleties which also must be considered with the Markov chain approach. These include unphysical effects such as autocorrelation (as subsequent elements of the chain are naturally correlated as a result of the generation process) and equilibration/thermalisation issues (if the choice of p_0 is so far from the target distribution that the generated U_i do not correctly sample the target distribution). These intricacies have been studied in the context of Monte Carlo integration with detailed discussion in the literature [31, 32] and therefore will not be discussed further in this work.

1.5 Finite Temperature on the Lattice

As visible in Eq. (1.4.13), there is a deep connection between the temporal extent of the lattice and temperature. In order to elucidate this connection, we turn to the discussion relating Euclidean quantum field theory and the partition function of a classical statistical mechanical system, which is usually one of the first topics discussed in any meritorious book on lattice quantum field theory.

The partition function of a quantum-mechanical system is given by

$$\mathcal{Z}(T) = \text{Tr} \left[e^{-\beta \hat{H}} \right], \qquad (1.5.1)$$

where $\hat{H}$ is the Hamiltonian operator corresponding to the system and $\beta = 1/k_B T$ the inverse temperature, with k_B the Boltzmann constant (which will be set to $k_B = 1$ in the following). One may re-express the partition function as a path integral by recalling the form of the evolution operator in Euclidean time,

$$U_E(x_1, \tau_1; x_2, \tau_2) = \langle x_1 | e^{-H(\tau_2 - \tau_1)} | x_2 \rangle = \int \mathcal{D}x \exp \left[\int_{\tau_1}^{\tau_2} \mathcal{L}_E(x, \tau) d\tau \right]. \qquad (1.5.2)$$

The trace in Eq. (1.5.1) restricts the partition function to fields which are periodic (bosonic) or anti-periodic (fermionic) in time, and so one can express the partition

function as an integral over these fields:

$$\mathcal{Z}(T) = \int \mathcal{D}\Phi e^{-S_E[\Phi]}, \qquad (1.5.3)$$

with $S_E[\Phi]$ the Euclidean action for the fields Φ,

$$S_E[\Phi] = \int_0^\beta d\tau \int_{\mathbb{R}^3} dx^3 \mathcal{L}_E(\Phi(\tau, x), \partial_\mu \Phi(\tau, x)). \qquad (1.5.4)$$

The compactification of the time dimension in Eq. (1.5.4) arises when one compares Eq. (1.5.2) with Eq. (1.5.1) and notes that $\beta = 1/T = N_\tau$, with N_τ the extent of the time window, $\tau_2 - \tau_1$ [31, 32].

This equivalence between the temporal extent and the temperature still holds when the theory is cast onto the lattice. Thus, by simulating our theory on lattices of different temporal sizes but fixed spatial volume, one may probe the dynamics of the theory at different temperatures.

1.6 Non-Relativistic QCD

There are three main energy scales which must be considered when studying the dynamics of a particle: the mass, M, the momentum, Mv, and the kinetic energy, $\frac{1}{2}Mv^2$. At relativistic speeds, $v \sim 1$, these scales are approximately equivalent, but when the dynamics of the system become non-relativistic we find $v \ll 1$ and the energy scales become widely separated. If one is to model the dynamics of such a system, larger lattice sizes must be used to sufficiently probe the infrared regime. This issue may be treated in part by using a renormalisation strategy such as that of non-relativistic QCD (NRQCD) [33, 34], which decouples the non-relativistic dynamics from the usual relativistic theory by integrating out contributions from momenta larger than $\mathcal{O}(M_b)$, where M_b is the bottom quark mass, simplifying the simulation of heavy mesons.

The NRQCD formulation is implemented by introducing an ultraviolet cutoff, $M_b v \ll \Lambda_{\mathrm{NRQCD}} \ll M_b$, to the QCD Lagrangian which separates short-distance effects on the scale of M or larger from those which arise from the small momentum scales of Mv, Mv^2 and the scale at which non-perturbative effects take hold, $\Lambda_{\mathrm{QCD}} \sim Mv^2$ [35]. The resulting Lagrangian is then split into two parts: the leading term given by the Lagrangian of a Schrödinger field and correction terms which for now

will be absorbed into the perturbation $\delta\mathscr{L}_0$. The NRQCD Lagrangian is then given by

$$\mathscr{L}_{\text{NRQCD}} = \psi^\dagger \left\{ iD_t + \frac{\boldsymbol{D}^2}{2M} \right\} \psi + \delta\mathscr{L}_0 \tag{1.6.1}$$

where $\mathscr{L}_{\text{light}}$ contains the dynamics of the light quarks and gluons, $\delta\mathscr{L}_0 = \delta\mathscr{L}_K + \delta\mathscr{L}_E + \delta\mathscr{L}_B + \delta\mathscr{L}_{EE}$ correspond to the kinetic (relativistic), electrostatic and magnetostatic scattering and spin-splitting corrections, respectively, and D_τ, $\boldsymbol{D}$ are the gauge-covariant temporal and spatial derivatives. The corrections are local and their magnitude curtailed by an $\mathcal{O}(v^4)$ cut-off, chosen to ensure good agreement with the relativistic theory, which yields an estimated systematic error of 10% or less [36]. There is, notably, no mass-like term, $M_b\psi^\dagger\psi$, as the non-relativistic framework only serves to calculate the energy difference from some zero-point [34] and the rest mass can be removed from the NRQCD dispersion relation via a redefinition of the quark fields [37]. The NRQCD formulation is well suited to the lattice discretisation procedure and has a long history of use in research focusing on the study of bottom quarks and bottomonia [36, 38].

To leading order, the NRQCD lattice action can be expressed in terms of a hopping expansion,

$$S_0^{(k)}(x) = a^3 \sum_{x \in \{\Lambda\}} \left[\psi^\dagger(x)\psi(x) \right.$$
$$\left. - \psi^\dagger(x + a_\tau\hat{\tau}) \left(1 - \frac{a_\tau H_0}{2k}\right)^k U_\tau(x)^\dagger \left(1 - \frac{a_\tau H_0}{2k}\right)^k \psi(x) \right] \tag{1.6.2}$$

where k is a positive integer known as the Lepage parameter, introduced to control the stability of the expansion, required by the condition, $\max|1 - a_\tau H_0/2k| < 1$ [34]. For the inverse coupling used in our work, $\beta \approx 1.5$, $k = 1$ is sufficient to simulate the b quark [37]. H_0 is the leading order term of the Hamiltonian, i.e., the discrete form of the kinetic energy operator

$$H_0 \equiv -\frac{\boldsymbol{\Delta}^{(2n)}}{2M_b}, \quad \text{with} \quad \boldsymbol{\Delta}^{(2n)} = \sum_i^3 (\nabla_i^+\nabla_i^-)^n, \tag{1.6.3}$$

with $2n$ the order of the derivative and ∇^+ and ∇^- the usual forward and backward covariant finite differences, respectively. The corresponding, discrete form of the leading-order Green's function for the quark fields is then given by the evolution

equation

$$G_0(x, \tau + a_\tau \hat{\tau}) = \left(1 - \frac{a_\tau H_0}{2k}\right)^k U_\tau^\dagger(x) \left(1 - \frac{a_\tau H_0}{2k}\right)^k G_0(x, \tau) + \delta_{x,0} \delta_{\tau + a_\tau, 0}. \quad (1.6.4)$$

The $\delta_{\tau + a_\tau, 0}$ term ensures that $G_0(x, \tau) = 0$ for $\tau < 0$ and one sets $G_0(x, \tau = 0) = S(x)$ with $S(x)$ the quark field source. This means that the NRQCD propagator solves an initial-value problem, which is less computationally expensive to simulate than a fully-relativistic propagator.

In order to account for the correction terms associated with $\delta \mathscr{L}_0$ in Eq. (1.6.1), the evolution equation $G_0(x, \tau + a_\tau \hat{\tau})$ must be modified using the Hamiltonian correction, δH, such that

$$G(x, \tau + a_\tau \hat{\tau}) = G_0(x, \tau + a_\tau \hat{\tau})(1 - a_\tau \delta H), \quad (1.6.5)$$

where

$$\begin{aligned}
\delta H = &- \frac{(\Delta^{(2)})^2}{8M_b^3} + \frac{ig_0}{8M_b^2}(\nabla^\pm \cdot E - E \cdot \nabla) \\
&- \frac{g_0}{8M_b^2} \sigma \cdot (\nabla^\pm \times E - E \times \nabla) - \frac{g_0}{2M_b} \sigma \cdot B \\
&+ \frac{a_s^2 \Delta^{(4)}}{24M_b} - \frac{a_s (\Delta^{(2)})^2}{16k M_b^2},
\end{aligned} \quad (1.6.6)$$

with g_0 the bare coupling, and a_s, a_τ are the spatial and temporal lattice spacings, respectively [37].

Finally, the mass of the bottom quark, $a_s M_b$, in our simulation is determined by tuning the spin-averaged kinetic mass of the s-wave bottomonium mesons (the η_b and Υ), $M(\overline{1S}) = (M(\eta_b) + 3M(\Upsilon))/4$, such that it equals its experimental value of $M(\overline{1S}) = 9444.7(8)$MeV [2]. In our work, this is achieved by fitting the lattice dispersion relation

$$a_\tau E(|p|^2) = a_\tau E(|p| = 0) + \frac{a_s^2 |p|^2}{2\xi^2 a_\tau M_2} + \mathcal{O}(a^2), \quad (1.6.7)$$

where $\xi = a_s/a_\tau$ is the lattice anisotropy (see §3.1 for details) and $|p|$ corresponds to the lattice momentum

$$a_s^2 |p|^2 = 4 \sum_i^3 \sin^2\left(\frac{n_i \pi}{N_s}\right), \quad (1.6.8)$$

with $n_i \in [-N_s/2, \ldots, N_s/2)$.

One drawback of the NRQCD formulation is that the continuum limit is not well defined due to the presence of UV divergent terms which contribute factors of $(a_s M_b)^{-1}$ and thus we are limited to the regime where $a_s \sim 1/M_b$ [33].

Reconstructing the Bottomonium Spectrum in NRQCD using the Backus-Gilbert Method

In this chapter we begin by motivating studies of the bottomonium spectrum before relating the spectral density function to the Euclidean correlator using the Källén-Lehman representation. We present a brief overview of reconstruction techniques before introducing the Backus-Gilbert method. We then discuss improvements upon the Backus-Gilbert method in §2.8 by exploiting the Laplacian nature of the NRQCD kernel.

2.1 Bottomonia

The existence of a new 'quarkyonic' state of matter has been theorised ever since the junior years of QCD [39]. The discovery in the early 1970s that quarks become asymptotically free [40, 41] at sufficiently high energies prompted discussion into the nature of this boundary between hadronized matter and the theorised plasma-like state of unconfined quarks and gluons. Studies [42] of the J/Ψ ($c\bar{c}$) system predicted melting of the state above the Hagedorn temperature and thus serves as a signal for the onset of the so-called quark-gluon plasma (QGP), which was eventually discovered at CERN in 2000 [43]. It is therefore expected that a similar study using the heavier $b\bar{b}$ bottomonium system should also exhibit similar behaviour. Thus, by measuring quantities such as the mass and width of the ground state at finite temperature, we expect to be able to probe the deconfinement transition.

Lattice QCD is a well-established approach which is able to explain the behaviour of mesons such as the J/Ψ and the heavier bottomonium system. In the rest of the

chapter we outline how non-relativistic measurements of the correlation function for a particular meson channel can be used to extract information such as the ground state mass and width.

2.2 The Spectral Representation of the Two-Point Correlator

For any given particle, the in-medium properties of bound states are described by its spectral density function $\rho(\omega)$. Properties of particular interest include the mass and width of the ground and excited states of the particle, along with associated quantities such as transport behaviour, diffusion coefficients and thermal conductivity of the system.

Consider some operator, $\mathcal{O}$, in Wick-rotated time, τ, which produces some particle state of which we wish to determine the spectrum. The correlator is given by the two-point function

$$
\begin{aligned}
G(\tau, \boldsymbol{x}) &= \langle \mathcal{O}(\tau, \boldsymbol{x}) \mathcal{O}(0, \boldsymbol{0}) \rangle \\
&= D^+(\tau, \boldsymbol{x}),
\end{aligned}
\tag{2.2.1}
$$

where $D^+(\tau, \boldsymbol{x})$ is known as the forward-ordered propagator. It can be expressed as a function of the momentum, $\boldsymbol{p}$, via the Fourier transform:

$$
G(\tau, \boldsymbol{p}) = \int_{-\infty}^{\infty} d^3\boldsymbol{x}\ e^{-i\boldsymbol{p}\cdot\boldsymbol{x}} D^+(\tau, \boldsymbol{x}).
\tag{2.2.2}
$$

We may rewrite $G(\tau, \boldsymbol{p})$ in terms of the energy-momentum space forward ordered propagator $D^+(\omega, \boldsymbol{p})$ by inserting its definition,

$$
D^+(\tau, \boldsymbol{x}) = \int_{-\infty}^{\infty} \frac{d\omega}{2\pi} \int_{-\infty}^{\infty} d^3\boldsymbol{p}' e^{i\boldsymbol{p}'\cdot\boldsymbol{x}} e^{-\omega\tau} D^+(\omega, \boldsymbol{p}'),
\tag{2.2.3}
$$

into Eq. (2.2.2), yielding

$$
G(\tau, \boldsymbol{p}) = \int_{-\infty}^{\infty} \frac{d\omega}{2\pi} \iint_{-\infty}^{\infty} d^3\boldsymbol{x} d^3\boldsymbol{p}' e^{-i(\boldsymbol{p}-\boldsymbol{p}')\cdot\boldsymbol{x}} e^{-\omega\tau} D^+(\omega, \boldsymbol{p}')
\tag{2.2.4}
$$

$$
= \int_{-\infty}^{\infty} d\omega \int_{-\infty}^{\infty} \frac{d^3\boldsymbol{p}'}{2\pi} \delta^3(\boldsymbol{p}'-\boldsymbol{p}) e^{-\omega\tau} D^+(\omega, \boldsymbol{p}')
\tag{2.2.5}
$$

$$
= \int_{-\infty}^{\infty} \frac{d\omega}{2\pi} e^{-\omega\tau} D^+(\omega, \boldsymbol{p}).
\tag{2.2.6}
$$

Dividing the integral over ω then gives

$$
\begin{aligned}
G(\tau, \boldsymbol{p}) &= \int_{-\infty}^{\infty} \frac{d\omega}{2\pi} e^{-\omega\tau} D^+(\omega, \boldsymbol{p}) + \int_{-\infty}^{0} \frac{d\omega}{2\pi} e^{-\omega\tau} D^+(\omega, \boldsymbol{p}) \\
&= \int_{0}^{\infty} \frac{d\omega}{2\pi} e^{-\omega\tau} D^+(\omega, \boldsymbol{p}) + \int_{0}^{\infty} \frac{d\omega}{2\pi} e^{\omega\tau} e^{\beta\omega} D^-(\omega, \boldsymbol{p}),
\end{aligned}
\tag{2.2.7}
$$

where we have used the Kubo-Martin-Schwinger relations for forward and backward-ordered propagators:

$$
D^+(\tau, \boldsymbol{x}) = D^-(\tau + i\beta, \boldsymbol{x}), \tag{2.2.8}
$$

$$
D^+(\omega, \boldsymbol{p}) = e^{\beta\omega} D^-(\omega, \boldsymbol{p}). \tag{2.2.9}
$$

The spectral density function is defined as the difference of the forward and backward propagators:

$$
\rho(\omega) = \frac{D^+(\omega, \boldsymbol{p}) - D^-(\omega, \boldsymbol{p})}{2\pi}. \tag{2.2.10}
$$

Combining Eq. (2.2.10) with the KMS relations in Eq. (2.2.9) yields:

$$
D^+(\omega, \boldsymbol{p}) = 2\pi\rho(\omega, \boldsymbol{p}) n(\omega; \beta), \tag{2.2.11}
$$

$$
D^-(\omega, \boldsymbol{p}) = 2\pi\rho(\omega, \boldsymbol{p})(1 + n(\omega; \beta)), \tag{2.2.12}
$$

where $n(\omega; \beta) = 1/(e^{\beta\omega} - 1)$ and β is the inverse temperature defined in §1.5. Substituting the above into Eq. (2.2.7) yields

$$
\begin{aligned}
G(\tau, \boldsymbol{p}) &= \int_{0}^{\infty} d\omega \ \rho(\omega) \left[n(\omega; \beta) e^{-\omega\tau} + e^{\omega\tau}(1 + n(\omega; \beta)) \right] \\
&= \int_{0}^{\infty} d\omega \ \rho(\omega) \frac{\cosh[\omega(\tau - \beta/2)]}{\sinh(\omega\beta/2)}.
\end{aligned}
\tag{2.2.13}
$$

Since we are interested in the properties of the spectrum at finite temperature, we integrate over the momentum, $\boldsymbol{p}$, and express the correlation function in the form

$$
G(\tau; T) = \int_{0}^{\infty} d\omega K(\tau, \omega; T) \rho(\omega; T), \tag{2.2.14}
$$

where $K(\tau, \omega; T)$ is called the kernel function and $G(\tau; T)$ and $\rho(\omega; T)$ are the finite-temperature correlation and spectral density functions. In the non-relativistic limit, which we shall make use of in this work, the kernel function of Eq. (2.2.13) reduces to a simple exponential. This can be seen by making the kernel substitution $\omega = \omega' + M$

with M the particle mass, such that

$$K(\tau, \omega; T) = \frac{\cosh[(\omega' + M)(\tau - \beta/2)]}{\sinh[(\omega' + M)\beta/2]}. \qquad (2.2.15)$$

In the regime where $M \gg T$, one finds that $e^{-M\beta} \approx 0$ and the kernel function reduces to

$$K(\tau, \omega; T) \approx \frac{e^{-(\omega' + M)(\tau - \beta/2)}}{e^{(\omega' + M)\beta/2)}}, \qquad (2.2.16)$$

$$= e^{-(\omega' + M)\tau}. \qquad (2.2.17)$$

Shifting the integration variable of Eq. (2.2.13) to subtract out the particle mass, M, yields the non-relativistic spectral representation

$$G_{\mathrm{NR}}(\tau; T) = \int_{-M}^{\infty} d\omega' \rho(\omega'; T) e^{-\omega' \tau}. \qquad (2.2.18)$$

For the sake of clarity, we shall drop the prime notation and use ω to denote the non-relativistic energy. The resulting non-relativistic kernel $K(\tau, \omega) = e^{-\omega\tau}$ is temperature independent and notably lacks periodicity in τ, meaning that the full temporal extent is accessible for spectral reconstruction (i.e. there are no backward-moving modes which contaminate the signal at large τ).

One of the difficulties in inverting Eq. (2.2.18) is that $G(\tau; T)$ generally is of $\mathcal{O}(10 - 100)$ observations whereas $\rho(\omega; T)$ is continuous ($\mathcal{O}(1000+)$), meaning that for a given set of observations $G(\tau; T)$ measured to within some error, we cannot expect to uniquely reconstruct the underlying spectrum. It has been previously argued that $\rho(\omega)$ cannot be constrained even when $G(\tau)$ is known *exactly* [44].

Consider the addition of a small oscillatory function $\delta\rho$ to the spectrum:

$$\delta\rho_s(\omega) = \sin(s\omega). \qquad (2.2.19)$$

By Eq. (2.2.14), the resulting perturbation in $G(\tau)$ is of the form

$$\delta G_s(\tau) = \int_a^b K(\tau, \omega) \delta\rho_s(\omega) d\omega$$
$$= \int_a^b K(\tau, \omega) \sin(s\omega) d\omega \xrightarrow[s \to \infty]{} 0, \qquad (2.2.20)$$

which is true for any integrable kernel function $K(\tau, \omega)$. Thus, we can make δG_s

arbitrarily small provided s is sufficiently large, and in such a case any numerical determination of $\rho(\omega)$ cannot be exact.

It is for this reason that the spectral reconstruction problem is regarded as ill-posed as we cannot, in general, entirely constrain the form of $\rho(\omega)$.

2.3 Restrictions on the Invertibility of the Laplace transform

The issue outlined in Eq. (2.2.20) is better understood from an information theory perspective [44]. Problems similar in form to Eq. (2.2.14), known in the literature as Fredholm equations, have long been studied in an attempt to characterise the way in which information is transmitted from $\rho(\omega)$ to the observations $G(\tau)$ [45]. Consider a function of the form

$$G(\tau) = \int_0^\infty K(\tau,\omega)\rho(\omega)d\omega. \tag{2.3.1}$$

If $\rho(\omega)$ and $G(\tau)$ are both positive semi-definite, then the convolution with $K(\tau,\omega)$ represents a linear transformation in the information space corresponding to Eq. (2.3.1). That is, one may think of $K(\tau,\omega)$ as the function which maps the information in energy space contained in $\rho(\omega)$ onto our correlator, $G(\tau)$, which is a function of the temporal coordinate, τ. Consider the eigenvalue problem

$$\int_0^\infty \phi_s(\omega)K(\tau,\omega)d\omega = \lambda_s\phi_s(\tau) \tag{2.3.2}$$

where ϕ_s is the eigenfunction corresponding to the eigenvalue λ_s. One may think of ϕ_s as a small packet of information which is transformed from ω-space to τ-space by our convolution, with λ_s representing the 'strength' of the information transmission. It is straightforward to show (see Appendix A.1 for detail) that for the Laplacian kernel $e^{-\omega\tau}$ the eigenvalues λ_s are given by

$$\lambda_s^\pm = \pm\sqrt{\Gamma(s)\Gamma(1-s)} \tag{2.3.3}$$

where Γ is the Gamma function:

$$\Gamma(s) = \int_0^\infty x^{s-1}e^{-x}dx, \qquad (\mathrm{Re}(s) > 0). \tag{2.3.4}$$

If we take s to lie along the functional strip $s = \frac{1}{2} + i\nu$ with ν continuous and unbounded, the eigenvalues may be re-expressed in the form

$$|\lambda_\nu^\pm|^2 = \left|\Gamma\left(\frac{1}{2} + i\nu\right)\right|^2 \equiv \frac{\pi}{\cosh(\pi\nu)}. \tag{2.3.5}$$

One can now see that as $\nu \to \infty$, the eigenvalues λ_ν become arbitrarily small, meaning the transmissive power decreases and the problem becomes ill-posed. The authors of Ref. [46] have investigated the Laplace transform further in this context and conclude that the reconstructibility of a particular Laplace transform may be evaluated via a study of its eigenvalue decomposition, with artificial neural networks having general success at reconstructing problems with large eigenvalue components but require additional regularization when the eigenvalues are small.

2.4 Techniques for Spectral Reconstruction

The construction of rigorous, method-independent estimates for the spectral density function has thus far eluded physicists, with a number of techniques having been applied to the reconstruction problem and each with varying degrees of success.

Some well-established approaches use Bayesian inference to extract the form of $\rho(\omega)$. One such example is the Maximum Entropy Method [47] which uses an entropy-based prior constructed from known constraints on the spectrum (such as positivity) and has been applied with success to the study of the bottomonium spectrum [37]. Another more recently proposed approach is Bayesian Reconstruction (BR) [48] which uses a set of alternative axioms which shape the form of the prior. Other approaches include Maximum Likelihood methods using multi-exponential fitting [49] and also Kernel Ridge Regression (KRR) [50]. Thus far, each of the aforementioned methods provide differing predictions for the bottomonium spectrum at finite temperature.

In recent years, a well-established method [51–56] from the field of geophysics and seismology called Backus-Gilbert [57] has received renewed interest in the physics community as a potential spectral reconstruction technique [58–61]. The method, named for its originators G.E. Backus and J.F. Gilbert, was originally devised to estimate the maximum resolving power which could be provided by a set of seismological observations, which in turn allows for the reconstruction of "gross Earth models" which represent the internal structure of the Earth. We will outline in the

following section how the method can be adapted to a problem similar in form to
Eq. (2.2.14).

2.5 THE BACKUS-GILBERT METHOD

The Backus-Gilbert method [57] is a regularisation technique which constructs esti-
mates for the solutions to a category of ill-posed inverse problems which satisfy the
Fredholm integral of the first kind:

$$g(\tau) = \int_a^b K(\tau, \omega) f(\omega) d\omega, \tag{2.5.1}$$

where $g(\tau)$ and $K(\tau, \omega)$ are known and $f(\omega)$ is some unknown function to be re-
constructed. The solution to Eq. (2.5.1) requires the construction of the continuous
function, $f(\omega)$, from a finite number of discrete observations, $g(\tau)$. At each ob-
servation point, τ, the target function, $f(\omega)$, is convolved with $K(\tau, \omega)$ to produce
the observation. The objective of the Backus-Gilbert method is to construct an
estimate of the target function at some point $\omega_0 \in \{\omega\}$ (with $\{\omega\}$ representing the
window in which $f(\omega)$ is to be reconstructed) using only a linear combination of the
observation data $g(\tau)$:

$$\hat{f}(\omega_0) = \sum_\tau c_\tau(\omega_0) g(\tau), \tag{2.5.2}$$

where $\hat{f}(\omega_0)$ denotes our reconstructed estimate of $f(\omega_0)$ and $c_\tau(\omega_0)$ are a set of
coefficients which are to be determined by the method. Inserting Eq. (2.5.1) into
Eq. (2.5.2) gives

$$\hat{f}(\omega_0) = \sum_\tau \int_a^b c_\tau(\omega_0) K(\tau, \omega) f(\omega) d\omega \tag{2.5.3}$$

$$= \int_a^b A(\omega, \omega_0) f(\omega) d\omega, \tag{2.5.4}$$

where we have defined the *averaging function*:

$$A(\omega, \omega_0) = \sum_\tau c_\tau(\omega_0) K(\tau, \omega). \tag{2.5.5}$$

Ideally, one would like to find the values of $c_\tau(\omega_0)$ such that $A(\omega, \omega_0)$ resembles the
delta-function as closely as possible, such that $\hat{f} \to f$. The method therefore makes

the fundamental assumption that

$$\lim_{\tau \to \infty} A(\omega, \omega_0) = \delta(\omega - \omega_0). \tag{2.5.6}$$

In practise this is not possible due to the finite number of observations which can
be obtained from the lattice. This causes $A(\omega, \omega_0)$ to acquire a finite width which
may be minimised via a choice of several criteria, two such examples of which are
the spread criterion, $W(s_0)$, proposed in Backus and Gilbert's seminal paper [57],

$$W(\omega_0) = \int_a^b 12(\omega - \omega_0)^2 A(\omega, \omega_0)^2 d\omega, \tag{2.5.7}$$

and the least-squares (also known in the literature as 'Dirichlet') criterion, $J(\omega_0)$
[52],

$$J(\omega_0) = \int_a^b \left[A(\omega, \omega_0) - \delta(\omega - \omega_0) \right]^2 d\omega. \tag{2.5.8}$$

The spread criterion, $W(\omega_0)$, corresponds to the minimisation of the second moment
of the averaging function. The factor of 12 facilitates the geometric interpretation
of $W(\omega_0)$ as a box-car estimate of the width of $A(\omega, \omega_0)$ about ω_0 [62]. The factor
of $(\omega - \omega_0)^2$ in Eq. (2.5.7) is a localisation factor which penalises contributions at
large $|\omega - \omega_0|$. In theory, one may choose any such localisation factor which obeys
this property, for example $|1 - \mathcal{N}(\omega_0, \sigma)|$ with $\mathcal{N}$ the normal distribution.

Minimising Eq. (2.5.7) with respect to the coefficients $c_\tau(\omega_0)$ (see discussion in
Appendix A.2) yields the trivial solution $c_\tau = 0, \quad \forall \tau$, which may be avoided by en-
forcing unimodularity of the averaging function, $\int A(\omega, \omega_0) d\omega = 1$. This is achieved
by introducing the unimodularity constraint to Eq. (2.5.7) via a Lagrange multiplier,

$$W(\omega_0) \to \widetilde{W}(\omega_0, \lambda) = \int_a^b 12(\omega - \omega_0)^2 A(\omega, \omega_0)^2 d\omega - \lambda \left[\int_a^b A(\omega, \omega_0) d\omega - 1 \right]. \tag{2.5.9}$$

The coefficients which minimise the criterion are then given by

$$c_\tau(\omega_0) = \frac{\sum_{\tau'} \widetilde{\mathcal{K}}_{\tau\tau'}^{-1}(\omega_0) \widetilde{\mathcal{C}}_{\tau'}}{\sum_{\tau,\tau'} \widetilde{\mathcal{C}}_\tau \widetilde{\mathcal{K}}_{\tau\tau'}^{-1}(\omega_0) \widetilde{\mathcal{C}}_{\tau'}}, \tag{2.5.10}$$

where we define the constraint vector

$$\widetilde{\mathcal{C}}_\tau = \int_a^b K(\tau, \omega) d\omega, \tag{2.5.11}$$

and the kernel weight matrix

$$\widetilde{\mathcal{K}}_{\tau\tau'}(\omega_0) = 24 \int_a^b (\omega - \omega_0)^2 K(\tau, \omega) K(\tau', \omega) d\omega. \tag{2.5.12}$$

We shall now discuss the same minimisation procedure on the least-squares criterion given in Eq. (2.5.8). Differentiating with respect to the Backus-Gilbert coefficients yields a more compact solution:

$$\partial_{c_{\tau'}} J(\omega_0) = 2 \int_a^b K(\tau', \omega) \left[A(\omega, \omega_0) - \delta(\omega - \omega_0) \right] d\omega \tag{2.5.13}$$

$$= 2 \sum_\tau \int_a^b c_\tau(\omega_0) K(\tau, \omega) K(\tau', \omega) d\omega - K(\tau', \omega_0). \tag{2.5.14}$$

As can be seen, there is no trivial solution for c_τ and thus no explicit need for a unimodularity condition. Setting $\partial_{c_{\tau'}} J(\omega_0) = 0$ then yields

$$\sum_\tau \int_a^b c_\tau(\omega_0) K(\tau, \omega) K(\tau', \omega) d\omega = K(\tau', \omega_0), \tag{2.5.15}$$

$$c_\tau(\omega_0) = \sum_{\tau'} \mathcal{K}_{\tau\tau'}^{-1} \mathcal{C}_{\tau'}(\omega_0), \tag{2.5.16}$$

where we now define the corresponding width matrix and constraint vector

$$\mathcal{K}_{\tau\tau'} = \int_a^b K(\tau, \omega) K(\tau', \omega) d\omega, \tag{2.5.17}$$

$$\mathcal{C}_\tau(\omega_0) = K(\tau, \omega_0). \tag{2.5.18}$$

One may now see an advantage of using the least-squares criterion over the spread criterion: the spread criterion has the dependence on the sampling point ω_0 encoded into the matrix $\mathcal{K}$, whereas the least-squares criterion has the ω_0 dependence in the vector-like $\mathcal{C}$. This observation translates into a dramatic computational speed-up, as the least-squares criterion only requires one inversion of $\mathcal{K}$ (which is highly-singular and poorly conditioned) for the entire sampling window $\{\omega\}$. However, one disadvantage of the least-squares criterion is that the lack of unimodularity of the averaging functions destroys the vertical scaling of the reconstruction. This means that one cannot re-create the input data, $g(\tau)$, from the reconstructed spectrum, $\hat{f}(\omega)$. This creates a dilemma, as explicitly reintroducing the unimodularity condition moves the ω_0 dependence back into the matrix $\mathcal{K}$, removing the speed-up. This tension between fidelity and reconstruction speed is not the only aspect to be consid-

ered, however, as each of the two approaches yield differing reconstructions. A more complete discussion of the reconstructive differences between the two approaches is detailed in §2.5.1.

At a first glance, the Backus-Gilbert method proves an attractive technique for spectral reconstruction as it requires few assumptions to be made about the form of both the input data, $g(\tau)$, or the target function, $f(\omega)$. It is also algebraic in its estimation of $f(\omega)$, with (in theory) only the number of observations, τ, dictating the quality of the reconstruction.

In the following sections, we study both the strengths and weaknesses of the method, with a particular focus on the means by which the averaging functions construct our estimate of the target function, $f(\omega)$. which arises from the spread criterion.

2.5.1 ON THE RECONSTRUCTIVE POWER OF THE SPREAD AND LEAST-SQUARES CRITERIA
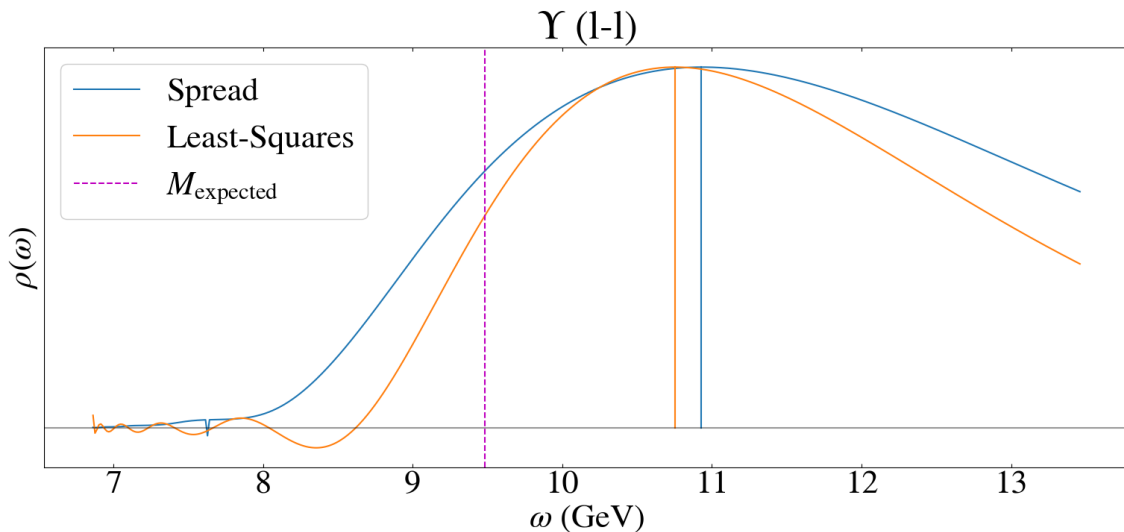
Figure 2.1: Comparison of spectral density functions created by the spread (Eq. (2.5.7)) and least-squares (Eq. (2.5.8)) criteria. The magenta line denotes the expected peak position for the ground state using exponential fits to the correlator, the calculation of which is outlined in §3.2. The coloured vertical lines represent the peak location for the spectrum. In this example, we compare density functions constructed from the Υ meson correlator using local quark sources (see §3.3 for further details).

The choice to use the least-squares criterion (Eq. (2.5.8)) over the spread criterion (Eq. (2.5.7)) is motivated not only by the significant computational speed-up (see Appendix B.2) but also by the reconstructive power of the averaging functions. Figure 2.1 shows the difference between the reconstructions produced by each of the two criteria.
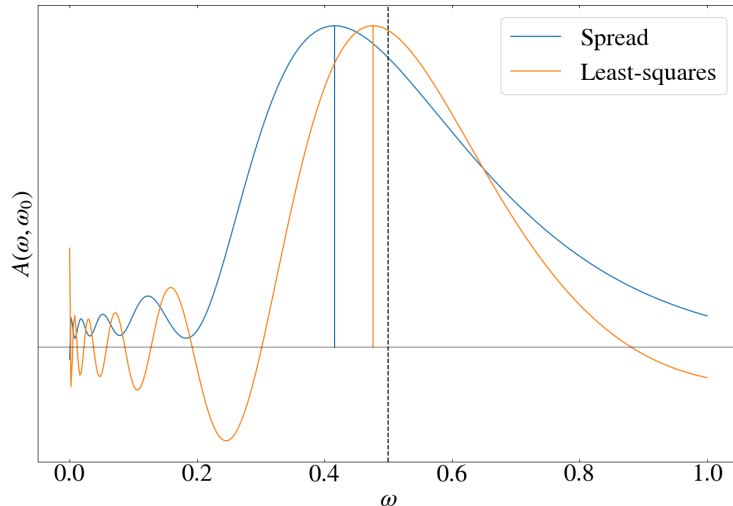
Figure 2.2: Comparison of the averaging functions produced by the least-squares and spread criteria. The vertical dashed line is the sampling point ω_0 about which we expect the averaging function to be constructed, and the coloured dropped lines represent the peak of $A(\omega, \omega_0)$ calculated via $\mathrm{argmax}_\omega(A(\omega, \omega_0))$. Here we show ω as a fraction of the sampling window $\{\omega\}$.

Figure 2.2 shows the localisation error of a sample averaging function for both criteria. The localisation error is defined as the difference between the desired sample point, ω_0, and the peak position of the averaging function, given by $\mathrm{argmax}_\omega[A(\omega, \omega_0)]$ (represented by the coloured drop-lines in the figure). Fig. 2.3 shows the localisation error as a function of the sampling point ω_0 for both the least-squares (Fig. 2.3-*Left*) and spread (2.3-*Right*) criteria. In Fig. 2.3 we can see that for both criteria the averaging functions have a systematic negative shift (which in turn will carry forward into the reconstructed spectrum), however this error is significantly greater for the spread criterion than the least-squares.

It is important to reduce this localisation error wherever possible, as the negative shift in the peak position relative to the sample point ω_0 means that the averaging functions sample the underlying spectrum at some ω_0 less than the desired value. In the reconstructed spectrum, this manifests as a noticeable shift in the energy of the ground and excited states.

One disadvantage of the least-squares criterion, however, is that the lack of unimodularity of the averaging function destroys the information relating to the scale of $\rho(\omega)$, meaning that the correlator cannot be reconstructed via Eq. (2.2.14). This reconstruction procedure is useful in characterising the systematic errors in the method. It is for this reason that the Backus-Gilbert method using the least-squares
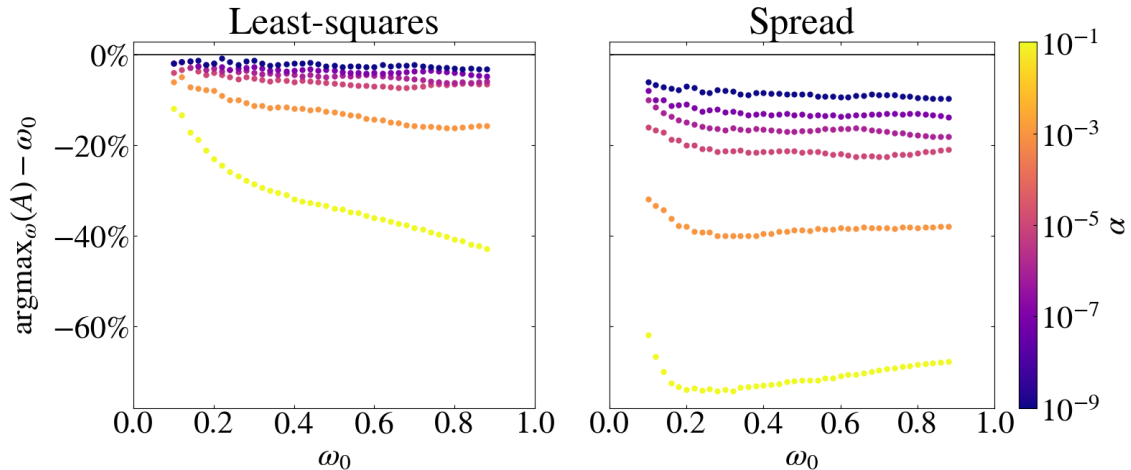
Figure 2.3: Comparison of the offset between sampling position ω_0 (as a fraction of the sampling window) versus the peak position of $A(\omega, \omega_0)$ for both the least-squares and spread criteria. The whitening parameter α represents the strength of the conditioning applied to the weight matrix $\mathcal{K}$ and is defined in Eq. (2.6.4).

criterion is sometimes referred to in the literature as a spectral 'appraisal' method as only the shape of the spectral features are preserved.

Related Work

As with the spread criterion, modifications to the least-squares criterion also exist in the literature. One popular modification (not studied in this work) which has arisen in recent years is the Hansen-Lupo-Tantalo (HLT) method [60], where the $\delta(\omega - \omega_0)$ of Eq. (2.5.8) is replaced by some narrow function centred about ω_0 with a defined width σ (e.g. $\mathcal{N}(\omega_0, \sigma)$). This width is then generally made a function of the position in the sampling window, allowing one finer control over the width of the averaging functions.

2.6 Weight Matrix Whitening and Inversion

Due to the exponential nature of the NRQCD kernel $K(\tau, \omega) = e^{-\omega\tau}$, the weight matrix becomes further ill-conditioned as the number of observations τ increases. This singular behaviour can be observed during the calculation of $\mathcal{K}^{-1}$ via singular-value decomposition (SVD):

$$\mathcal{K} = U\Sigma V^T, \tag{2.6.1}$$

$$\Rightarrow \mathcal{K}^{-1} = V\Sigma^{-1}U^T, \tag{2.6.2}$$
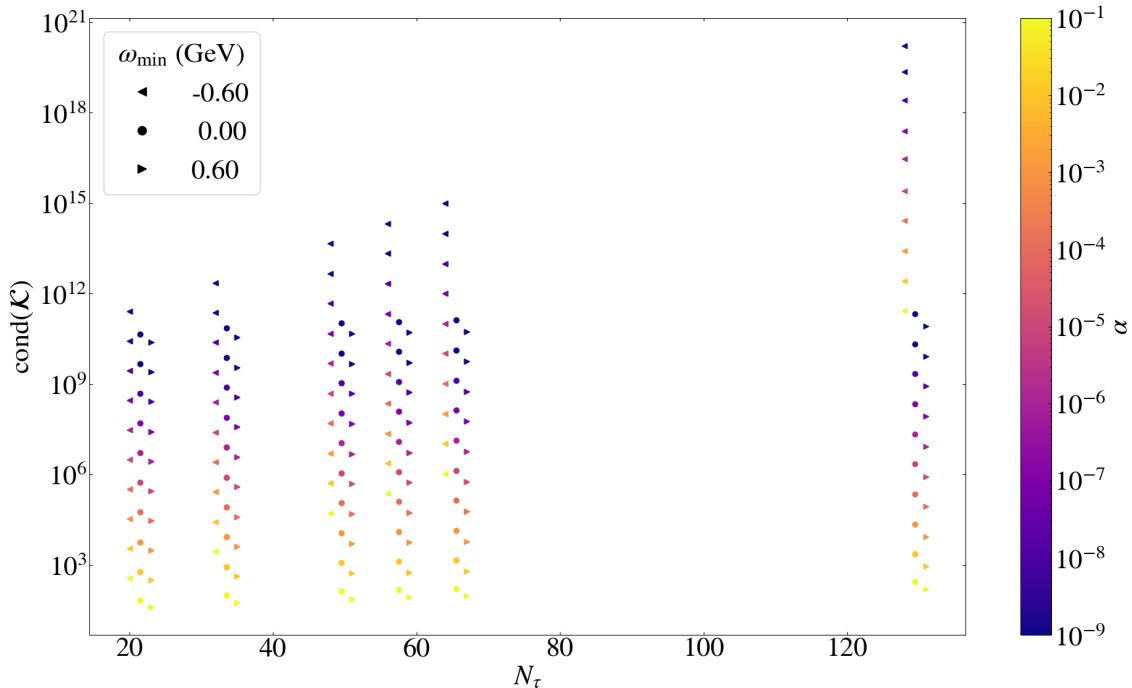
Figure 2.4: Least-squares weight matrix condition number, cond($\mathcal{K}$), versus temporal extent, N_τ, for a range of whitening factor values, α, and choices of $\omega_{\min}$, where we have added a small stagger to each N_τ so that differences in $\omega_{\min}$ are visible. Notice the sudden increase in the condition as a function of N_τ when $\omega_{\min} < 0$.

where Σ is the diagonal matrix of singular values σ_i and U, V are, respectively, the left and right singular, orthogonal vectors of $\mathcal{K}$.

One method of conditioning $\mathcal{K}^{-1}$ is via the inclusion of an additive noise term in the form of the covariance matrix of the input data $G(\tau)$:

$$\mathcal{K}(\alpha) = \alpha\mathcal{K} + (1 - \alpha)\mathrm{Cov}[G(\tau)], \qquad (2.6.3)$$

where α is known as the whitening factor or parameter and controls the strength of the regularisation. Figure 2.4 shows the condition number (defined as cond($\mathcal{K}$) = $\max(\sigma_i)/\min(\sigma_i)$) as a function of the temporal extent, N_τ, and the whitening factor, α. Another similar approach is to regularise $\mathcal{K}$ via the addition of a small, diagonal contribution [45]

$$\mathcal{K}(\alpha) = \mathcal{K} + \alpha\mathbb{1}. \qquad (2.6.4)$$

This acts in a similar manner to Tikhonov regularization or ridge regression (see Appendix A.3 for details) to increase the singular values, σ_i, in a manner such that the smallest singular values are regularised the most, resulting in a smaller condition number.

Both Eqs. (2.6.3) and (2.6.4) are valid ways of treating the ill-condition of $\mathcal{K}^{-1}$ and each allow one to regulate the balance between the resolution width, ε, created by the kernel function and the resulting reconstruction error, $\Delta\rho$, given by

$$\Delta\rho^2(\omega_0) = \sum_{\tau,\tau'} c_\tau(\omega_0)\text{Cov}[G]_{\tau\tau'}c_{\tau'}(\omega_0). \qquad (2.6.5)$$

The methods for determining the critical value of α which simultaneously minimises ε and $\Delta\rho$ vary in the literature [51, 53, 55, 62, 63]. One issue which plagues this condition is that the definition of ε is ambiguous, and furthermore depends strongly on the choice of width criteria (*cf.* Eqs. (2.5.7) and (2.5.8)). The values of ε and $\Delta\rho$ also do not generally vary on the same scale, which means that a small change in α can yield a large change in both ε and $\Delta\rho$, which requires one to perform reconstructions at several values of α to characterise the dependence of ε and $\Delta\rho$.

In this work, we posit that there is no rigorously defined approach to finding the optimal value of α, and so we shall treat it in this work as a free parameter, the dependence on which must be removed in our final analysis. We also opt to use the form outlined in Eq. (2.6.4) (which we refer to as 'Tikhonov' whitening) for treating $\mathcal{K}^{-1}$. This approach has the added benefit of not explicitly introducing noise from the input data into the determination of c_τ, enabling one to use the same set of coefficients for any data which shares the same kernel function $K(\omega,\tau)$, hence reducing computation time.

Other traditional approaches to matrix inversion, such as Gauss-Jordan elimination, are unsuitable for use with near-singular matrices as they suffer from compounding numerical error [64]. In practise, the smallest singular values of Σ may be zero to within machine precision, causing the reciprocal matrix Σ^{-1} to become singular and $\mathcal{K}^{-1}$ be undefined. In this case, it is acceptable to use a generalised form of the inverse, known as the Moore-Penrose pseudoinverse [65, 66]:

$$\mathcal{K}^+ = V\Sigma^+U^T, \qquad (2.6.6)$$

where we define

$$\Sigma_{ii}^+ = \begin{cases} 1/\sigma_i & \text{if } \sigma_i > \varepsilon \\ 0 & \text{otherwise} \end{cases}, \qquad (2.6.7)$$

with ε (not to be confused with the resolution width, also denoted ε in the literature)

the smallest value representable by the computer (i.e. the machine precision). In
this work, we use quadruple precision (128 bits) for the SVD, which corresponds to
a numerical precision of 2^{113} or 34 decimal places.

2.7 INVESTIGATIONS INTO THE RESOLVING POWER

As highlighted in §2.5, one of the strengths of using a technique such as the Backus-
Gilbert method is that one can gain a fairly good understanding of the resolving
power before any data is introduced to the model. From Eq. (2.5.4) we know that
a well-resolved spectrum is produced when the sampling functions, $A(\omega, \omega_0)$, are a
good approximation to $\delta(\omega - \omega_0)$. However, when a finite number of kernel func-
tions are used as a basis for the construction of the averaging functions, $A(\omega, \omega_0)$,
one finds that not only do the functions not correctly describe $\delta(\omega - \omega_0)$, but that
the characteristics of the function (such as peak position and width) also acquire
some dependence on the relative position of the sample point, ω_0, within the re-
construction window, $\{\omega\}$. This behaviour is first noticeable in the width criterion
comparison in Fig. 2.3. Figure 2.5 shows $A(\omega, \omega_0)$ (black) at two different values of
ω_0 (left-right) and α (top-bottom). The blue and orange lines are Gaussian fits to
the leading and trailing edges of $A(\omega, \omega_0)$, respectively, and highlight the asymme-
try of the function. This asymmetry can result in reconstruction artefacts such as
smearing which worsens towards higher energies in the sampling window or improper
location of the ground state peak in energy space.

The degree of asymmetry and improper location of the averaging functions may
be measured by fitting a Gaussian curve to the upper half of the leading and trailing
edges of $A(\omega, \omega_0)$ (the upper half is used so as to ignore contributions from the nega-
tive side-lobes in the lower halves). This fitting procedure is shown in Fig. 2.5, where
we fit the leading and trailing edges of a sample averaging function $A(\omega, \omega_0)$ early
and late in the time window at strong ($\alpha = 10^{-3}$) and weak ($\alpha = 10^{-6}$) whitening.
Here we see that the width of the averaging function depends strongly on its position
in the sampling window, ω_0, and that the localisation error, $\text{argmax}_\omega(A) - \omega_0$, is
larger for strong whitening.

We now extend this process to the entire time window, comparing the values for
the mean, μ_A, and width, Γ_A, for the leading ($\mathcal{N}^L$) and trailing ($\mathcal{N}^T$) fits. Figure
2.6-*Left* shows the mean of the Gaussian fits while 2.6-*Right* shows the difference in
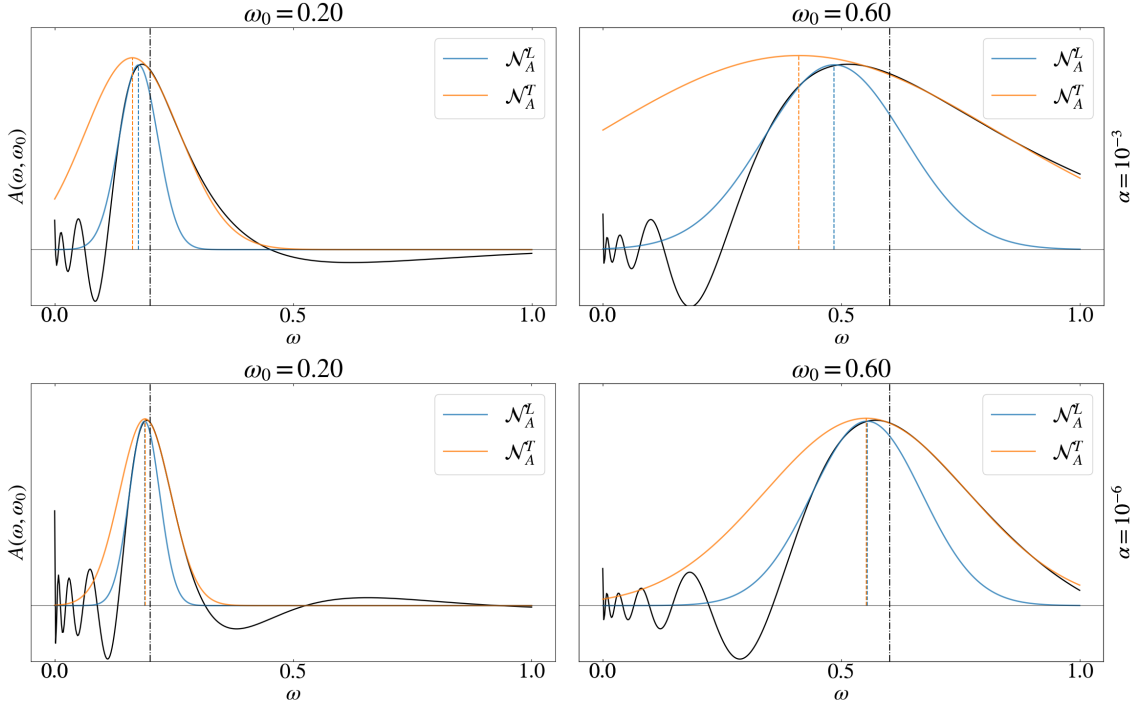
Figure 2.5: Comparison of leading and trailing edge Gaussian fits to averaging functions $A(\omega, \omega_0)$ located at $\omega_0 = 0.2$ and $\omega_0 = 0.6$ (as a fraction of the total sampling window $\{\omega\}$) for two values of the whitening parameter, $\alpha = 10^{-3}$ (*Top*) and $\alpha = 10^{-6}$ (*Bottom*). The correlator time window used to construct the $A(\omega, \omega_0)$ is $\tau \in [1, 128)$. The blue and orange curves correspond to the leading and trailing edge Gaussian fits, $\mathcal{N}_A^L$ and $\mathcal{N}_A^T$, respectively. The corresponding coloured vertical lines are the means, $\mu_A^{[L/T]}$, associated with each fit, $\mathcal{N}_A^{[L/T]}$.
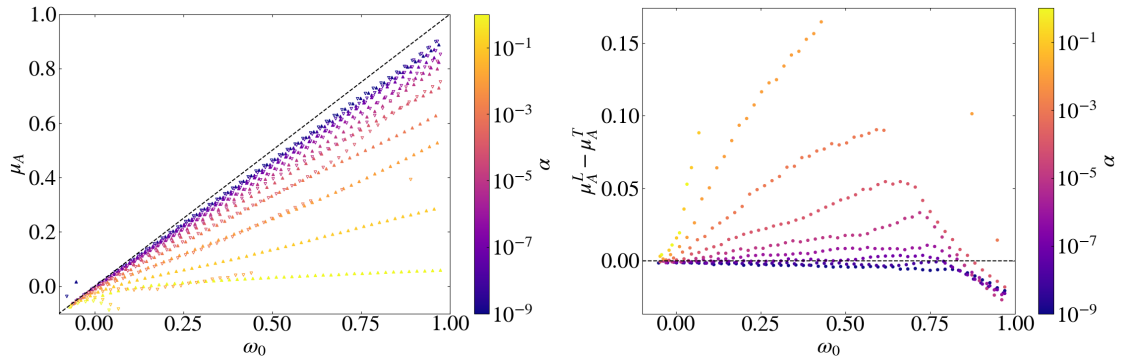
Figure 2.6: *Left*: The fit mean, μ_A, as a function of the sampling window position, ω_0, for the leading and trailing edges of $A(\omega, \omega_0)$ and for a range of whitening parameter values, α (shown by colour). The dashed line represents the idealised case where $A(\omega, \omega_0)$ is perfectly located (i.e. $\mu_A = \omega_0$). *Right*: The asymmetry measure $\mu_A^L - \mu_A^T$ as a function of the sampling window position ω_0. For both plots, the time window used was $\tau \in [1, 128)$.

Table 2.1: Particle Data Group (PDG) values [2] for the ground state mass M and width Γ of a choice of bottomonium states. We note that no width is reported for the h_b (1S) meson.

	η_b (1S)	Υ (1S)	χ_{b1} (1P)	h_b (1P)
M (MeV)	9398.0 ± 3.2	9460.30 ± 0.26	$9892.78 \pm 0.26 \pm 0.31$	9899.3 ± 0.8
Γ (MeV)	$10.8^{+4.0}_{-3.7}{}^{+4.5}_{-2.0}$	54.02 ± 1.25	129.64 ± 0.33	$-$

the means for the leading and trailing fits. Figure 2.7 shows the same information for the width of the Gaussian fits.

Figures 2.6 and 2.7 confirm that there is a strong dependence of the averaging function width Γ_A and the localisation error on both the position in the sampling window and the whitening factor. However, we also see that the asymmetry of the averaging functions probed by $\mu_A^L - \mu_A^T$ and $\Gamma_A^L - \Gamma_A^T$ also worsens as a factor of both the position and whitening. Each of these effects will influence the resulting spectrum and cause not only a smearing of spectral features, but also a non-trivial shift, as described by Eq. (2.5.4).

This form of analysis is critical before attempting a reconstruction using the method as we can make an *a priori* estimate of the maximum resolving power and potential systematic effects of the method, before the introduction of observational data.

Comparing the values for Γ_A in Table 2.1 with those in Fig. 2.7 we can immediately see that the method will be incapable of resolving the ground state width at the position along the sampling window which corresponds to the particle masses.
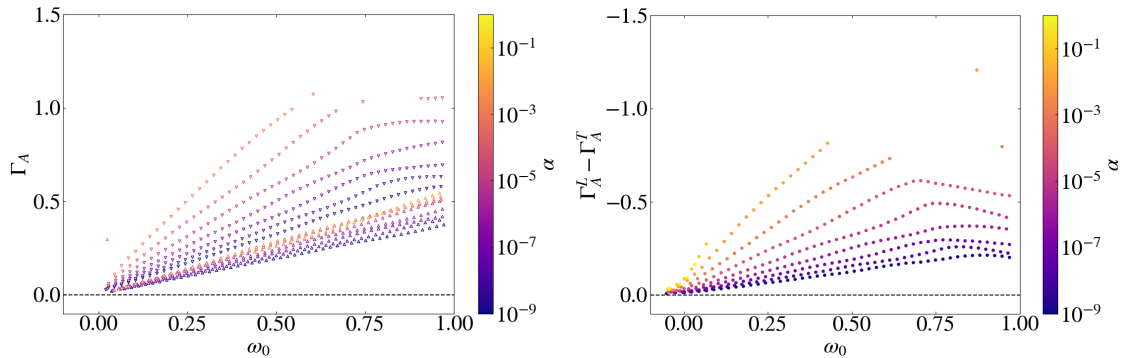
Figure 2.7: *Left*: The fit width, Γ_A, as a function of the sampling window position, ω_0, for the leading and trailing edges of $A(\omega, \omega_0)$ and for a range of whitening parameter values, α (shown by colour). *Right*: The asymmetry measure $\Gamma_A^L - \Gamma_A^T$ as a function of the sampling window position ω_0. For both plots, the time window used was $\tau \in [1, 128)$.

However, we shall outline in §2.8 a possible improvement method for increasing the resolution width (of which Γ_A is a proxy) of the averaging functions.

Another variable which strongly influences the resolving power is the number of observations, $g(\tau)$, as can be seen by the critical assumption made in Eq. (2.5.6). If we expect our averaging functions to produce a more faithful reconstruction as the number of basis components (equal to the number of observations $g(\tau)$) increases, then lattices which have access to fewer observations (as is the case with high temperatures) will have poorer resolving power. However, one cannot arbitrarily increase the number of observations (either via probing colder lattices or larger anisotropies) due to the Moore-Penrose term in Eq. (2.6.7). This tension between machine and theory arises due to the finite precision with which computers operate – increasing the number of observations broadens the separation in scale between the highest and lowest singular values. The information contributed by the largest-time observations will be so vanishingly small that the Backus-Gilbert method will require exponentially increasing precision in order to avoid the information cutoff introduced by the Moore-Penrose term. This increase in singular behaviour can be treated via the prescription outlined in §2.6, but at the cost of broadening the averaging functions (see Fig. 2.7). Thus, we anticipate that there exists some maximal 'saturation' of the resolving power at some τ_2 large. The effects of such a time-window dependence will be further discussed and treated in §3.7.

2.8 LAPLACE SHIFTING

As discussed in the previous section, Figs. 2.6 and 2.7 show that the reconstruction errors are small early in the sampling window. One benefit of the spectral reconstruction problem being of the Laplacian form is that we may take advantage of the corresponding transform rules to improve the resolution of our reconstruction routine. Consider again the form of the reconstruction problem:

$$G(\tau) = \int \rho(\omega)e^{-\omega\tau}d\omega. \tag{2.8.1}$$

One may imagine two possible methods of obtaining $\rho(\omega)$ from $G(\tau)$. First, consider the case where we invert Eq. (2.8.1) using an ideal inverse Laplace transform. Figure 2.8 depicts the operation of two possible reconstruction methods. The first (and trivial) approach is marked path A in red, where we may simply take the inverse Laplace transform of $G(\tau)$ to get $\rho(\omega)$ directly. Alternatively, we may follow path B, marked in blue, whereby we multiply the correlator by $e^{\Delta\cdot\tau}$ before taking the inverse transform to obtain the shifted spectrum $\rho(\omega-\Delta)$, using the transformation property

$$e^{\Delta\cdot\tau}G(\tau) \stackrel{\mathcal{L}^{-1}}{\Longrightarrow} \rho(\omega-\Delta). \tag{2.8.2}$$

The shifted spectrum is then related to $\rho(\omega)$ by a trivial shift in ω. We emphasise that in the case of an ideal inverse Laplace transform, both paths A and B are equivalent.

We now discuss the case where the ideal inverse transform is instead replaced by the approximation provided by the Backus-Gilbert method. Figure 2.9 depicts the operation of the two previously-discussed approaches in the Backus-Gilbert case. Path A now produces the estimate for the spectrum via a convolution of the correlator with the Backus-Gilbert coefficients. Path B again involves multiplying $G(\tau)$ by $e^{\Delta\cdot\tau}$ which, if the Backus-Gilbert approximation to the inverse transform is sufficiently close, yields the shifted spectrum. However, we now find that a trivial shift *does not* return the spectrum predicted by path A. The spectrum predicted by path B is shown in Figs. 2.10 and 2.11.

This distinction arises because the Backus-Gilbert coefficients are themselves invariant under Eq. (2.8.2), which means that the averaging functions are also unchanged. Recalling the way in which we obtain estimates of the spectrum from the

$$G(\tau) \xrightarrow{\times e^{\Delta \cdot \tau}} e^{\Delta \cdot \tau} G(\tau)$$

$$\mathcal{L}^{-1}\{G(\tau)\} \qquad \boxed{A = B} \qquad \mathcal{L}^{-1}\{e^{\Delta \cdot \tau} G(\tau)\}$$

$$\rho(\omega) \xleftarrow{(\omega - \Delta) \to \omega} \rho(\omega - \Delta)$$
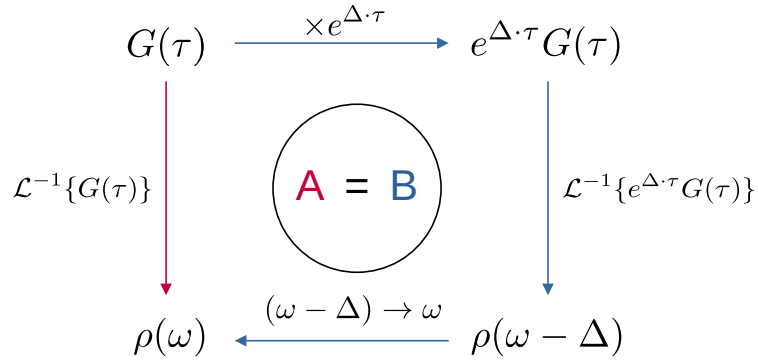
Figure 2.8: Diagram demonstrating two methods for obtaining the spectral density function, $\rho(\omega)$, from the correlator, $G(\tau)$, using the inverse Laplace transform, $\mathcal{L}^{-1}\{\cdot\}\}$.

$$G(\tau) \xrightarrow{\times e^{\Delta \cdot \tau}} e^{\Delta \cdot \tau} G(\tau)$$

$$\sum_{\tau} c_{\tau} G(\tau) \quad \text{BG} \qquad \boxed{A \neq B} \qquad \text{BG} \quad \sum_{\tau} c_{\tau} e^{\Delta \cdot \tau} G(\tau)$$

$$\rho(\omega) \xleftarrow{(\omega - \Delta) \to \omega} \times \rho(\omega - \Delta)$$
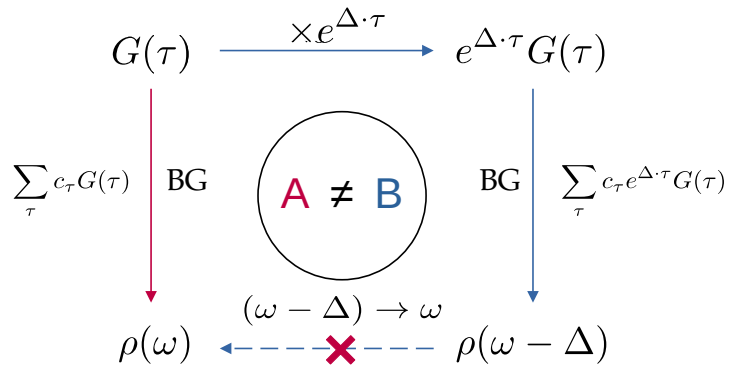
Figure 2.9: Diagram demonstrating two methods for obtaining the spectral density function, $\rho(\omega)$, from the correlator, $G(\tau)$, using the Backus-Gilbert approximation to the inverse Laplace transform, denoted by BG.

averaging functions, as shown in Eq. (2.5.4), our reconstructed spectrum would be
unaffected if it were not for the fact that the $A(\omega, \omega_0)$ have a width which changes
as a function of ω_0, as shown in Figure 2.7. Thus, by shifting our value of $G(\tau)$
before convolution with the Backus-Gilbert coefficients, we may shift the features of
interest of the spectrum into a sampling region with narrower averaging functions,
thus improving the resolution of the reconstruction. This improvement is shown in
Figs. 2.10 and 2.11 where the improvement due to successively stronger shifts is now
readily seen.
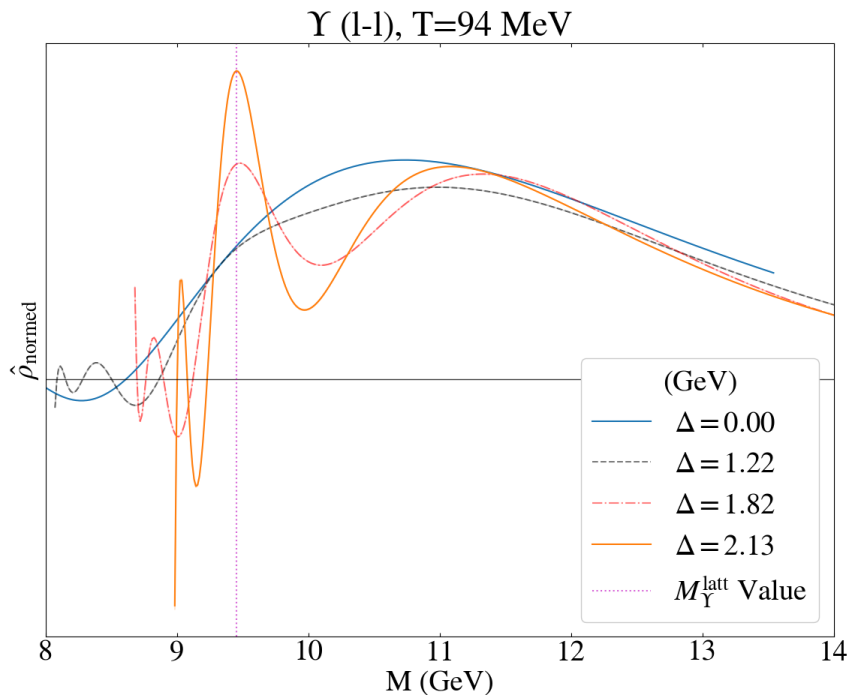
Figure 2.10: Graph of the baseline reconstruction from Backus-Gilbert (blue) compared
with Laplace-shift improved spectra (orange) for the Υ meson. In this example, $\alpha = 10^{-2}$.
Here the error bars are too small to be seen as the FASTSUM NRQCD correlators have
small statistical errors.

One drawback of shifting the correlator is that the error also grows proportionally
with the shift (as can be seen in Fig. 2.11). Given a linear combination of the form
Eq. (2.5.2), the error in $G(\tau)$ is propagated to the spectral estimate via

$$\Delta\hat{\rho}^2(\omega_0) = \sum_{\tau,\tau'} c_\tau(\omega_0)\text{Cov}[G(t)]_{\tau\tau'}c_{\tau'}(\omega_0). \qquad (2.8.3)$$

Under the Laplace shift, the covariance matrix is pre- and post-multiplied by a
factor of $e^{\Delta\cdot\tau}$, which causes small fluctuations in $G(\tau)$ to be magnified. This effect
is especially apparent at small values of the whitening factor, α, as the values of
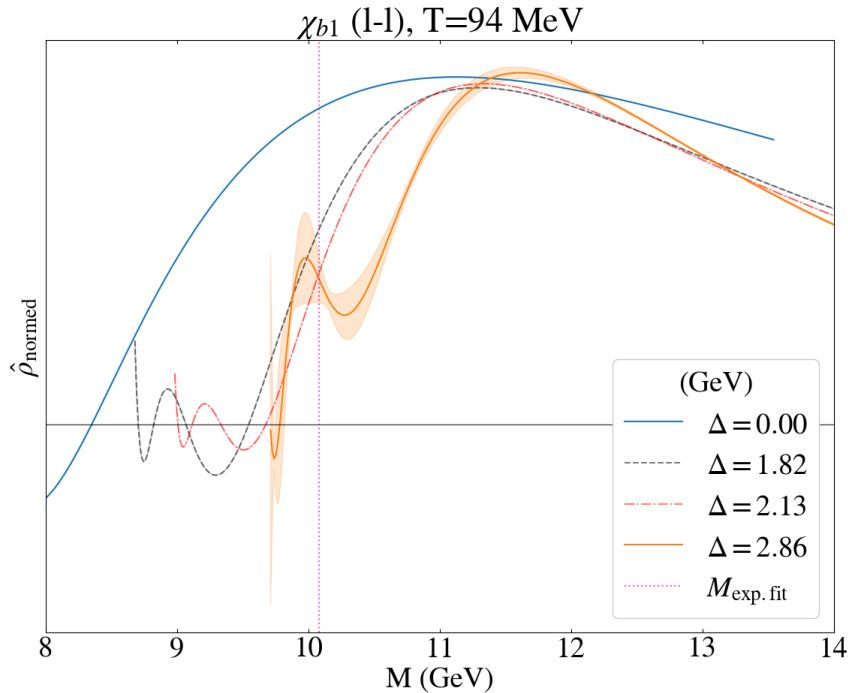
Figure 2.11: Graph of the baseline reconstruction from Backus-Gilbert (blue) compared with Laplace-shift improved spectra (orange) for the χ_{b1} meson. In this example, $\alpha = 10^{-2}$. Note that the statistical error has been drastically magnified for large Δ, in contrast with Fig. 2.10.

$c_\tau(\omega_0)$ at large τ become large and oscillatory.

In the following results section we apply the Laplace shift improvement routine to our reconstruction of $\rho(\omega)$, treating Δ as a free parameter. The maximum theoretical shift is that which brings the ground state peak to the edge of the window, given by $\Delta = M - \omega_{\min}$ where M is the ground state mass and $\omega_{\min}$ is the minimum of the reconstruction window. To facilitate any comparisons with data with differing $\omega_{\min}$, we define the 'global' shift $\widetilde{\Delta} = \Delta + \omega_{\min}$. We note here that Δ and $\widetilde{\Delta}$ also are subject to the addition of the NRQCD energy shift, E_0, just as with the estimate for the ground state mass, M. This shift is explicitly added from this point forward to enable direct comparisons between the shift value and the mass, which will be necessary for the analysis in Chapter 3.

In this chapter, we have outlined the operation of the Backus-Gilbert method and briefly discussed its strengths and shortcomings in the context of spectral reconstruction. We then explored a potential improvement scheme which exploits the non-uniformity of the averaging functions to enhance our estimates for the ground state mass and width.

2.9 ON THE RELATIONSHIP BETWEEN THE LAPLACE SHIFT AND $\omega_{\min}$

In §2.2 we derived the spectral representation of the (relativistic) correlator and took the non-relativistic limit, $M \gg T$. In this form, the inverse transform, given by Eq. (2.2.18), acquires a negative lower bound which corresponds to the mass of the state. In the case of bottomonia this lower bound, $\omega_{\min}$, corresponds to $M = 2M_b$. In practise, we allow the lower bound to vary to account for renormalization effects in the bottom quark mass and the NRQCD energy shift.

It has previously been suggested that for reconstruction techniques which are based upon a basis-function construction approach, such as the maximum entropy method (MEM), there may be a dependence on the resolving power of the resolution functions (or equivalent components) and the position of the reconstructed feature in relation to the start of the sampling window [67]. This study showed that the resolution capabilities of a particular method could be inferred by inspecting the resolution functions in an SVD basis, where the width of a particular feature was shown to acquire an increasing artificial contribution as the feature is moved to the end of the reconstruction window. This particular feature is prevalent in reconstruction routines which adopt a choice of basis functions and has been invoked as a motivation for the creation of the Bayesian Reconstruction (BR) method [48, 68].

In our work, we have probed the effect of changing $\omega_{\min}$ and its relation to the Laplace shift. Figures 2.12 and 2.13 show the predicted value for the ground state mass, M, and full width at half-maximum (hereafter denoted FWHM), respectively, versus the value of $\omega_{\min}$ for the η_b meson at $T = 189$ MeV and $T = 47$ MeV for a range of whitening values. Overall, we did not find any appreciable difference in the central value for the mass when changing $\omega_{\min}$ through the range $\omega_{\min} \in [-0.1, -0.05, 0.025, 0, 0.025, 0.05, 0.075] \, a_\tau^{-1}$ (or in energy units, $\omega_{\min} \in [-0.6, 0.46]$ GeV)– the only discernible effects are a small reduction in the error at small α for increasingly positive $\omega_{\min}$ at the expense of fit convergence failure at large α. However, there is a reduction in the ground state width with increasing $\omega_{\min}$ at the higher temperature, consistent with the argument that bringing $\omega_{\min}$ closer to the ground state improves the resolution. This result is partly supported by previous work [69] which showed a dependence of both the mass and width on $\omega_{\min}$.

We do note that pushing $\omega_{\min}$ too far in either direction is inappropriate. When
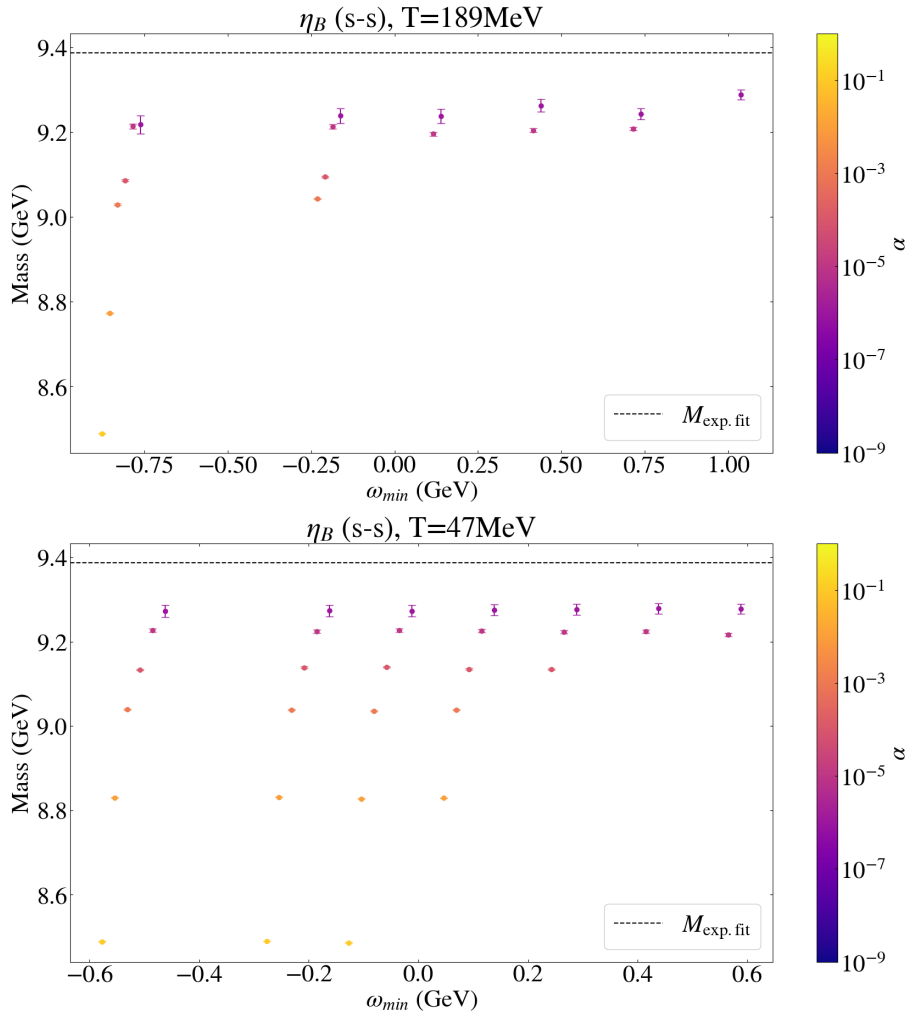
Figure 2.12: Plot showing the predicted ground state mass, M, versus $\omega_{\min}$ for the η_b (s-s, see §3.3) meson at $T = 189$ Mev (*Top*) and $T = 47$ MeV (*Bottom*). The colour of the data points represents the whitening factor values, α.

$\omega_{\min}$ is too negative the ground state will be far into the sampling window where the resolving functions are broad and Laplace shifting will break down before reaching $\omega_{\min}$. An $\omega_{\min}$ too positive is usually more unstable for large α and risks cutting into the peaks of the spectrum or missing the ground state completely. This can be seen especially at $T = 189$ MeV in Fig. 2.12, where no estimates could be calculated at large α. Empirical testing suggests that $\omega_{\min} = -0.1 a_\tau^{-1} \approx -0.6$ GeV yields a nice balance between the aforementioned arguments.
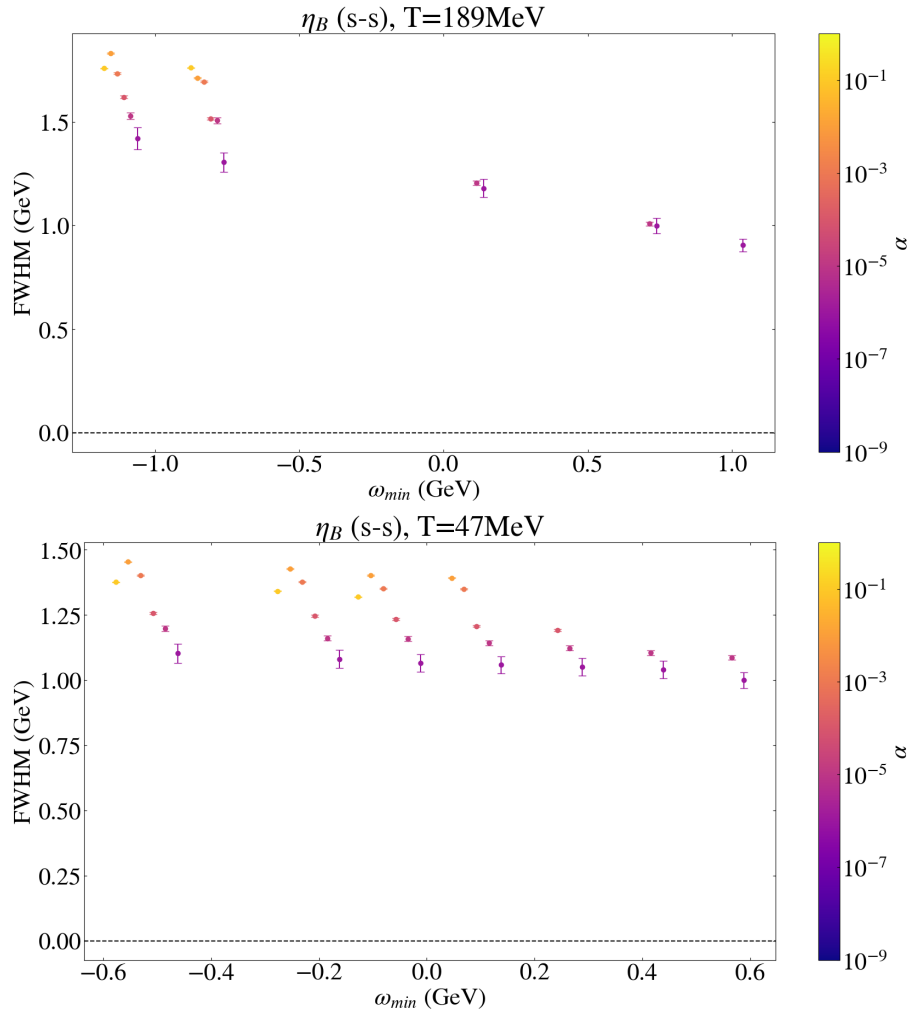
Figure 2.13: Plot showing the predicted ground state FWHM width versus $\omega_{\min}$ for the η_b (s-s, see §3.3) meson at $T = 189$ MeV (*Top*) and $T = 47$ MeV (*Bottom*). The colour of the data points represents the whitening factor values, α.

RESULTS: BOTTOMONIUM SPECTRAL RECONSTRUCTION

In the following chapter we outline the details of the FASTSUM anisotropic NRQCD ensembles, before presenting Backus-Gilbert estimates of the mass and width for a select variety of bottomonia channels. We focus in particular on the s and p-wave channels simulated with both local and smeared quark sources, presenting a comparison between the two. We begin by briefly discussing the estimates for the ground state mass and width obtained using the original (henceforth named 'unshifted') Backus-Gilbert method, before presenting results obtained after the introduction of the Laplace shift improvement scheme.

3.1 DETAILS OF THE FASTSUM ENSEMBLES

This analysis makes use of the FASTSUM collaboration's anisotropic Gen-2L ensembles which employ clover-improved [30], dynamical Wilson fermions ($N_f = 2 + 1$) and has a Symanzik-improved gauge action [70]. The ensembles cover a broad range of temperatures (see Table 3.1 for detail) spanning the pseudocritical transition $T_{\mathrm{pc}} \approx 167$ MeV [4, 5]. The lattice is anisotropic, with a space-time anisotropy of $\xi = a_s/a_\tau = 3.453(6)$ [71] with $a_s = 0.11208(31)$ fm. The pion mass is heavier-than-nature at $M_\pi = 239(1)$MeV [72].

3.2 COMMENTS ON COMPARISONS WITH EXPERIMENT

As previously discussed in §1.6, the non-relativistic lattice formalism for QCD is additively renormalized and as such requires some reference energy with which the scale may be set. In the FASTSUM ensembles the energy shift E_0 is calculated by

Table 3.1: Temporal extent, corresponding lattice temperature in MeV and number of configurations for the FASTSUM Generation 2L ensembles. The double vertical line mid-table separates the temperatures according to our value of $T_{\mathrm{pc}} \approx 167\mathrm{MeV}$[4, 5].

N_τ $(N_s = 32)$	128	64	56	48	40	36	32	28	24	20
$T = 1/(a_\tau N_\tau)$ [MeV]	47	95	109	127	152	169	190	217	253	304
N_{cfg}	1024	1041	1042	1123	1102	1119	1090	1031	1016	1030

comparing [37] the spin-averaged mass of the 1S state with the value obtained from experiment [2]. If one assumes that the spectrum of ground state of a particle is given by $\delta(\omega - M)$ (and neglecting contributions from higher energy states), then by the spectral representation of the correlator (Eq. (2.2.18)) one finds that

$$G(\tau) \approx e^{-M\tau}. \tag{3.2.1}$$

Figure 3.1-*Top* shows the value of $G(\tau)$ for the Υ meson for two types of quark sources (see §3.3) at $T = 94$ MeV. The vertical scale is logarithmic, and we can see that at large τ/a_τ the log of the correlator is linear in the lattice time, which is expected when the ground state becomes dominant.

Although one may directly fit Eq, 3.2.1 with a simple exponential for M, it is customary in the literature to instead measure a proxy for the mass, given by

$$M_{\mathrm{eff}}(\tau) = -\partial_\tau \log G(\tau) = -\langle \omega \rangle_\rho, \tag{3.2.2}$$

where $\langle \omega \rangle_\rho$ is the expectation value of the particle energy measured on the spectrum $\rho(\omega)$. Figure 3.1-*Bottom* shows the effective mass as a function of lattice time for the Υ meson for two types of quark sources at $T = 94$ MeV. From this form, one can see the effective mass associated with a single-exponential state such as Eq. (3.2.1) converges at M in the limit of large lattice time, in which the ground state dominates. In the small-τ regime excited states contribute toward the value of M_{eff}, while at large-τ there is a signal-to-noise problem (which we shall revisit in detail in §4). We have opted to fit the M_{eff} plateau in the intermediate-τ region to use as our value of M for comparison. Figure 3.2 shows the mass splitting for a selection of meson channels derived from single-exponential fits to our "zero-temperature" correlator ($T = 47$ MeV) compared with the experimental values obtained by the Particle Data Group (PDG) [2]. Since the intention of this work is to assess the suitability of the
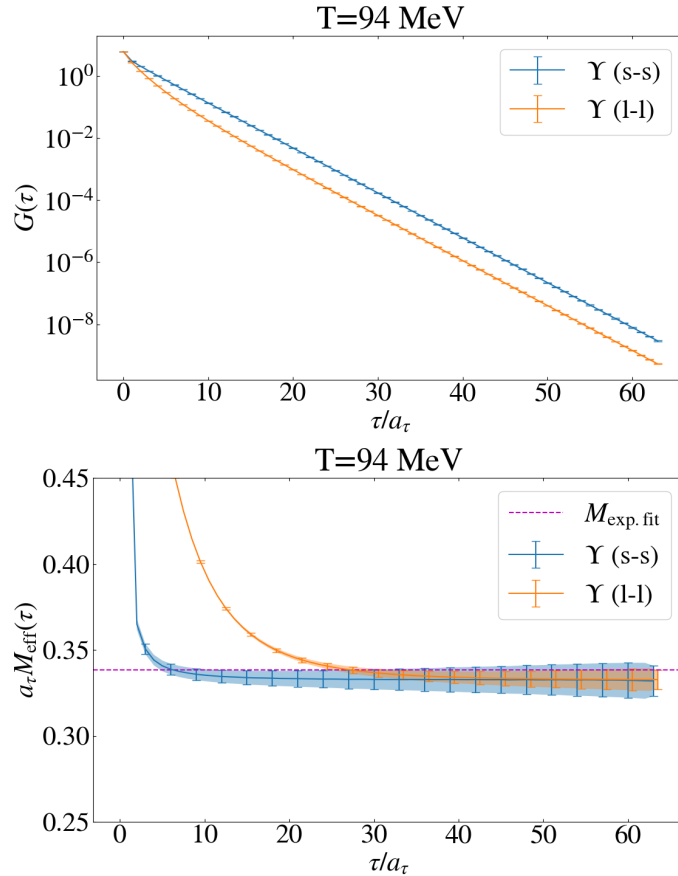
Figure 3.1:   The correlator $G(\tau)$ (*Top*) and effective mass $a_\tau M_{\text{eff}}(\tau)$ (*Bottom*) for the Υ meson versus lattice time τ/a_τ, for local (l-l) and smeared (s-s) quark sources (see §3.3) at $T = 94$ MeV ($N_\tau = 64$). The magenta line represents the estimates obtained from a single exponential fit to our "zero-temperature" ($T = 47$ MeV, $N_\tau = 128$) correlator. For the effective mass plot (*Bottom*), a small offset in the data has been introduced to aid visual comparisons between the two curves, with the transparent region denoting the error in the effective mass.

Backus-Gilbert method in ascertaining particle masses and widths, we shall instead compare our Backus-Gilbert results with the results of a single-exponential fitting procedure instead.

3.3   Local vs. smeared quark sources

The naive implementation of a fermion source $\psi(x)$ (with $x \in \{\Lambda\}$) would be the exactly localised field $\psi(x_0)$ for some lattice coordinate x_0. This is known as a *local* or *point* source. Although such a source would indeed be capable of probing the physical state encoded by some set of interpolating operators, one can augment the operator by extending the source with some smearing function to include contributions from neighbouring fermion fields, which can result in improved overlap with the desired state [32], as shown in Fig. 3.1. This general group of augmented approaches are
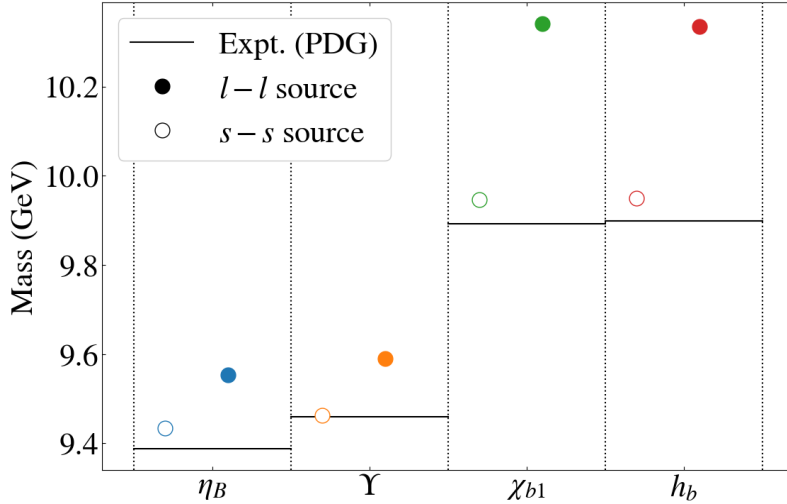
Figure 3.2: Comparison of single exponential fits to the NRQCD correlator for select channels at our lowest lattice temperature ($T = 47$ MeV) versus experimental Particle Data Group (PDG) values [2]. Closed faces denote local quark sources whilst open faces denote smeared quark sources (see §3.3). The NRQCD energy shift E_0 is set by matching $M_\Upsilon^{\mathrm{PDG}}$ with the result obtained for $M_\Upsilon^{\mathrm{latt}}$ using smeared quark sources.

known as *smeared* or *extended* sources. The FASTSUM ensembles which we shall make use of in this analysis contain both local quark source correlators and Gaussian [73] smeared source correlators, with a smearing width of 2.5 spatial lattice units [74]. In the following, we shall refer to data generated using local and smeared quark sources with the labels 'l-l' and 's-s' respectively.

3.4 DETERMINING THE GROUND STATE MASS AND WIDTH

In order to extract physical values for the ground state mass and width from the spectrum, we consider the ground state for the spectral density function to be the first *prominent* peak closest to the expected value of the mass derived from single-exponential fits. We assume that the ground state feature is given by a Gaussian distribution, which corresponds roughly to a single-state with central value μ and width σ. To compensate for the fact that $\rho(\omega)$ is not required to be strictly positive when using the least-squares criterion, we opt to only fit the upper half of the ground state peak. We further restrict the fit region to only include the leading portion of the peak, as it is often the case that the averaging functions are broad enough to incur contributions from excited states, as seen in Figs. 2.10 and 2.11.

The Laplace shifting procedure also causes oscillatory behaviour to manifest at ω early in the sampling window, which grows with increasing Δ. In order to fulfill the

'prominence' condition of the ground state, we disregard any reconstructed spectrum where the peak preceding the ground state exceeds 50% of the height of the ground state. This is a conservative restriction which we believe prevents the peak finding algorithm from incorrectly identifying a noise artefact as the ground state.

Once the peak finding algorithm has identified a candidate ground state, the central value of the Gaussian fit, μ, is reported as the ground state mass, M, and the FWHM width is given by $\Gamma = 2\sqrt{2\log 2}\sigma$.

3.5 UNSHIFTED RESULTS

We begin by briefly presenting some results obtained using the original (unshifted) interpretation of the Backus-Gilbert method, and the least-squares criterion defined in Eq. (2.5.8). Figures 3.3-3.6 show the ground state mass and width versus the temperature for the η_b and Υ mesons, using local and smeared quark sources. It is readily seen that there is a strong dependence on the whitening parameter α for both the ground state mass and the width. Also noticeable is the statistical error that grows as a function of α. The large deviation in the central values for large α suggests that the localisation and broadening artefacts described in §2.7 are inducing a systematic shift towards small M/large Γ.

Comparing Figs. 3.4 and 3.6 with Figs. 3.3 and 3.5 also highlights the effect of implementing point versus smeared quark sources. When we apply a smearing operator to the quark sources there is better overlap with the ground state as the signal from higher excited states are suppressed, which should help to reduce shifting of the spectral features when the averaging function is broader than the mass splitting between the ground and first excited states.

Overall, for the unshifted results we observe a good overlap with the expected value of the ground state mass only in the case of smeared quark sources and at the smallest values of α, with the associated estimates of the mass having a very large error. The estimates of the ground state width are very poor for local quark sources, but are improved in the case of smeared sources. The predicted width decreases with α as expected, but are still $\mathcal{O}(\text{GeV})$ in scale.
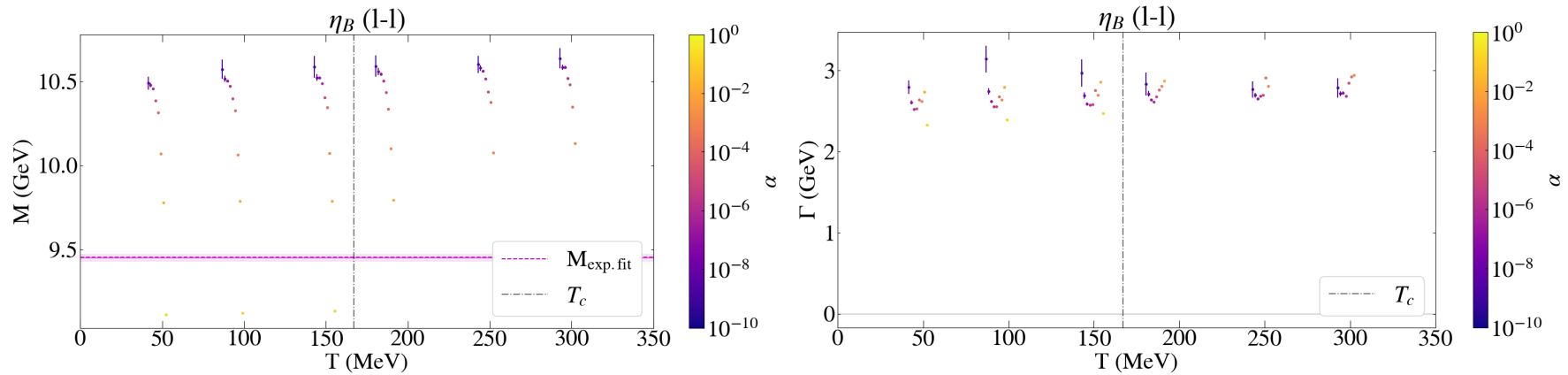
Figure 3.3: Mass (*Left*) and width (*Right*) of the η meson (l-l) versus temperature. The colour represents the value of the whitening parameter, α.
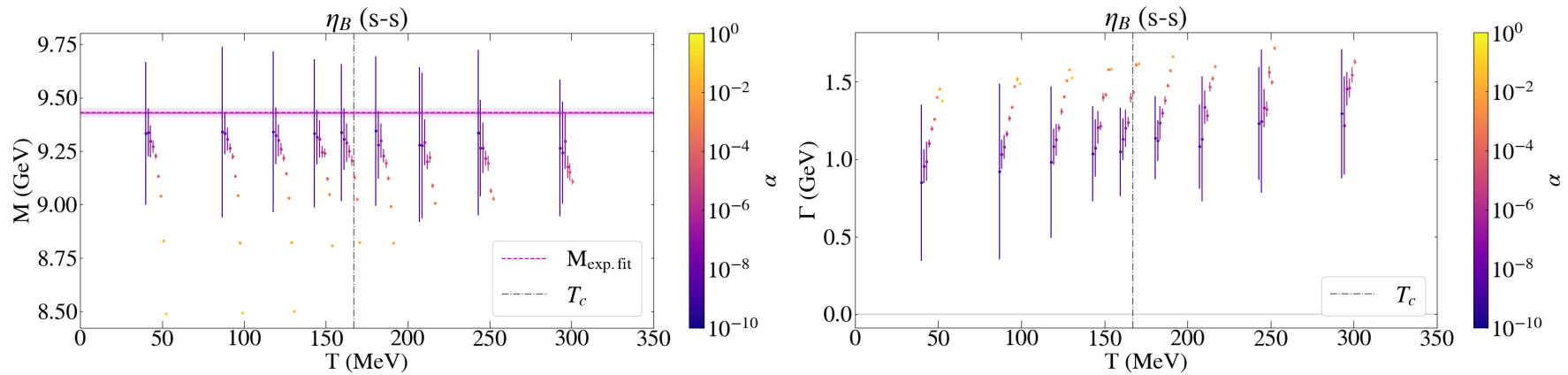
Figure 3.4: Mass (*Left*) and width (*Right*) of the η_b meson (s-s) versus temperature. The colour represents the value of the whitening parameter, α.
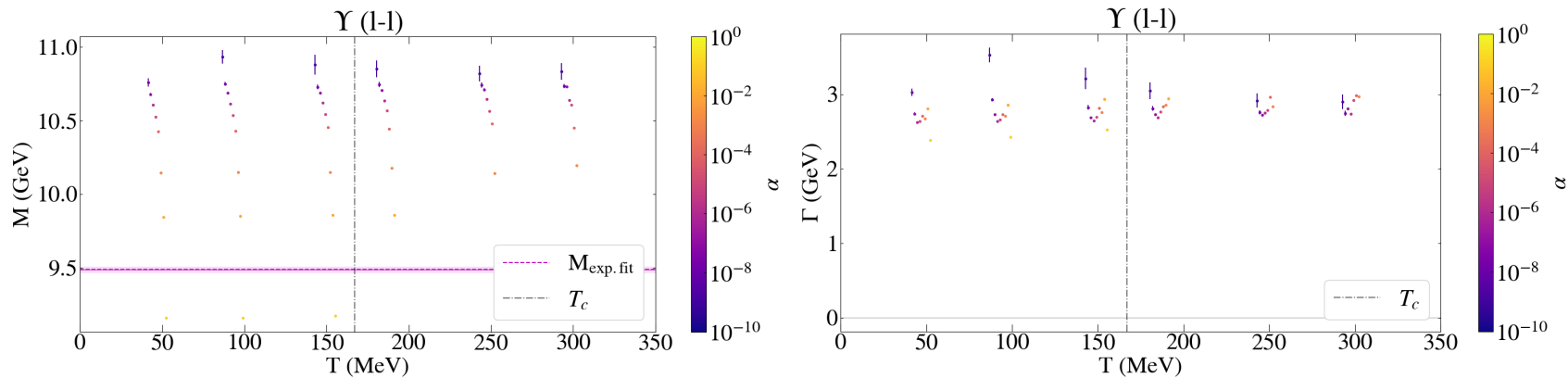
Figure 3.5: Mass (*Left*) and width (*Right*) of the Υ meson (l-l) versus temperature, The colour represents the value of the whitening parameter, α.
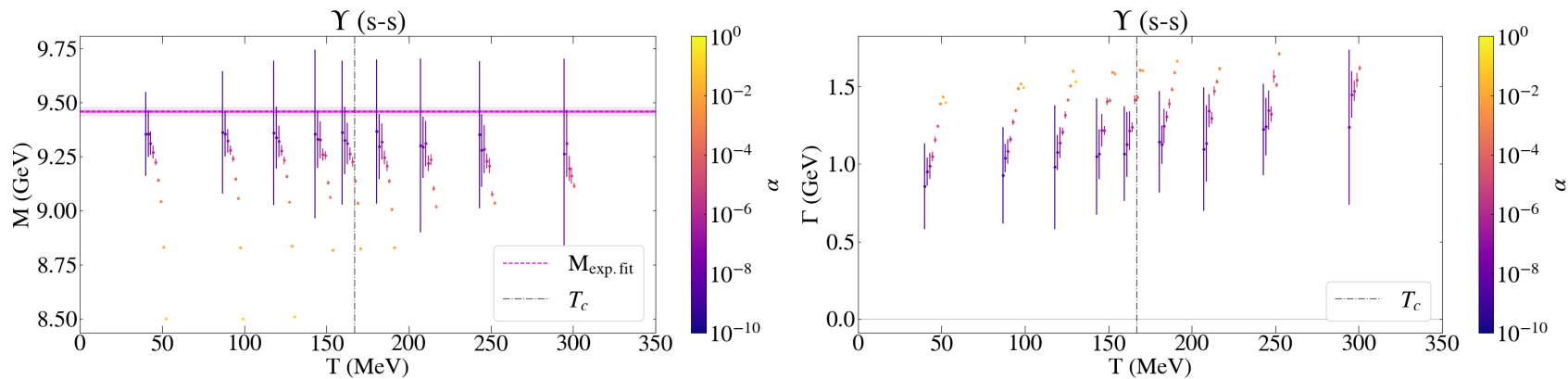
Figure 3.6: Mass (*Left*) and width (*Right*) of the Υ meson (s-s) versus temperature, The colour represents the value of the whitening parameter, α.

3.6 LAPLACE-SHIFTED RESULTS

Motivated by the poor results for the unshifted Backus-Gilbert method, we now present results for the η_b, Υ, χ_{b1}, and h_b bottomonium mesons generated using the FASTSUM ensembles, employing the Laplace shift improvement routine to the Backus-Gilbert method, as outlined in §2.8. In this approach, we must remove the dependence of the mass and width on both the whitening factor, α, and the shift parameter, $\widetilde{\Delta}$, shown in Fig. 3.7 and 3.8, which we shall attempt to do via an extrapolation routine.
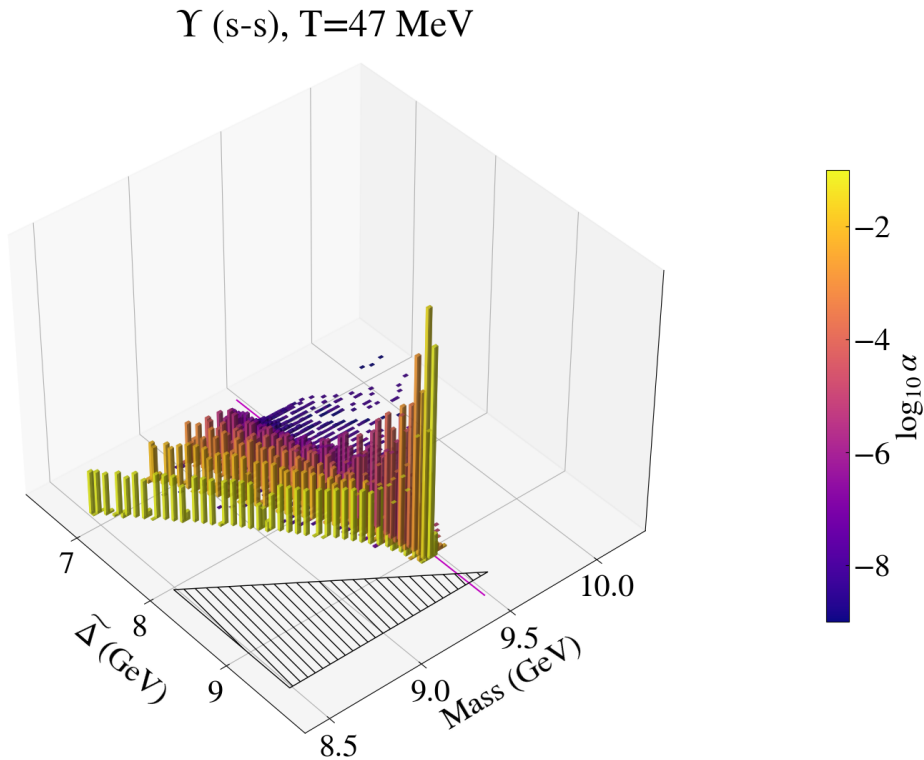
Figure 3.7: 3D histogram of the ground state mass of the Υ meson versus the Laplace shift parameter, $\widetilde{\Delta}$. The colour of the samples represents the whitening factor, α, used. The hatched region denotes the maximum possible Laplace shift $\widetilde{\Delta} = M$ and the magenta line is the estimate for the Υ mass obtained using exponential fits.

When generating mass and width data, we can easily sample many points in the parameter space of $\widetilde{\Delta}$ as the dependence is purely a multiplicative scaling of $G(\tau)$, but sampling the α dependence requires an iteration of the Backus-Gilbert method for each α (as the dependence is contained within c_τ). For our extrapolation routine, we sample approximately $\mathcal{O}(10)$ values of α and $\mathcal{O}(40)$ values of $\widetilde{\Delta}$. We opt to perform the extrapolation in $\widetilde{\Delta}$ first, before extrapolating in α, to maximise the statistics in the fits which carry onto the second extrapolation step.
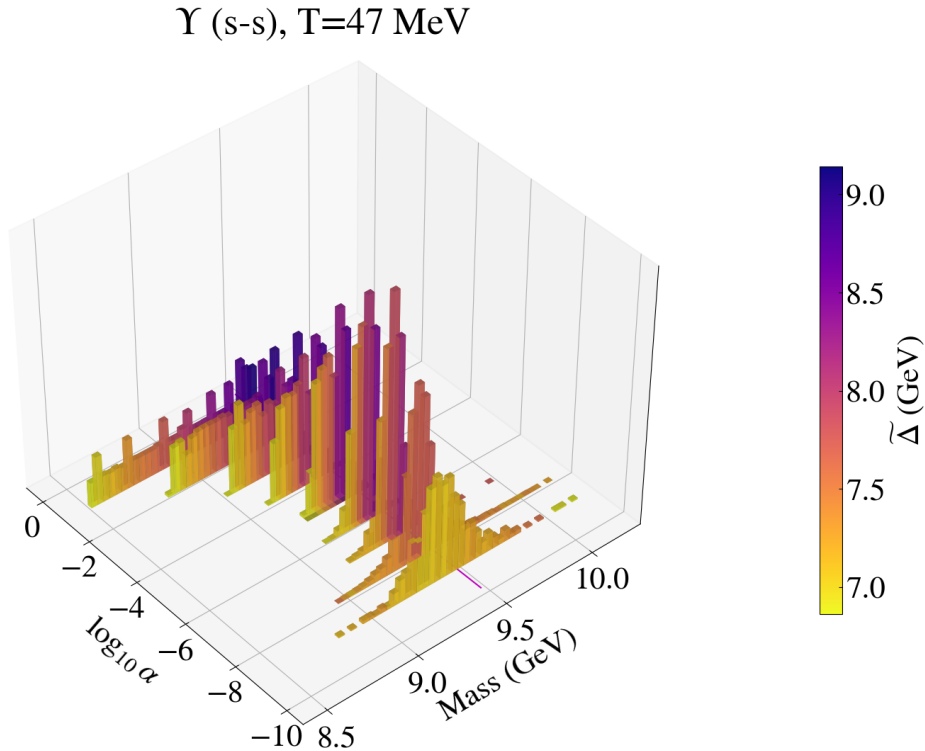
Figure 3.8: 3D histogram of the ground state mass of the Υ meson versus the whitening factor, α. The colour of the samples represents the value of $\widetilde{\Delta}$ used. The magenta line is the estimate for the Υ mass obtained using exponential fits.

Figure 3.7 shows the mass distribution of the Υ meson as a function of the Laplace shift parameter, $\widetilde{\Delta}$, in histogram form with the value of, α, represented by the color of the bar. The height of the bars represents the frequency. Figure 3.8 shows the mass distribution as a function of the whitening parameter, α, with $\widetilde{\Delta}$ represented by the color. In both plots, the magenta line is the mass of the Υ from single exponential fits.

The maximal value of the $\widetilde{\Delta}$-shift which produces a valid (but not necessarily interpretable) result is $\widetilde{\Delta} = M$, with M the ground state mass of the system. This corresponds to the hatched wedge in Fig. 3.7. When $\widetilde{\Delta} > M$, the ground state feature is 'pushed' outside of the sampling window by the shift transformation and is no longer observable.

It is evident from Figs. 3.7 and 3.8 that there is a strong systematic dependence of the mass on the value of α and $\widetilde{\Delta}$. In Fig. 3.7 we see that for fixed $\widetilde{\Delta} = E_0 \sim 7.5$ GeV (i.e., no shift with respect to E_0) there is a strong dependence of mass on the whitening parameter, α, but this dependence is not seen for $\widetilde{\Delta} \sim 9$ GeV. Similarly, we see in Fig. 3.8 that for fixed $\log_{10} \alpha \sim 1$ the mass is strongly dependent on $\widetilde{\Delta}$,
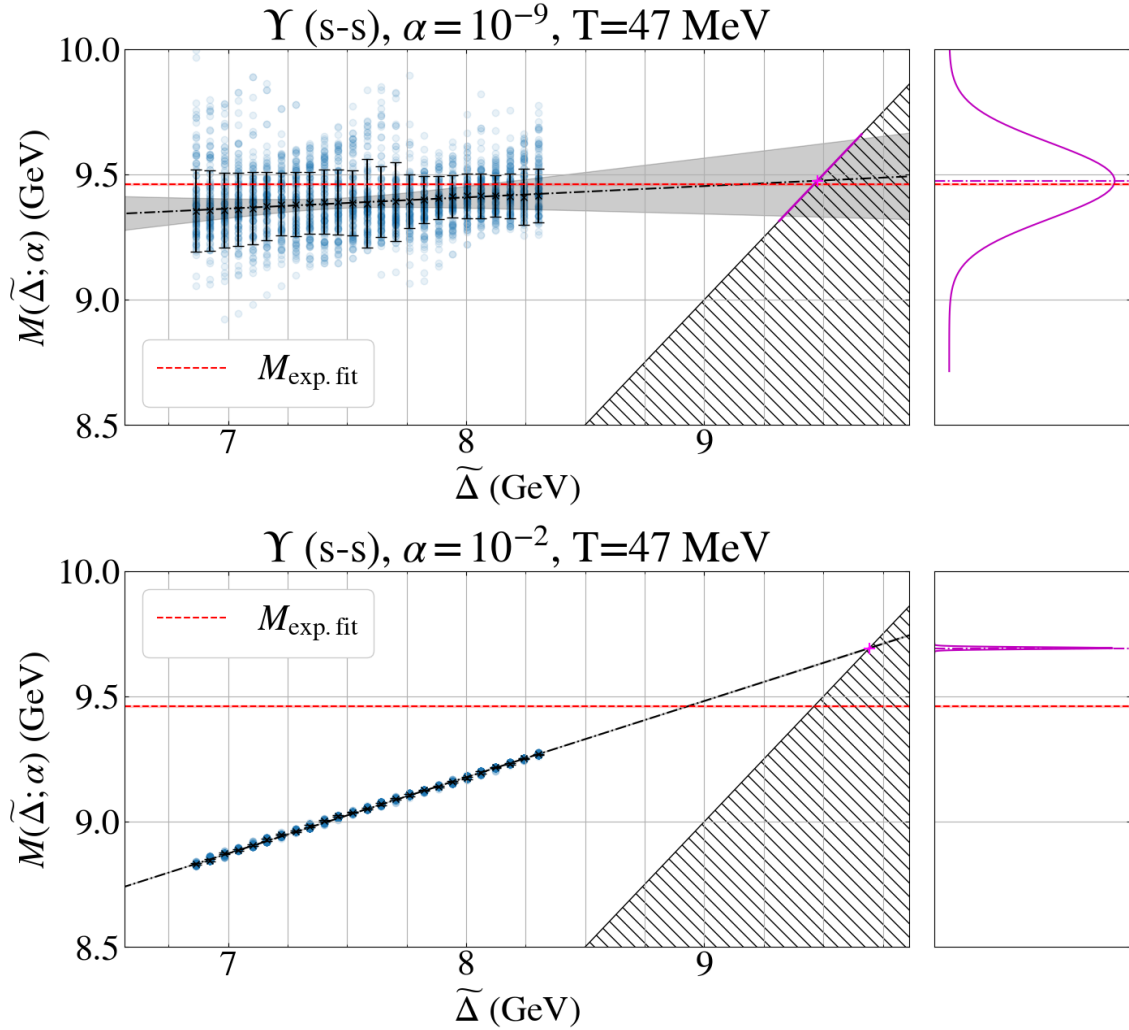
Figure 3.9: Example of plot showing the bootstrap predictions for the ground state mass as a function of the adjusted Laplace shift, $\widetilde{\Delta}$, for $\alpha = 10^{-9}$ (*Top*) and $\alpha = 10^{-2}$ (*Bottom*). The hatched region is the maximum allowed shift $\widetilde{\Delta} = M$. The magenta cross represents $M(\alpha)$. The right hand side of the figure shows the distribution of the central fit along the face of the wedge compared with the expected value in red, with the magenta line corresponding to $M(\alpha)$.

but that the relative uniformity in the colour of the distribution at $\log_{10} \alpha \sim -9$ suggests that this dependence has fallen away.

Both Figs. 3.9 and 3.10 show a normal distribution in M which arises in the limit $\alpha \to 0$ and $\widetilde{\Delta} \to M$ (represented by the boundary of the hatched region), suggesting that these limits provide a natural extrapolation point for our routine.

Figure 3.9 shows the mass as a function of $\widetilde{\Delta}$ for $\alpha = 10^{-9}$ and $\alpha = 10^{-2}$, and for $T = 47$ MeV. Fitting $M(\widetilde{\Delta}; \alpha)$ with the linear ansatz

$$M(\widetilde{\Delta}; \alpha) = A(\alpha)\widetilde{\Delta} + B(\alpha) \tag{3.6.1}$$
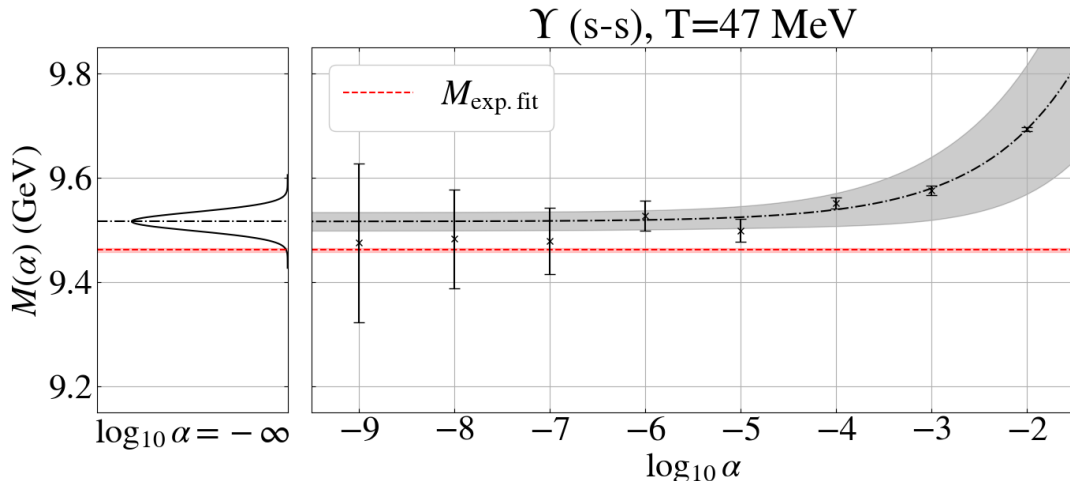
Figure 3.10: Plot showing the values of the wedge crossings as a function of α. The distribution in the leftmost pane is the $\alpha \to 0$ (represented in log-space by $\log_{10} \alpha = -\infty$) extrapolated values for the central fit, with the dot-dashed black line representing the central value. The red dashed line is the single-exponential fit estimate of the mass.

and extrapolating to the intersection of the line $\widetilde{\Delta} = M$ (represented by the magenta cross on the hatched region of Fig. 3.9) yields the mass as a pure function of the whitening parameter

$$M(\alpha) = \frac{B(\alpha)}{1 - A(\alpha)}. \tag{3.6.2}$$

The linear ansatz is motivated by the apparent linear dependence of M with $\widetilde{\Delta}$ (Fig. 3.9-*Bottom*) and of the position of the averaging functions on the position in the sampling window, as shown in Fig. 2.6. This explicitly highlights the issue with Backus-Gilbert caused by the averaging functions being improperly located (as shown by Fig. 2.3). When the centre of $A(\omega, \omega_0)$ differs from ω_0, we measure smaller values for the mass and our resulting linear extrapolation is tilted upwards (see Fig. 3.9-*Bottom*), producing an over-estimate for $M(\alpha)$.

This fitting process can be repeated for each value of α, which is shown in Fig. 3.10. In a similar manner to the $\widetilde{\Delta}$ extrapolation, we may now remove the α dependence using a fit function of the form

$$M(\alpha) = C e^{D \log_{10} \alpha} + M_{\alpha=0}, \qquad (D > 0), \tag{3.6.3}$$

where $M_{\alpha=0}$ represents our extrapolated value of the mass. This functional form is motivated by the fact that the whitening parameter, α, is sampled at each order of magnitude, and that we anticipate the dependence of the mass on α to fall away

yielding the 'true' mass in the limit where $\alpha \to 0$. Simplifying the exponential in Eq. (3.6.3) reduces the function to to the power-law form

$$M(\alpha) = C\alpha^{\widetilde{D}} + M_{\alpha=0}, \qquad (\widetilde{D} > 0), \qquad (3.6.4)$$

with $\widetilde{D} = D/\ln(10)$. Both functional forms were tested with the fitting routine, with Eq. (3.6.3) converging more consistently than Eq. (3.6.4), despite their mathematical equivalence.

To test the stability of the extrapolation routine, we also explicitly test the case where $C = 0$ in Eq. (3.6.3) (corresponding to a constant fit). In all cases, we measure the reduced χ^2 value as a goodness-of-fit statistic, which is shown in Figs. 3.23 and 3.24.

We perform a similar routine for the determination of the ground state width Γ, shown in Figs. 3.11 and 3.12 for the Υ meson (s-s) at $T = 47$ MeV. We loosen the restriction that $\Gamma(\widetilde{\Delta}; \alpha)$ be linear in $\widetilde{\Delta}$ and also test exponential ansätze of the form

$$\Gamma(\widetilde{\Delta}; \alpha) = A(\alpha)e^{-B(\alpha)\widetilde{\Delta}} + C(\alpha), \qquad (3.6.5)$$

as we anticipate the width to be finite and constant when the width of the averaging functions becomes narrower than the true width of the underlying state.
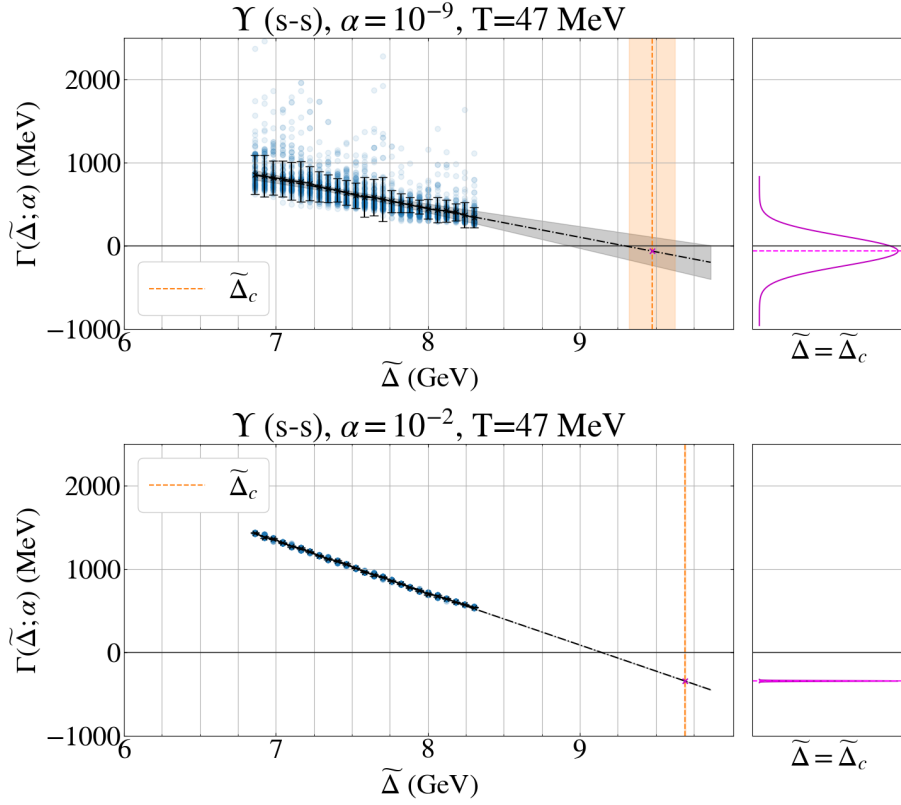
Figure 3.11: Example of plot showing the bootstrap predictions for the ground state width, Γ, as a function of the Laplace shift, $\widetilde{\Delta}$, for $\alpha = 10^{-9}$ (*Top*) and $\alpha = 10^{-2}$ (*Bottom*). The vertical dashed line represents $\widetilde{\Delta}_c(\alpha)$, the point of intersection between $M(\widetilde{\Delta}; \alpha)$ and the hatched region of Fig. 3.9 (i.e. $\widetilde{\Delta}_c(\alpha) = M(\alpha)$) The right hand side of the figure shows the distribution of the central fit about $\Gamma(\widetilde{\Delta}_c; \alpha)$, denoted by the magenta line.
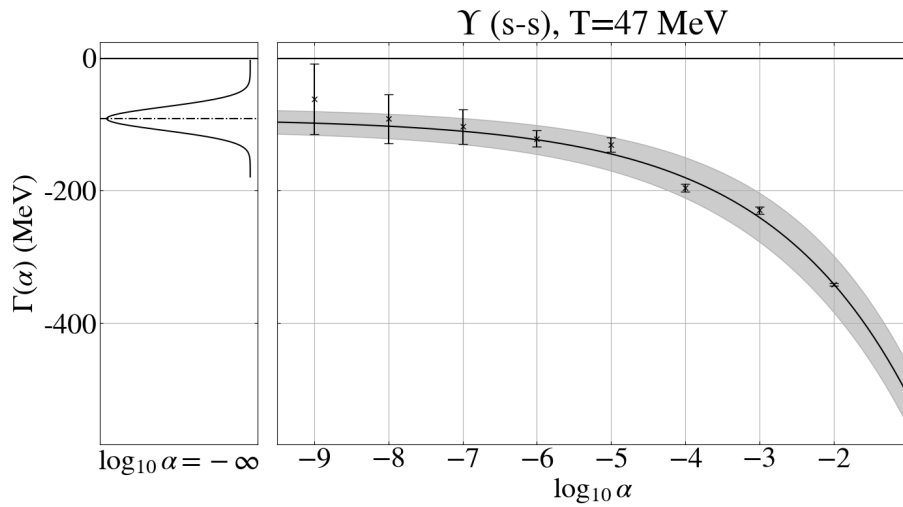
Figure 3.12: Plot showing the values of the width, Γ, evaluated at the wedge crossings $\widetilde{\Delta} = \widetilde{\Delta}_c$ as a function of α. The distribution in the leftmost pane represents the $\alpha \rightarrow 0$ extrapolated values for the central fit to the width, with the dot-dashed black line representing the central value.
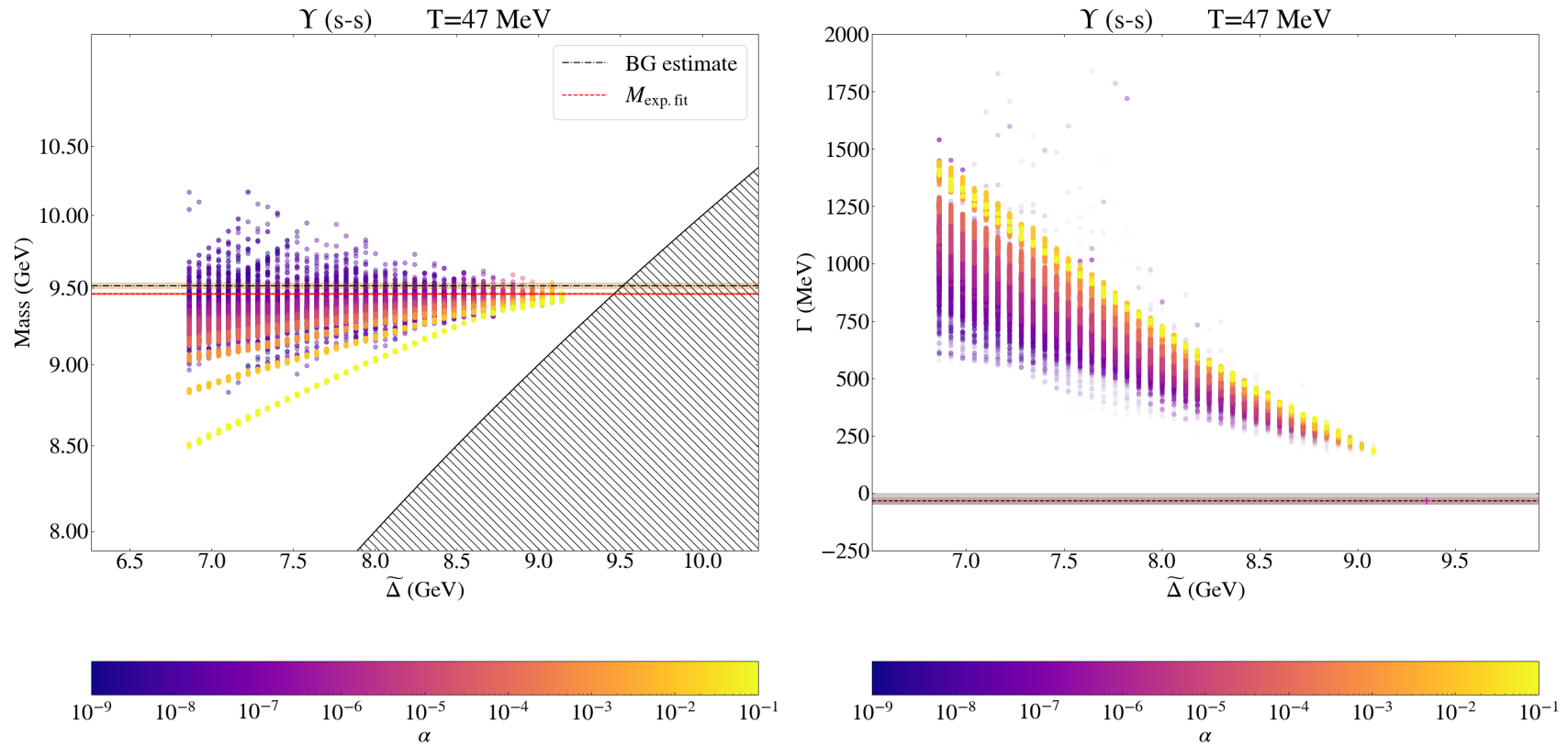
Figure 3.13: *Left*: Scatter plot of the bootstrap estimates for the ground state mass of the Υ meson (s-s) versus the Laplace shift parameter, $\widetilde{\Delta}$. Overlaid is the prediction from the extrapolation routine (black) and the prediction from the single-exponential fits (red). The colour of the samples represents the whitening factor, α, used. *Right*: Corresponding plot for the ground state width with the prediction from the extrapolation routine represented by the magenta cross.
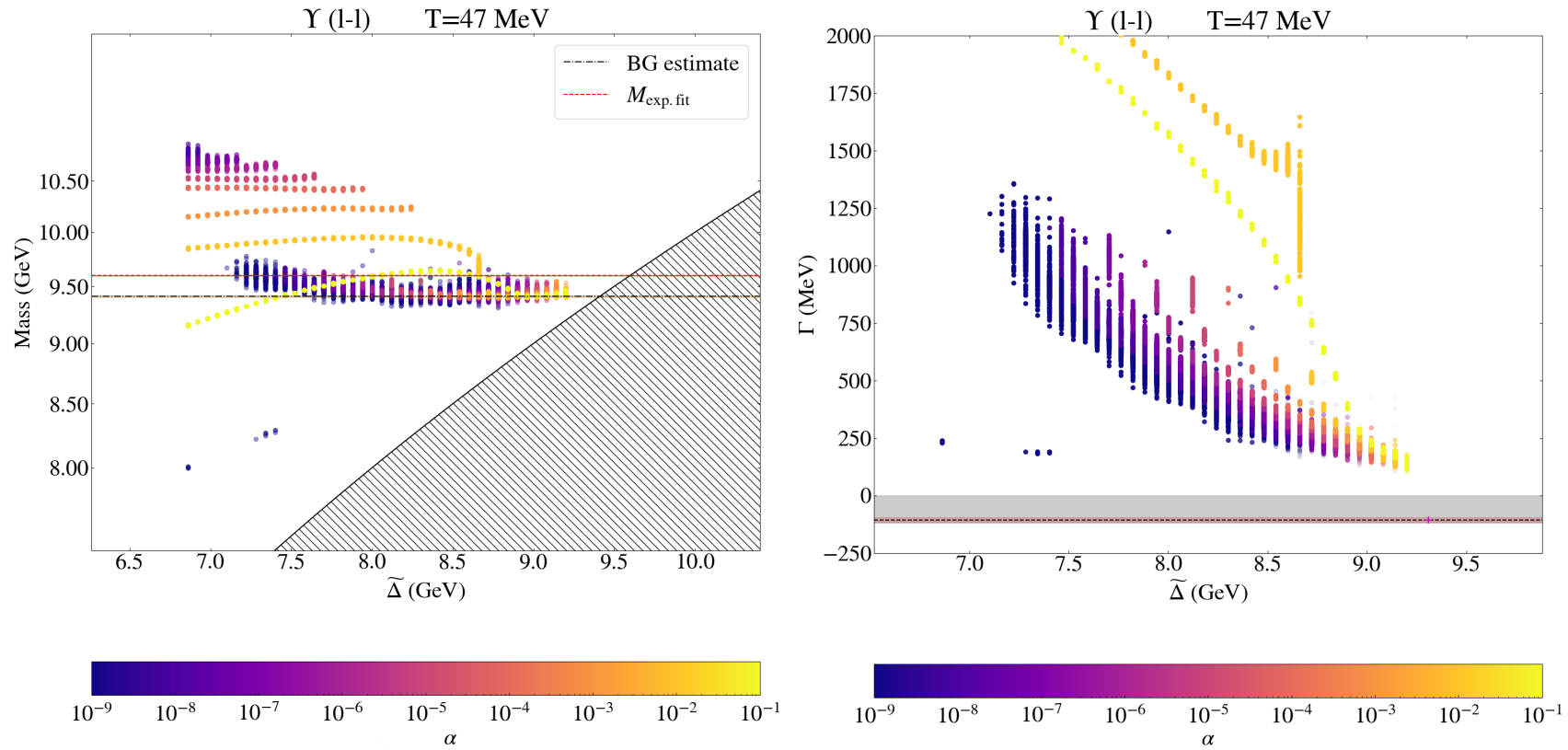
Figure 3.14: *Left*: Scatter plot of the bootstrap estimates for the ground state mass of the Υ meson (l-l) versus the Laplace shift parameter, $\widetilde{\Delta}$. Overlaid is the prediction from the extrapolation routine (black) and the prediction from the single-exponential fits (red). The colour of the samples represents the whitening factor, α, used. *Right*: Corresponding plot for the ground state width with the prediction from the extrapolation routine represented by the magenta cross.

Figures 3.13 and 3.14 show the distribution of the bootstrap estimates for the ground state mass and width with the corresponding extrapolated results overlaid for the Υ meson using smeared and local quark sources respectively at $T = 47$ MeV. Also overlaid is our estimate of the mass using single exponential fits. In the case of smeared quark sources, there is a linear convergence towards the expected value of the mass and zero-width as both $\alpha \to 0$ and $\Delta \to M$, demonstrating the resolution improvement gained from the Laplace shifting procedure. However, we can see that the estimates obtained from local quark sources (Fig. 3.14 as an example) exhibit a non-trivial relation with the shift parameter and thus is not described by the models given by Eq. (3.6.1) and Eqs. (3.6.3) and (3.6.4). Extrapolations using these models yielded χ^2_ν goodness-of-fit values of $10^2 - 10^8$ (see Appendix B.1), which shows a complete failure of the routine in the case of local quark sources. As such, we will focus on the smeared quark source data (which has already been shown to exhibit better affinity with the ground state in Fig. 3.1-*Bottom*) and leave adjustments necessary to support extrapolations using local quark source data to future work.

Comparing Figs. 3.13 and 3.14 with the unshifted results presented in §3.5, one can see not only a vast improvement on the measured values for the mass and width, but also smaller calculated values for the uncertainty (which we wish to highlight is a mixture of statistical and systematic in origin). Another added benefit of using the Laplace shift procedure is that the resolution limit is much lower than in the unshifted approach, as the shift moves the ground state peak to a region with narrower averaging functions. This means that the results for the width, Γ, can be smaller when a shift is introduced. As such, one should ideally expect to see a finite result for Γ emerging from the shift procedure only if the width of the underlying state is resolvable in at least the narrowest of the averaging functions. If the measured value of Γ is instead consistent with zero, then the method cannot resolve the underlying state and Γ only represents an upper bound on the state width.

Figures 3.15-3.20 show the different predictions in box-and-whisker form for the ground state mass and width provided by the extrapolation routine for a series of lattice temperature. For a given temperature, each data point associated with the box-and-whisker is generated by re-running the extrapolation routine with a coarser step in $\widetilde{\Delta}$ and α, and also testing the case where we set $D = 0$ to the the fit described

in Eq. (3.6.3) (i.e. the exponential fit is replaced with a linear one). The magenta bands in the mass plots corresponds to our best estimate from single-exponential fitting, with the darkest band corresponding to 1-σ errors and the lightest band representing an error of 5% in lattice units (with the 5% not including the NRQCD energy shift E_0).

The body of the box represents the interquartile range associated with the set of predictions (the central 50% of observations, assuming a normal distribution) with the dashed green and block red lines corresponding to the ensemble mean and median, respectively. The ensemble median is a better estimate of the ground state mass and width, as the number of observations is small and the distribution of estimates are asymmetrical, as highlighted by the noticeable difference in the mean and median results. This asymmetry can be seen in the taper of the box plot, which represents the 95% confidence interval associated with the median. When the taper is short, the confidence in the median is better, while a longer taper signals poorer confidence. In cases where the taper is sufficiently long as to 'fold' back on itself (e.g. the $T \sim 300$ MeV results in Figs. 3.15), this usually signals that there is insufficient data to correctly construct the box plot or there is a large underlying variance, as the confidence interval of the median exceeds the interquartile range (IQR) of the data. Finally, any points beyond the whiskers of the plot are deemed outliers and highlighted in black, with the whiskers positioned $1.5 \times$ IQR above and below the box.

Across the three meson channels tested we see that there is relatively good agreement between the ground state mass as measured using the extrapolation routine and the estimate from single exponential fits. Almost all temperatures yield mass estimates which lie within 5% of the expected mass, with no discernible dependence of the mass on the temperature. Estimates of the ground state width given by the extrapolation routine appear to increase with increasing temperature and are roughly consistent with zero-width at the lowest temperatures.

For smeared source results, the values for ground state width are far better for in comparison with the $\mathcal{O}(\text{GeV})$ widths predicted by the unshifted Backus-Gilbert method. This can be seen in full in Table 3.2, which gives the predicted ground state mass and width for each of the channels.

Our prediction of a temperature-insensitive mass is partially supported by the

literature, where previous studies are found to be in contention. It was reported in [75] and [76] that reconstructions using the MEM showed that there was no temperature dependence of the ground state mass of the Υ, whilst the χ_{b1} exhibited some thermal sensitivity. Subsequent work [37] found that there was thermal modification of the bottomonia correlators for both temperatures and it was reported that a general broadening of the peak associated with the ground state was observed above T_c, consistent with the melting of the state. Another study using the MEM [77] predicted that the Υ and η_b both survive up until $2T_c$ (beyond the temperatures probed in this work) whilst the χ_{b1} exhibited melting between $1-2T_c$. This appears to be supported by our findings, where we observe a greater ground state width for the χ_{b1} than the Υ and η_b at high temperature. We remark that there appear to be little to no bottomonia studies probing the h_b state, and so we make no further comment in this regard.

A more recent study [78] using high-statistics Bayesian approaches suggest that the apparent discrepancies in temperature dependence between published results is a facet of the reconstruction methods used. It is a well-known fact that each reconstruction method leaves a 'fingerprint' within the systematic error of the analysis and the authors of the paper state that closer attention must be paid to the analysis of these uncertainties before commenting on the temperature effects of the spectra.

We conclude by highlighting Figures 3.23 and 3.24, which show the value of the reduced chi-square statistic scattered against the ground state mass for each of the channels, at each temperature tested. For each channel, the biggest estimates for the mass appear to coincide with the poorest fits (i.e. $\chi_\nu^2 \gg 1$) and lowest temperatures, while those which exhibit overfitting ($\chi_\nu^2 \ll 1$) tend to still lie close to the expected value. This appears counter-intuitive at first, as the reconstructions at the lowest temperatures can access the highest number of basis functions, but this is often at the expense of noise arising in the mass extrapolations at small α. It is evident from this analysis of the χ_ν^2 values that there is room for improvement for our fitting and extrapolation routine – a simple cut in the data, i.e. restricting fits to some maximal χ_ν^2 value would reduce the systematic positive shift in the mass, reinforcing the suggestions of the authors of Ref. [78] that further care must be taken to correctly characterise any and all systematic effects.
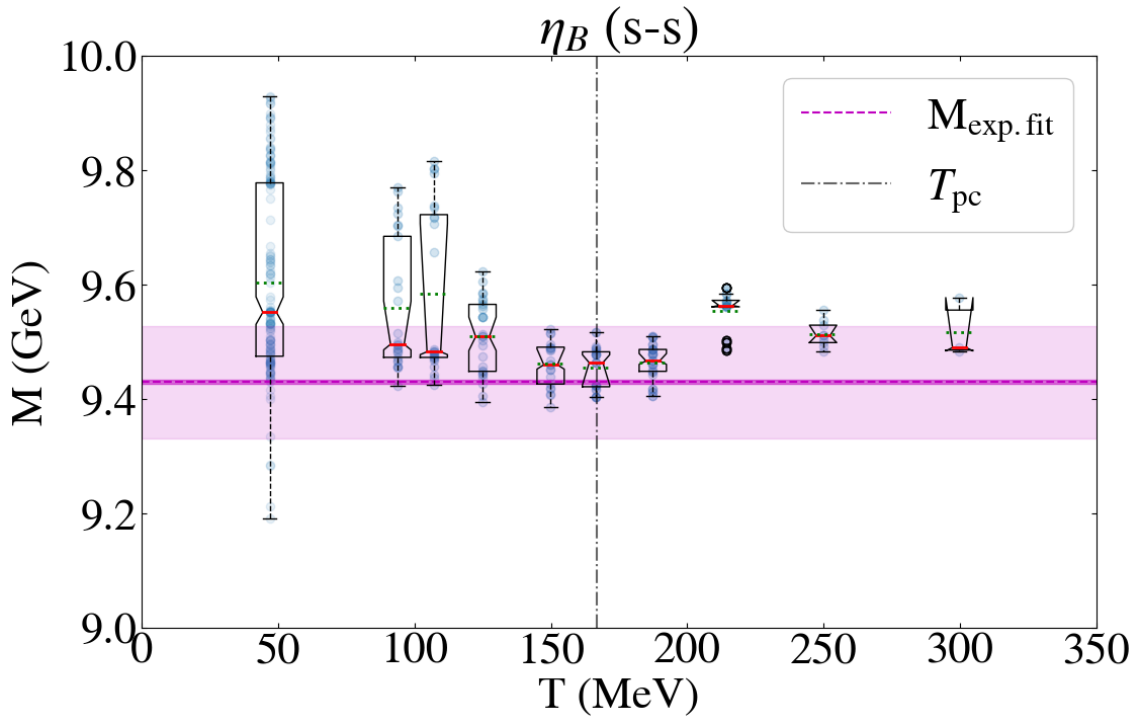
Figure 3.15: Box-plot of the ground state mass, M, versus temperature, T, for the η_b meson (s-s). The solid red and dashed green lines represent the ensemble median and mean respectively, with the body of the box representing the confidence interval and the whiskers denoting the inliers. The outliers are denoted by thick black circles (see text for detail). The magenta line represents the expected mass from exponential fits to the correlator.
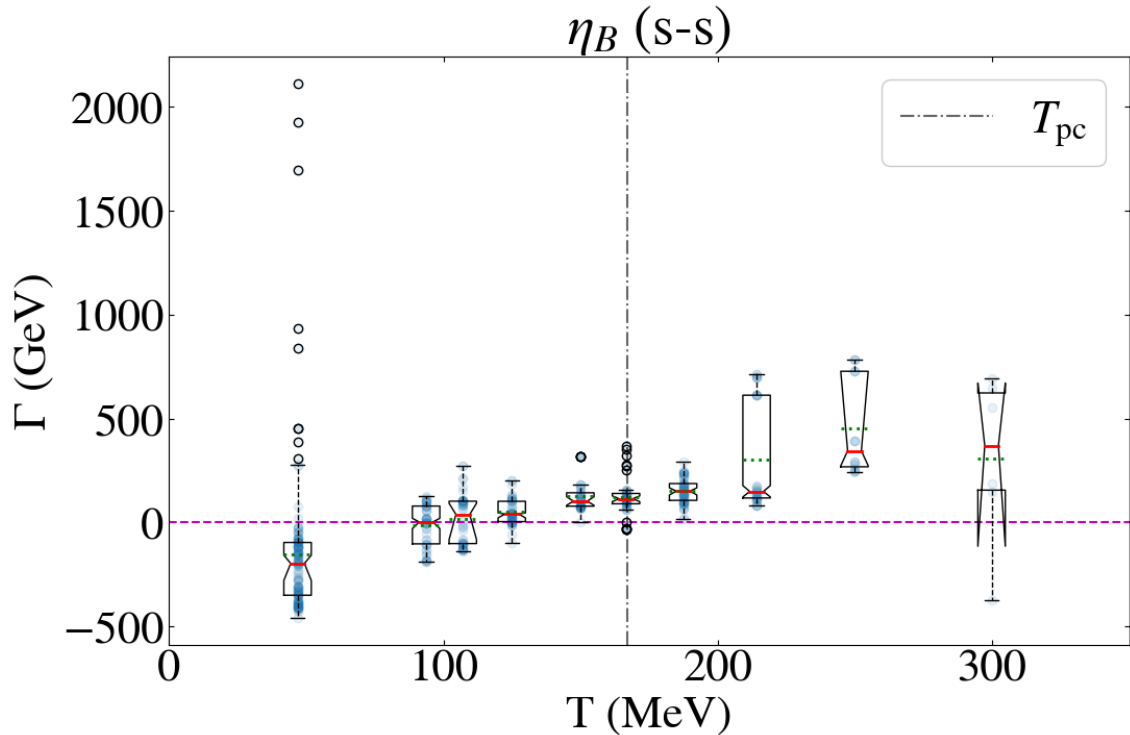
Figure 3.16: Box-plot of the ground state width, Γ, versus temperature, T, for the η_b meson (s-s). The solid red and dashed green lines represent the ensemble median and mean respectively, with the body of the box representing the confidence interval and the whiskers denoting the inliers. The outliers are denoted by thick black circles (see text for detail).
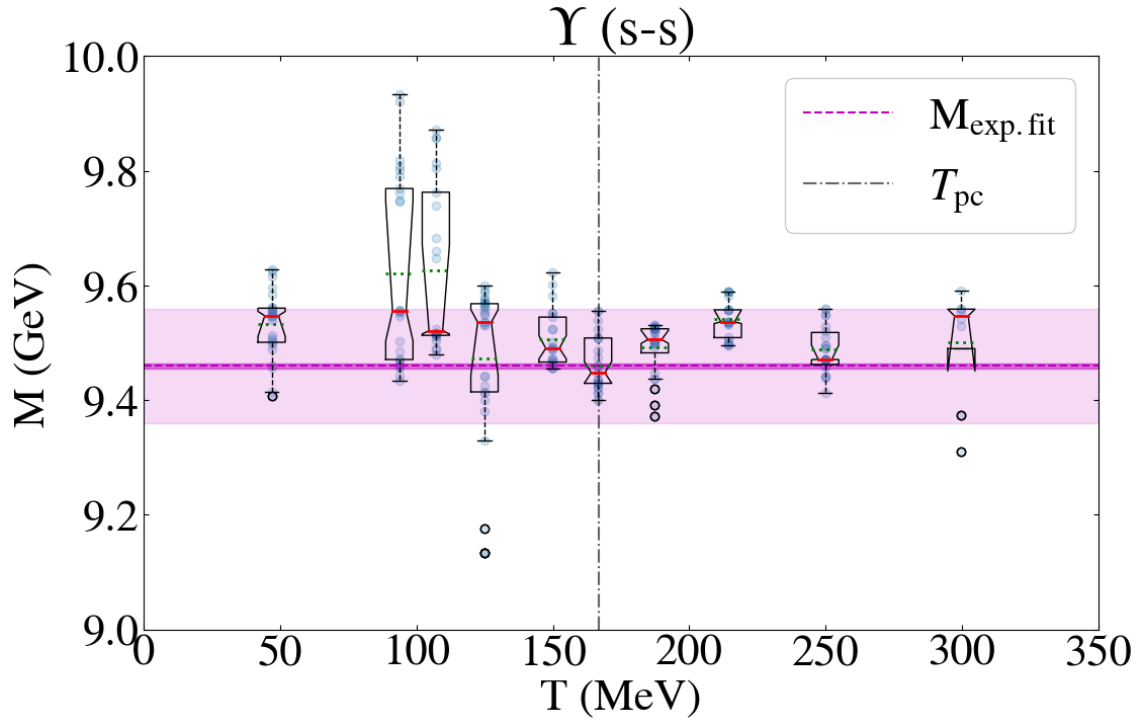
Figure 3.17: Box-plot of the ground state mass, M, versus temperature, T, for the Υ meson (s-s). The solid red and dashed green lines represent the ensemble median and mean respectively, with the body of the box representing the confidence interval and the whiskers denoting the inliers. The outliers are denoted by thick black circles (see text for detail). The magenta line represents the expected mass from exponential fits to the correlator.
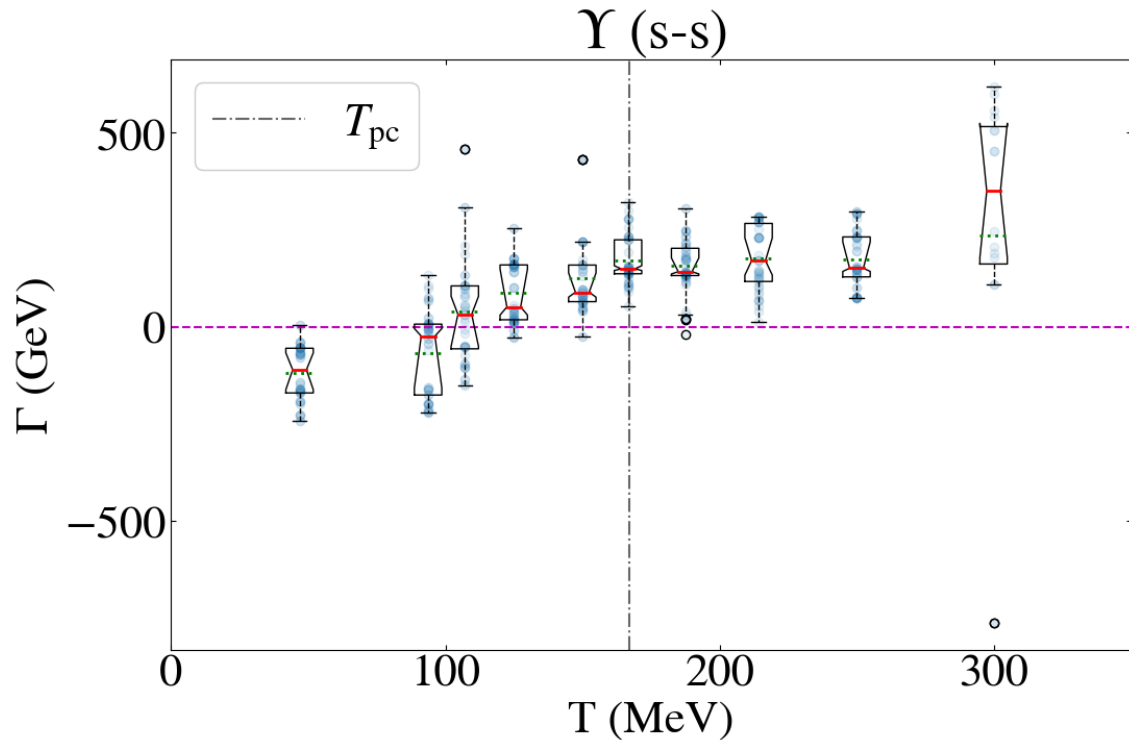
Figure 3.18: Box-plot of the ground state width, Γ, versus temperature, T, for the Υ meson (s-s). The solid red and dashed green lines represent the ensemble median and mean respectively, with the body of the box representing the confidence interval and the whiskers denoting the inliers. The outliers are denoted by thick black circles (see text for detail)
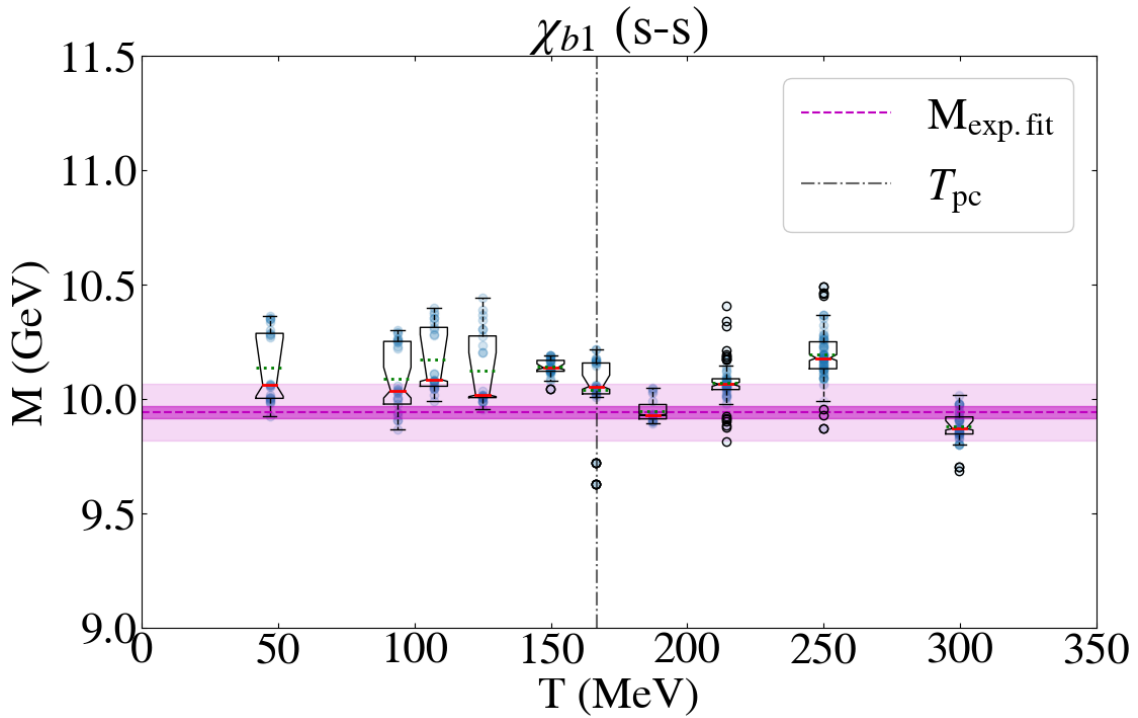
Figure 3.19: Box-plot of the ground state mass, M, versus temperature, T, for the χ_{b1} meson (s-s). The solid red and dashed green lines represent the ensemble median and mean respectively, with the body of the box representing the confidence interval and the whiskers denoting the inliers. The outliers are denoted by thick black circles (see text for detail). The magenta line represents the expected mass from exponential fits to the correlator.
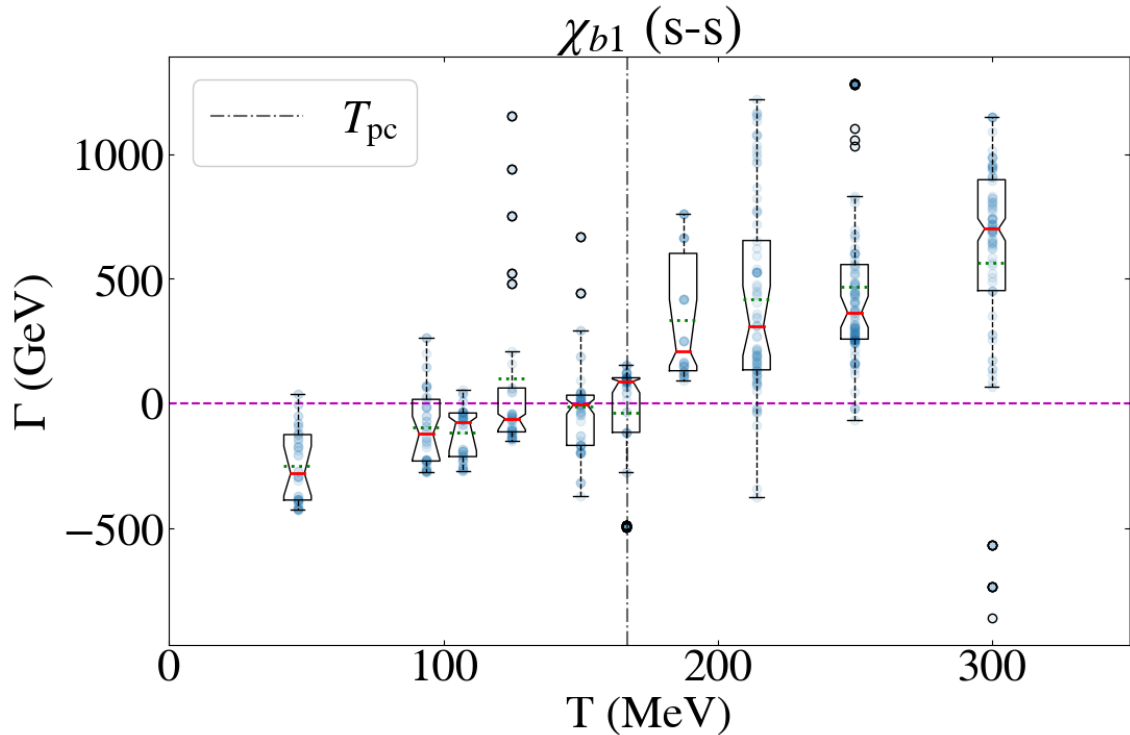
Figure 3.20: Box-plot of the ground state width, Γ, versus temperature, T, for the χ_{b1} meson (s-s). The solid red and dashed green lines represent the ensemble median and mean respectively, with the body of the box representing the confidence interval and the whiskers denoting the inliers. The outliers are denoted by thick black circles (see text for detail).
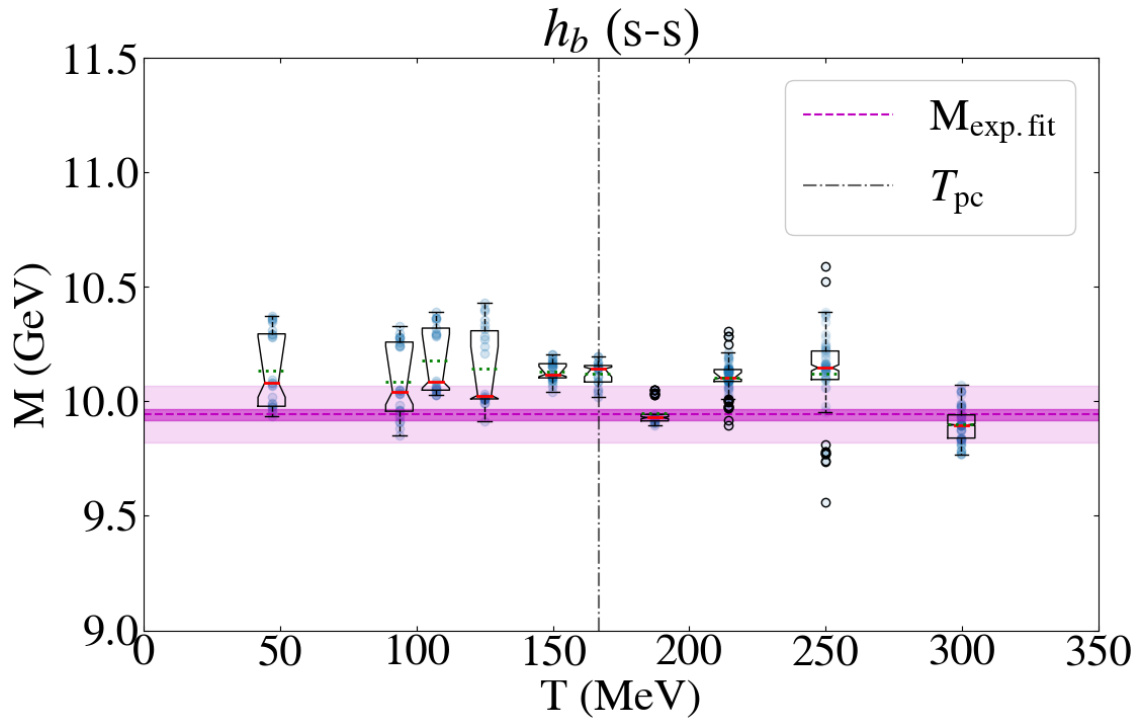
Figure 3.21: Box-plot of the ground state mass, M, versus temperature, T, for the h_b meson (s-s). The solid red and dashed green lines represent the ensemble median and mean respectively, with the body of the box representing the confidence interval and the whiskers denoting the inliers (see text for detail). The magenta line represents the expected mass from exponential fits to the correlator.
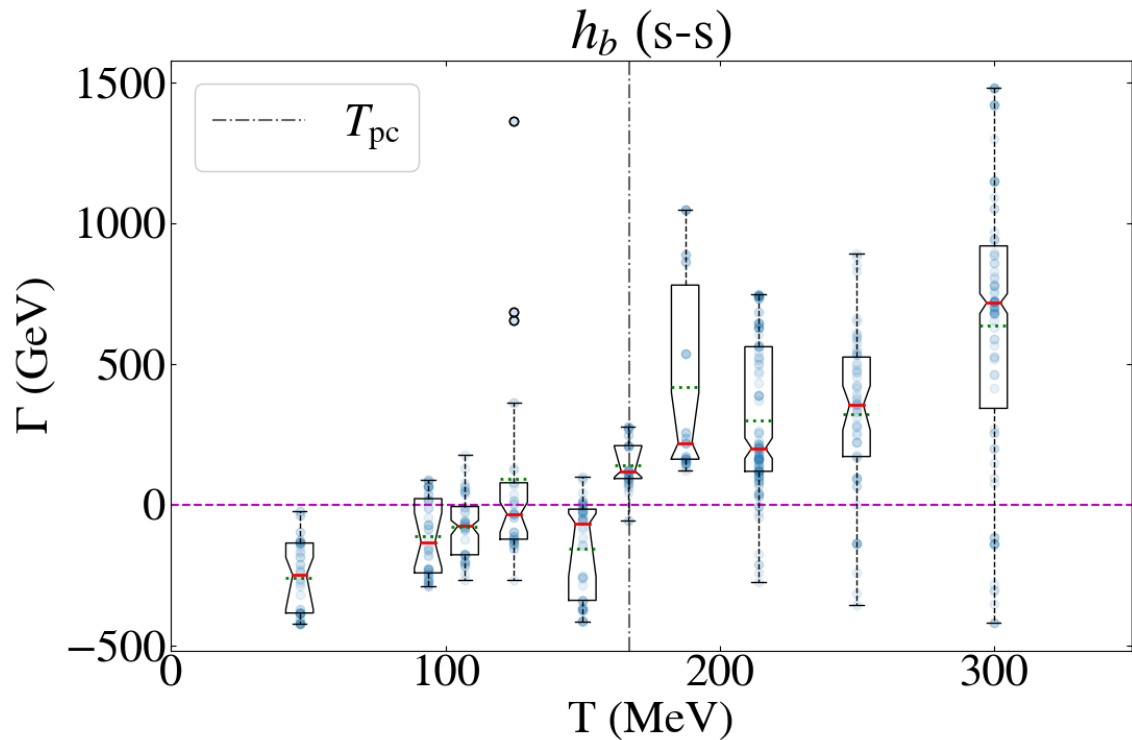
Figure 3.22: Box-plot of the ground state width, Γ, versus temperature, T, for the h_b meson (s-s). The solid red and dashed green lines represent the ensemble median and mean respectively, with the body of the box representing the confidence interval and the whiskers denoting the inliers. The outliers are denoted by thick black circles (see text for detail).
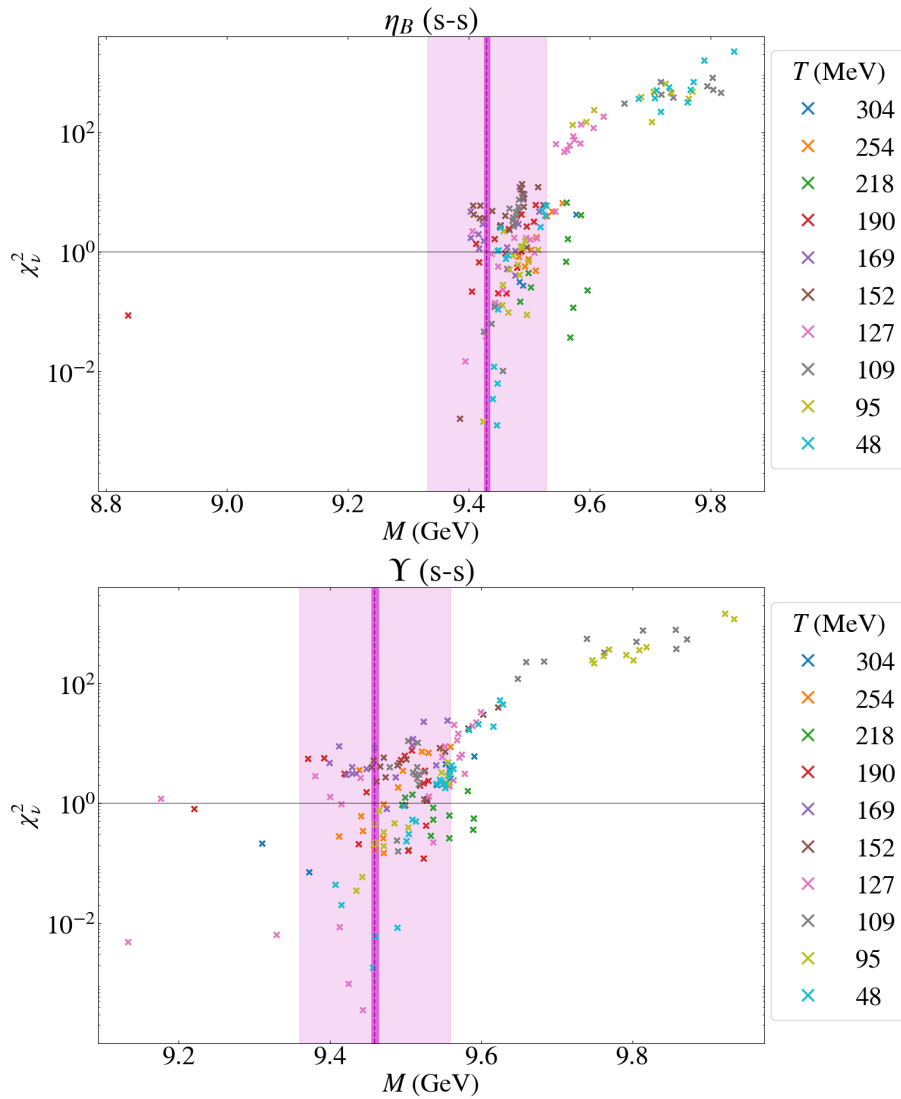
Figure 3.23: Plot of χ_ν^2 vs M for the η_b (s-s) (*Top*) and Υ (s-s) (*Bottom*) mesons, for a range of temperatures, with the vertical magenta bands corresponding to the 1σ (dark) and 5% (light) bounds on the mass estimated using exponential fits.
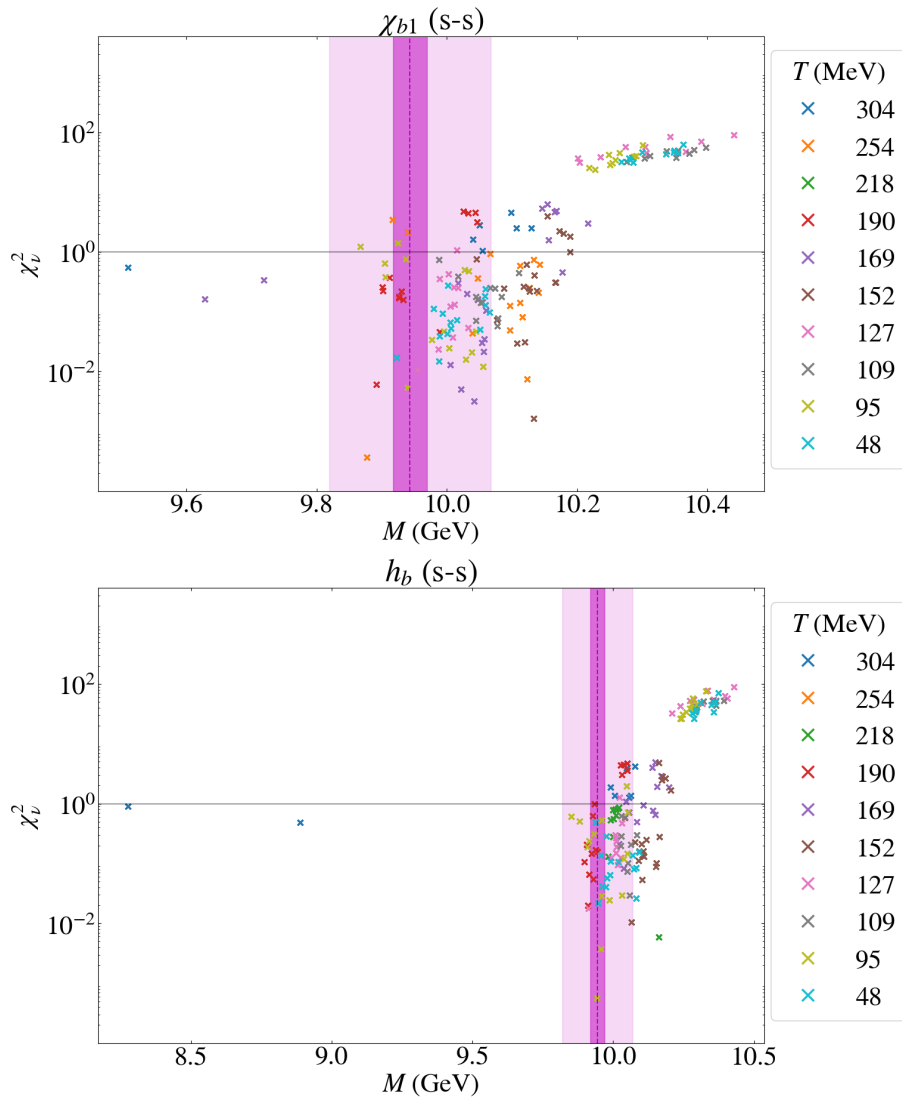
Figure 3.24: Plot of χ_ν^2 vs M for the χ_{b1} (s-s) (*Top*) and h_b (s-s) (*Bottom*) mesons, for a range of temperatures, with the vertical magenta bands corresponding to the 1σ (dark) and 5% (light) bounds on the mass estimated using exponential fits.

Table 3.2: Table of results for the ground state mass M and FWHM width Γ for each of the tested meson channels using smeared quark sources, generated in the time window $\tau \in [1, N_\tau)$.

N_τ T	20	24	28	32	36	40	48	56	64	128
					η_b (s-s)					
M (GeV)	9.489^{+05}_{-87}	9.510^{+12}_{-18}	9.5632^{+25}_{-89}	9.466^{+18}_{-02}	9.463^{+42}_{-19}	9.459^{+34}_{-31}	9.508^{+61}_{-57}	9.48^{+01}_{-24}	9.49^{+02}_{-19}	9.52^{+08}_{-19}
Γ (MeV)	369^{+480}_{-300}	344^{+76}_{-380}	149^{+31}_{-463}	151^{+44}_{-36}	114^{+24}_{-25}	102^{+23}_{-40}	40^{+36}_{-61}	38^{+140}_{-64}	2^{+105}_{-76}	-161^{+98}_{-121}
					Υ (s-s)					
M (GeV)	9.547^{+57}_{-12}	9.470^{+09}_{-47}	9.536^{+28}_{-21}	9.505^{+23}_{-19}	9.447^{+19}_{-60}	9.490^{+24}_{-54}	9.53^{+12}_{-03}	9.52^{+24}_{-01}	9.55^{+09}_{-21}	9.546^{+46}_{-13}
Γ (MeV)	340^{+180}_{-160}	151^{+22}_{-80}	170^{+53}_{-96}	142^{+10}_{-60}	149^{+12}_{-74}	89^{+24}_{-70}	51^{+32}_{-108}	32^{+88}_{-73}	-23^{+150}_{-30}	-110^{+60}_{-55}
					χ_{b1} (s-s)					
M (GeV)	9.869^{+24}_{-51}	10.177^{+47}_{-71}	10.063^{+23}_{-24}	9.926^{+15}_{-48}	10.05^{+03}_{-10}	10.134^{+15}_{-33}	10.01^{+01}_{-26}	10.08^{+03}_{-23}	10.03^{+06}_{-21}	10.05^{+06}_{-23}
Γ (MeV)	700^{+250}_{-200}	360^{+100}_{-200}	310^{+180}_{-350}	208^{+77}_{-390}	88^{+204}_{-14}	-5^{+160}_{-38}	-61^{+53}_{-120}	-74^{+138}_{-36}	-122^{+108}_{-138}	-280^{+107}_{-155}
					h_b (s-s)					
M (GeV)	10.02^{+31}_{-03}	10.222^{+20}_{-17}	10.0084^{+97}_{-66}	9.929^{+15}_{-14}	10.142^{+57}_{-15}	10.118^{+16}_{-46}	10.02^{+01}_{-28}	10.08^{+03}_{-23}	10.04^{+08}_{-22}	10.08^{+10}_{-21}
Γ (MeV)	493^{+370}_{-70}	510^{+170}_{-350}	312 ± 200	218^{+57}_{-560}	118^{+26}_{-89}	-68^{+270}_{-51}	-33^{+89}_{-110}	-76^{+100}_{-68}	-134^{+110}_{-150}	-250^{+130}_{-110}

3.7 PROBING THE SYSTEMATIC EFFECT OF CHANGING THE TIME WINDOW

Besides the extrapolation routines to remove the unphysical α and $\widetilde{\Delta}$ dependence from the results, the effect of the time window used for the spectral reconstruction on the mass and width predictions should also be studied. By construction, lattices at lower temperature have access to a longer range of time data than lattices at higher temperature. Recall that, according to Eq. (2.5.6), we anticipate the reconstruction to be more accurate as the time extent increases. Thus, for a more accurate comparison of temperatures, we also reconstruct the 'zero-temperature' ($T = 47$ MeV) mass and width from correlators truncated to the maximum time window accessible by each lattice temperature (i.e., we compare the spectrum derived from $T = 95$ MeV ($N_\tau = 64$) correlator with the $T = 47$ MeV correlator truncated to the window $\tau \in [0, 64)$).

Figures 3.25-3.32 show the zero-temperature ($T = 47$ MeV) results for the ground state mass and width, given by the extrapolation routine outlined in §2.8, as a function of the temporal extent $\tau \in [0, \tau_2)$ provided to the Backus-Gilbert routine. Since our reconstructions use the full temporal extent, N_τ, available at each lattice temperature, the zero-temperature plots should reveal, upon comparison with Figs. 3.15-3.21, any systematic effects caused by changing the time window provided to the spectral reconstruction routine.

Figures 3.26, 3.28, and 3.30 exhibit the same increasing width as seen in the finite temperature results, suggesting that the dependence of the ground state width on the temperature may instead be a facet of the restricted time window at large temperature and not some physical mechanism such as broadening of the peak due to melting of the state. This is expected to some extent with Backus-Gilbert reconstruction, as restricting the number of observations causes broadening of the underlying averaging functions, which in turn worsens the resolving power.
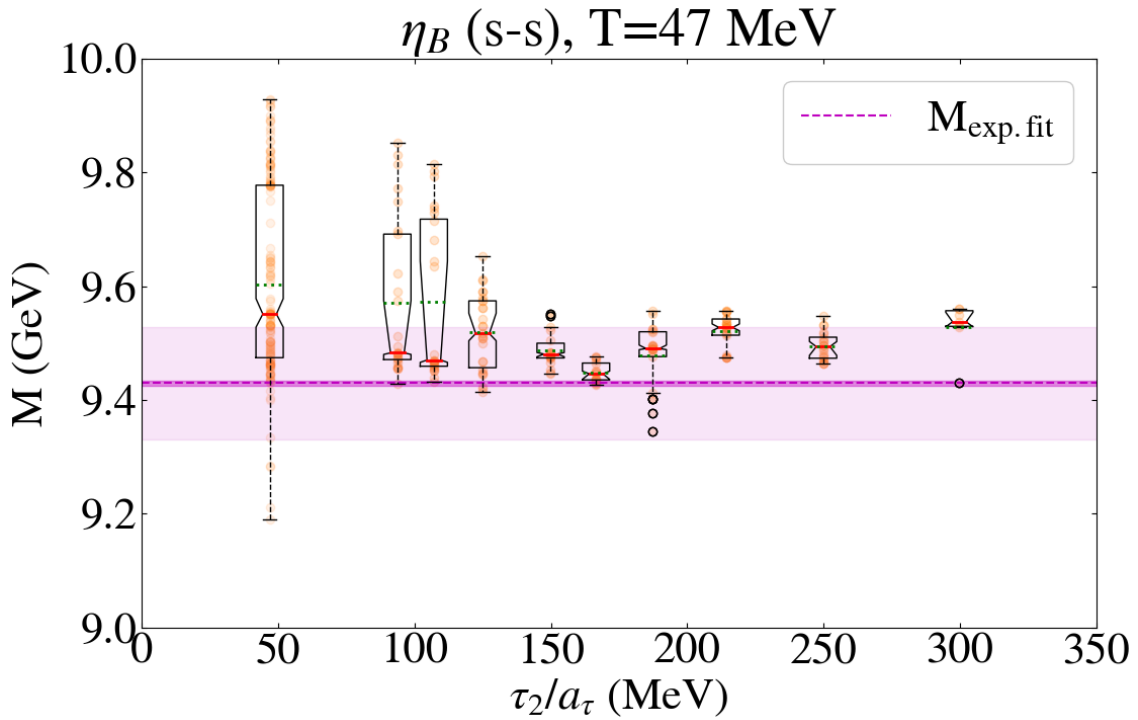
Figure 3.25: Box-plot of the zero-temperature ($T = 47$ MeV) estimate of the ground state mass, M, for the η_b meson (s-s) versus temporal extent of the spectral reconstruction ,τ_2/a_τ. The solid red and dashed green lines represent the ensemble median and mean respectively, with the body of the box representing the confidence interval and the whiskers denoting the inliers (see §3.6 for detail). The magenta line represents the expected mass from exponential fits to the correlator.
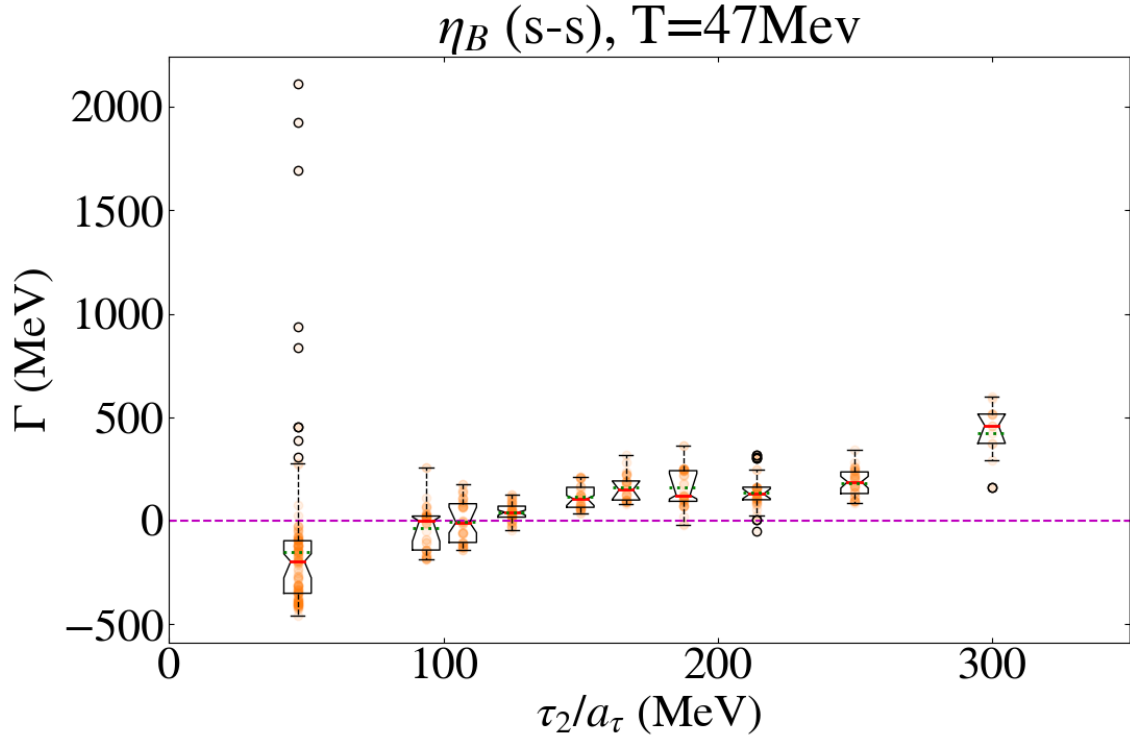
Figure 3.26: Box-plot of the zero-temperature ($T = 47$ MeV) estimate of the ground state width, Γ, for the η_b meson (s-s) versus temporal extent of the spectral reconstruction, τ_2/a_τ. The solid red and dashed green lines represent the ensemble median and mean respectively, with the body of the box representing the confidence interval and the whiskers denoting the inliers (see §3.6 for detail). 66
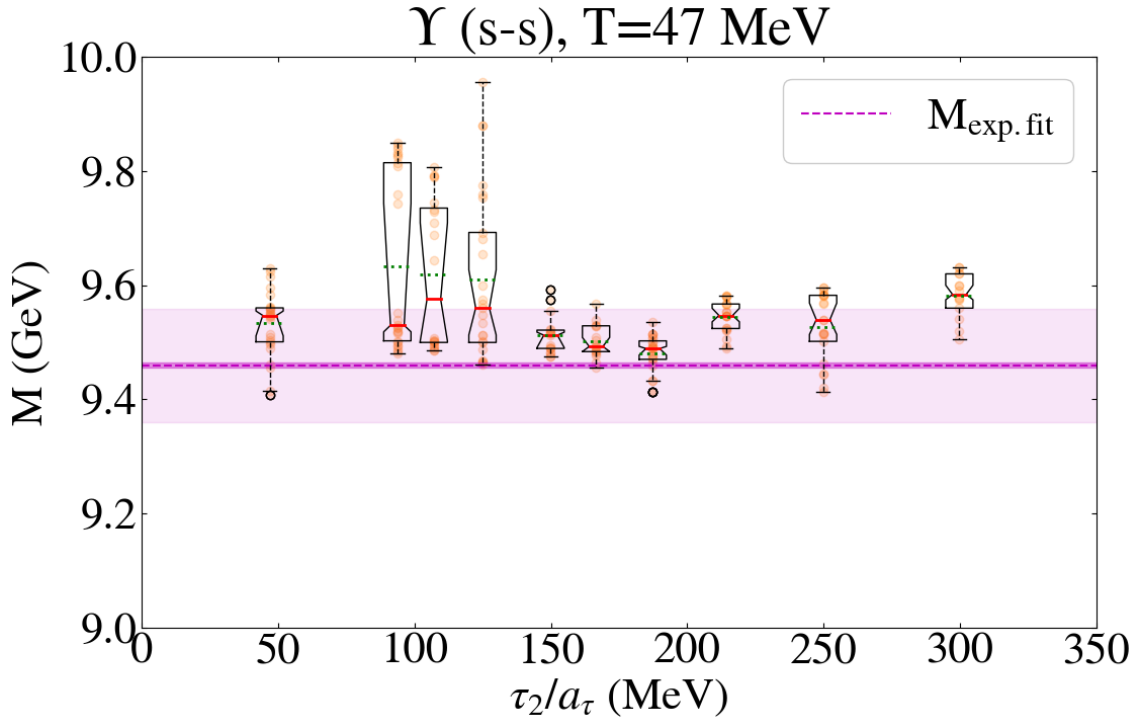
Figure 3.27: Box-plot of the zero-temperature ($T = 47$ MeV) estimate of the ground state mass, M, for the Υ meson (s-s) versus temporal extent of the spectral reconstruction, τ_2/a_τ. The solid red and dashed green lines represent the ensemble median and mean respectively, with the body of the box representing the confidence interval and the whiskers denoting the inliers (see §3.6 for detail). The magenta line represents the expected mass from exponential fits to the correlator.
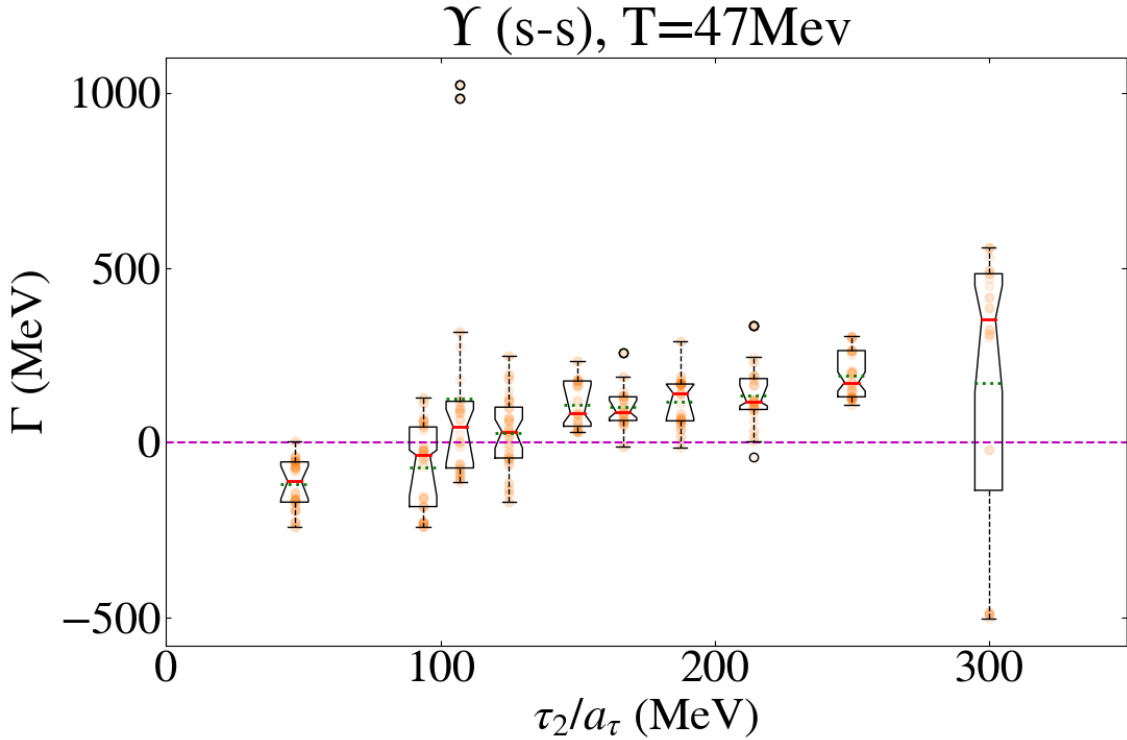
Figure 3.28: Box-plot of the zero-temperature ($T = 47$ MeV) estimate of the ground state width, Γ, for the Υ meson (s-s) versus temporal extent of the spectral reconstruction, τ_2/a_τ. The solid red and dashed green lines represent the ensemble median and mean respectively, with the body of the box representing the confidence interval and the whiskers denoting the inliers (see §3.6 for detail).

67
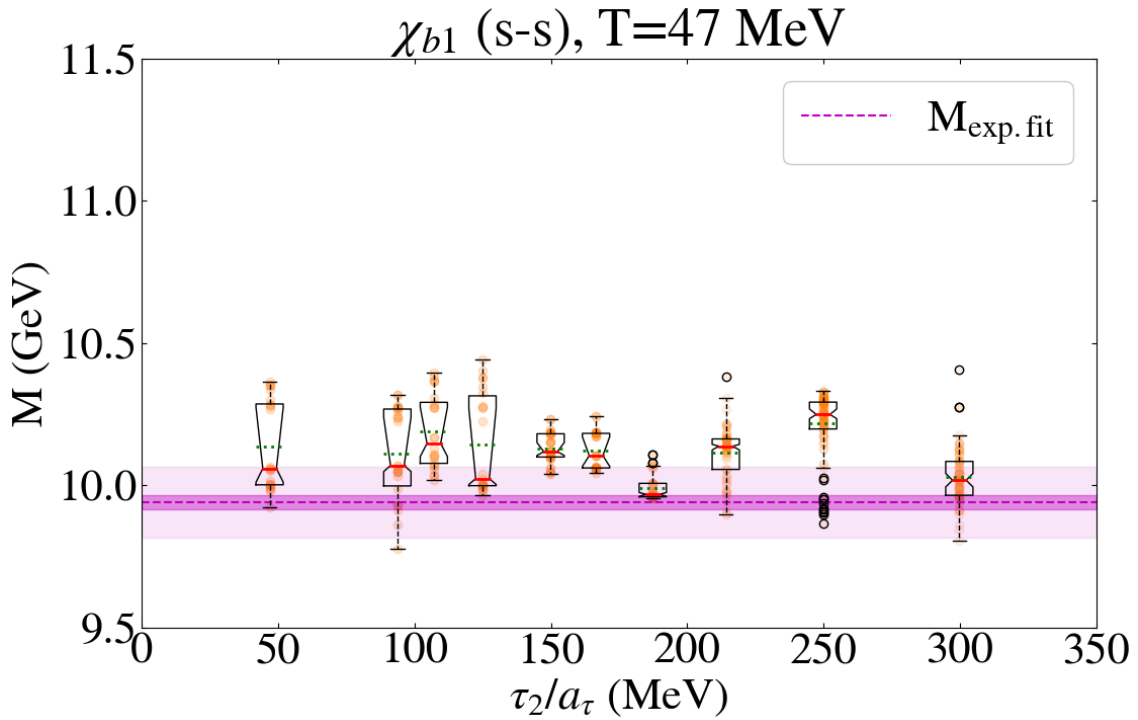
Figure 3.29: Box-plot of the zero-temperature ($T = 47$ MeV) estimate of the ground state mass, M, for the χ_{b1} meson (s-s) versus temporal extent of the spectral reconstruction, τ_2/a_τ. The solid red and dashed green lines represent the ensemble median and mean respectively, with the body of the box representing the confidence interval and the whiskers denoting the inliers (see §3.6 for detail). The magenta line represents the expected mass from exponential fits to the correlator.
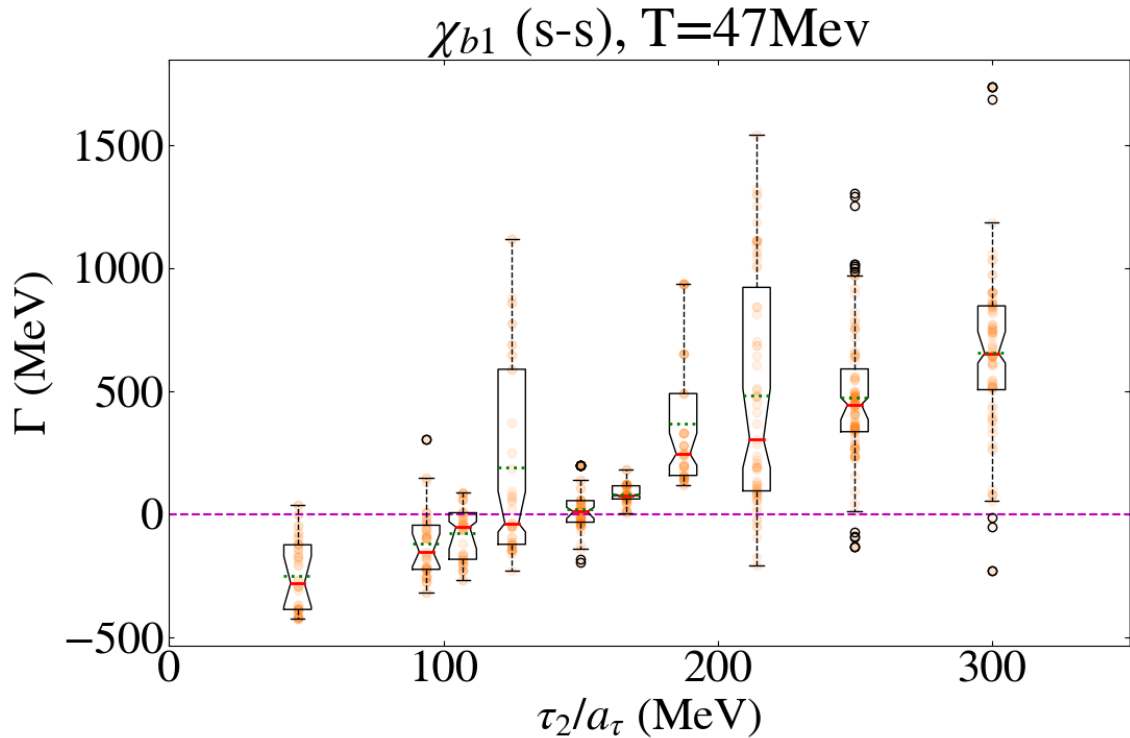
Figure 3.30: Box-plot of the zero-temperature ($T = 47$ MeV) estimate of the ground state width, Γ, for the χ_{b1} meson (s-s) versus temporal extent of the spectral reconstruction, τ_2/a_τ. The solid red and dashed green lines represent the ensemble median and mean respectively, with the body of the box representing the confidence interval and the whiskers denoting the inliers (see §3.6 for detail).

68
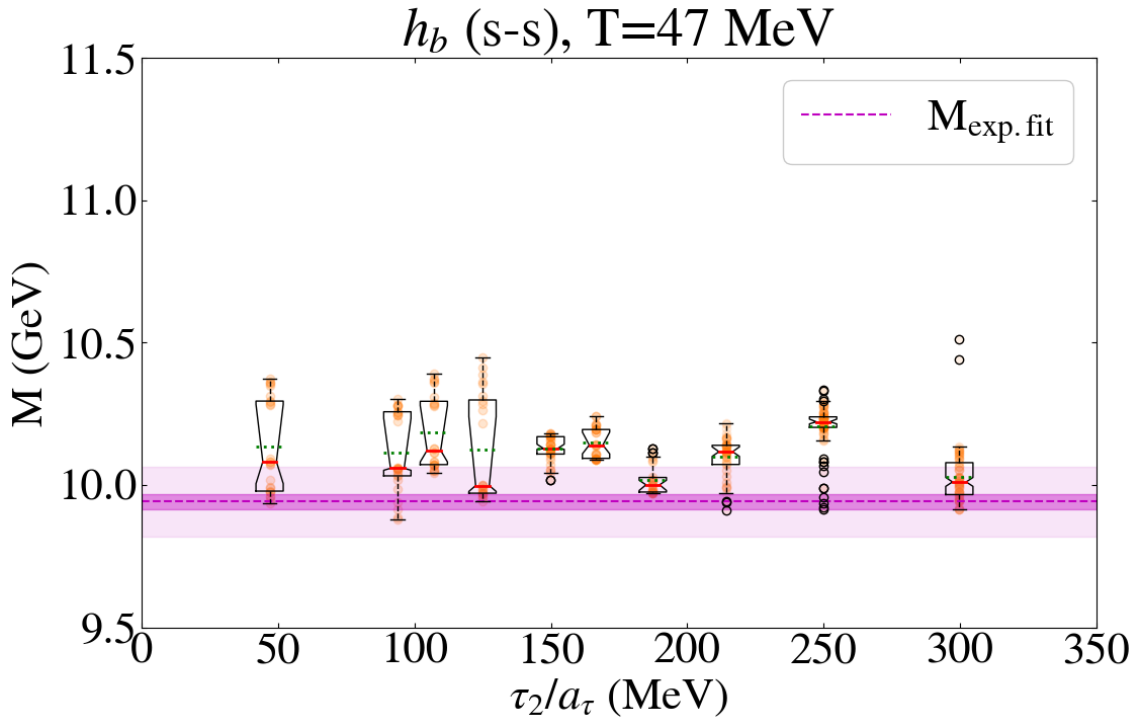
Figure 3.31: Box-plot of the zero-temperature ($T = 47$ MeV) estimate of the ground state mass, M, for the h_b meson (s-s) versus temporal extent of the spectral reconstruction, τ_2/a_τ. The solid red and dashed green lines represent the ensemble median and mean respectively, with the body of the box representing the confidence interval and the whiskers denoting the inliers (see §3.6 for detail). The magenta line represents the expected mass from exponential fits to the correlator.
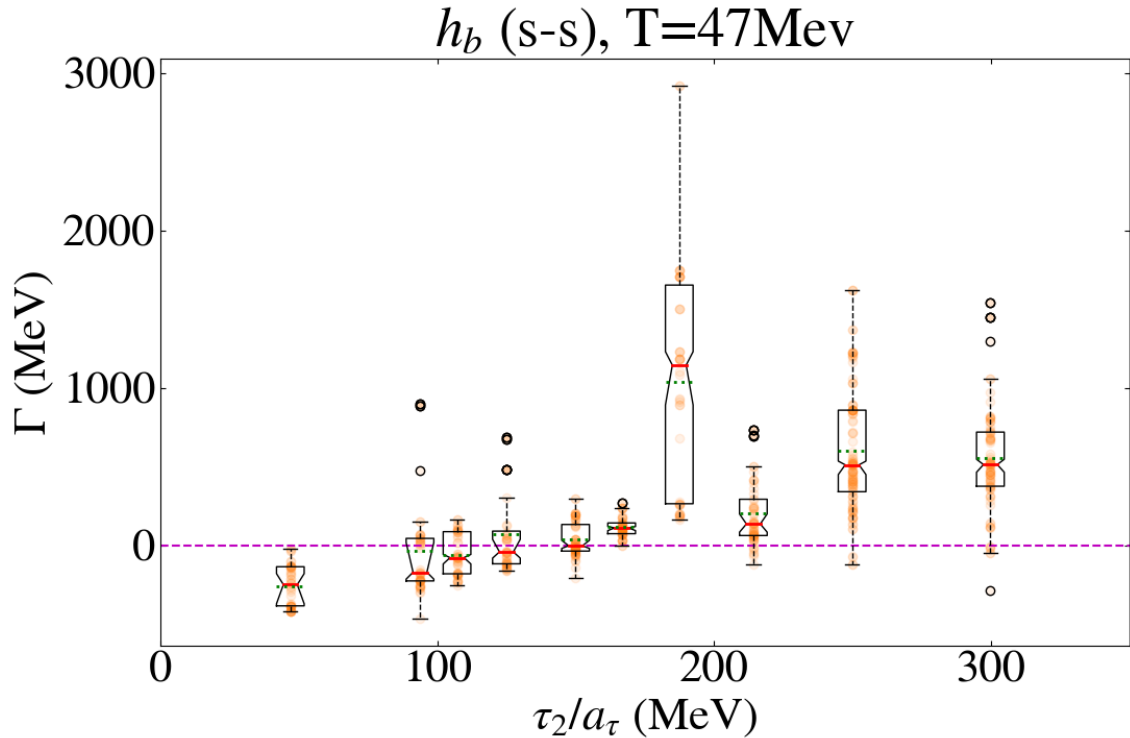

Figure 3.32: Box-plot of the zero-temperature ($T = 47$ MeV) estimate of the ground state width, Γ, for the h_b meson (s-s) versus temporal extent of the spectral reconstruction, τ_2/a_τ. The solid red and dashed green lines represent the ensemble median and mean respectively, with the body of the box representing the confidence interval and the whiskers denoting the inliers (see §3.6 for detail).   69

CHAPTER 4

LIMITATIONS OF LAPLACE-SHIFT IMPROVEMENT

In this chapter we discuss the effects of the Laplace shift improvement technique on the spectral error predicted by the Backus-Gilbert method. We propose to impose a maximum bound on the allowed Laplace shift, argued on the basis of the form of the variance for a general two-point correlator.
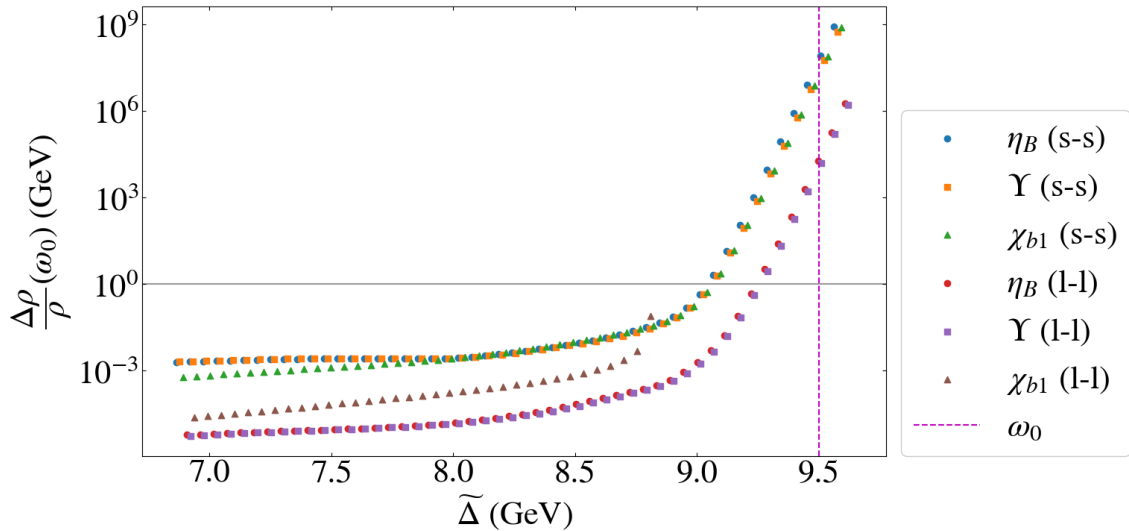
Figure 4.1: Plot of the relative error in the reconstructed spectrum as a function of the adjusted Laplace shift parameter $\widetilde{\Delta}$. In this example, we measure the error at $\omega_0 = 9.5$ GeV, $T = 47$ MeV and $\alpha = 10^{-3}$. Note the logarithmic scale on the y-axis.

There are two main issues which arise when applying the Laplace shift transform to improve the reconstruction resolution. The first is that stronger shifts move the important features of the spectrum, such as the ground state, increasingly closer to the edge of the fit window. The technique relies on the assumption that the spectrum is negligible outside of the window to avoid unwanted amplification of the shifted spectrum by the oscillations of the analytically-continued averaging functions. The second issue which arises is the stability of the error under strong shifts. Figure

4.1 shows the relative error in the spectrum at $\omega_0 = 9.5$ GeV as a function of the adjusted shift parameter, $\widetilde{\Delta}$. At some value of $\widetilde{\Delta}$, seemingly regardless of the underlying channel, the relative error begins to suddenly increase exponentially. Recall that the error in the reconstructed spectrum is given by

$$\Delta\rho^2(\omega) = \sum_{\tau,\tau'} c_\tau \text{Cov}(G)_{\tau\tau'} c_{\tau'}. \tag{4.0.1}$$

Under the shift transform defined in Eq. (2.8.2), the covariance matrix transforms as

$$\text{Cov}(G)_{\tau\tau'} \Rightarrow e^{\Delta\cdot\tau} \text{Cov}(G)_{\tau\tau'} e^{\Delta\cdot\tau'} \tag{4.0.2}$$

and since at large τ the unshifted correlator, $G(\tau)$, behaves like $G(\tau) \sim e^{-M\tau}$, with M the mass of the target state, we would expect that the covariance matrix become 'flat' in the limit where $\Delta \to M$.

We can estimate the degree of 'flat-ness' of the covariance matrix by measuring its condition number, κ. Let $\boldsymbol{\Sigma}_\Delta = \text{Cov}(G; \Delta)$; the condition number is then defined as

$$\kappa(\Delta) = \text{cond}\left[\boldsymbol{\Sigma}_\Delta\right] = ||\boldsymbol{\Sigma}_\Delta|| \cdot ||\boldsymbol{\Sigma}_\Delta^{-1}|| = \frac{\sigma_{\max}}{\sigma_{\min}}, \tag{4.0.3}$$

where σ are the singular values of the covariance matrix, obtained using singular-value decomposition, and $|| \cdot ||$ denotes the Frobenius norm, $||A|| = \sqrt{\sum_{i,j} |a_{ij}|^2}$. Figure 4.2 shows the condition number as a function of the shift parameter, Δ, calculated from the $T = 47$ MeV ($N_\tau = 128$) correlator truncated to the time window $\tau \in [0, \tau_2)$. Naively, one would expect the condition number to be a minimum when $\Delta = M$, which appears at first glance to be supported by Fig 4.2. Figure 4.3 shows the predicted mass (of which the value of Δ at $\min[\kappa]$ is a proxy) as a function of a_τ/τ_2, for several choices of meson channel, with the expected masses derived from single-exponential fits overlaid. Fig. 4.3 shows that the predicted mass for all channels lie below the expected values, contrary to the naive expectation.

4.1 Connection with Parisi-Lepage Statistical Scaling

In order to understand why the mass predicted by the condition number method is less than one would expect given the channel, we must turn to G. Parisi [79] and G.P. Lepage [80] who first elucidated this phenomena in the 1980s.

Consider the correlation function for some general state, H, obtained by acting
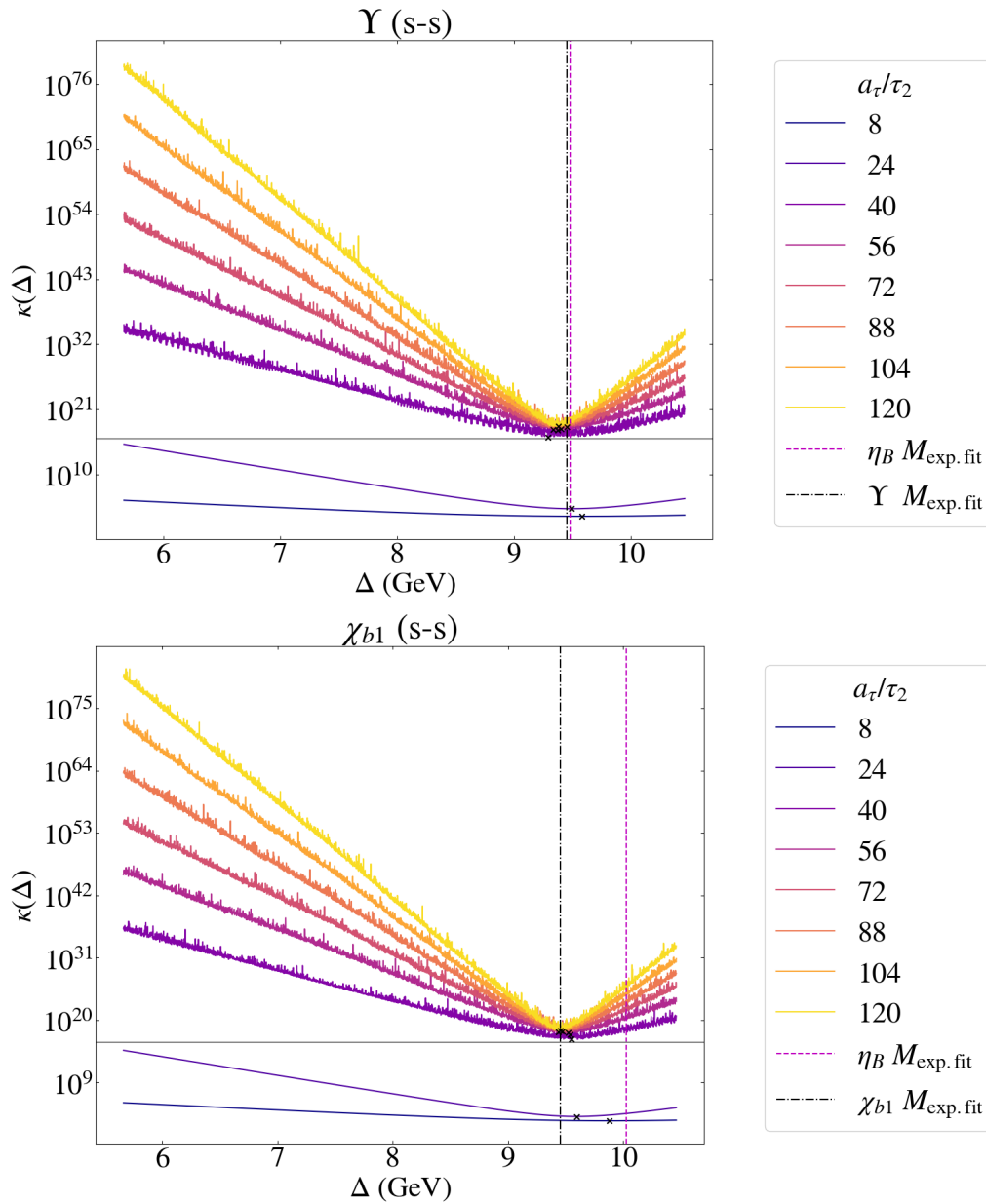
Figure 4.2: Covariance matrix condition number, $\kappa(\Delta)$, versus Δ for the Υ meson (s-s) *Top* and χ_{b1} meson (s-s) *Bottom* at several values of a_τ/τ_2. The largest lattice size $N_\tau = 128a_\tau$ ($T \simeq 47$ MeV) has been used to maximise the available choices of a_τ/τ_2. The black crosses denote the minimum of the condition curve (the predicted masses shown in Fig. 4.3) and the black and magenta lines correspond to the the single-exponential fit estimate of the pseudoscalar and channel masses respectively. The grey horizontal line at $\kappa = 10^{-16}$ corresponds to the precision threshold of 64-bit floating point numbers (the maximum number of decimal places which may be represented is 16, thus the largest computable condition is 10^{-16}).
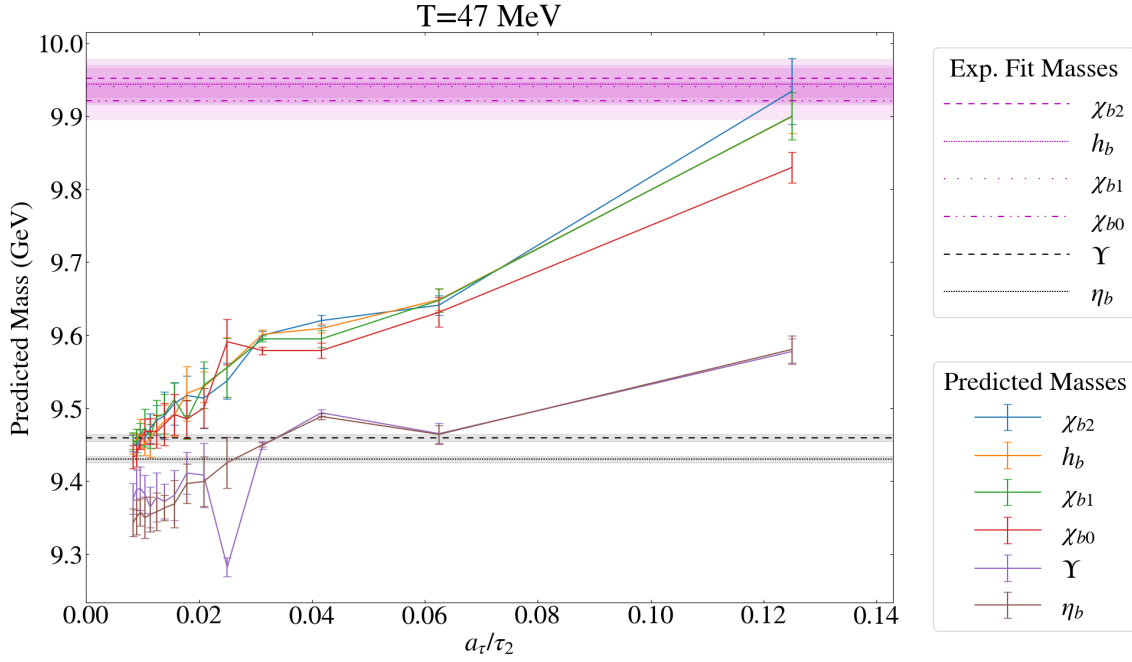
Figure 4.3: Predicted mass for a collection of meson channels versus the time-window extent a_τ/τ_2.

Table 4.1: Matrices appearing in the (relativistic) interpolating operators and the associated quantum numbers and meson states for b-quarkonia, with light sector quarkonia for reference [6].

Γ	$^{2S+1}L_J$	J^{PC}	$u\bar{u}$	$b\bar{b}$
γ_5	$^1S_0$	0^{-+}	π	η_b
γ_i	$^3S_1$	1^{--}	ρ	Υ
$\gamma_i\gamma_j$	$^1P_1$	1^{+-}	b_1	h_b
$\mathbb{1}$	$^3P_0$	0^{++}	a_0	χ_{b0}
$\gamma_i\gamma_5$	$^3P_1$	1^{++}	a_1	χ_{b1}

the current operator, J, on the vaccuum:

$$G_H(x,t) = \langle J_{x,t} J_0^\dagger \rangle \tag{4.1.1}$$

$$\equiv \langle 0| J_{x,t} J_0^\dagger |0\rangle . \tag{4.1.2}$$

Converting to the Heisenberg picture and inserting a complete set of eigenstates $\mathbb{1} = |n\rangle \langle n|$ yields

$$\langle J_{x,t} J_0^\dagger \rangle = \langle 0| J_0 e^{-\hat{H}t} J_0^\dagger |0\rangle \tag{4.1.3}$$

$$= \sum_n |\langle 0| J_0 |n\rangle|^2 e^{-E_n t}, \tag{4.1.4}$$

where we have used the relation $\hat{H}\left|n\right\rangle = E_n\left|n\right\rangle$. The higher energy states are suppressed at long-t, such that we may approximate

$$G_H(x,t) \approx e^{-Mt}, \tag{4.1.5}$$

with M the ground state. Recalling the Monte Carlo method for estimating expectation values outlined in §1.4.1, the correlator is given by

$$G_H(x,t) = \left\langle \mathcal{G}_i(x,t) \right\rangle, \tag{4.1.6}$$

where $\mathcal{G}_i$ represent the values of $\langle J_{x,t} J_0^\dagger \rangle$ evaluated over each of the N_i Monte Carlo configurations. The correlator, G_H, is real-valued by charge-conjugation symmetry, but $\mathcal{G}_i$ need not be in general, giving rise to the following conditions on $\mathcal{G}_i$:

$$\lim_{N_i \to \infty} \left\langle \mathrm{Im}(\mathcal{G}_i) \right\rangle = 0, \qquad \forall x, t\ , \tag{4.1.7}$$

$$\lim_{N_i \to \infty} \left\langle \mathrm{Im}(\mathcal{G}_i)\mathrm{Re}(\mathcal{G}_i) \right\rangle = 0, \qquad \forall x, t\ , \tag{4.1.8}$$

where we highlight that the second condition is a direct consequence of the first. The variance associated with Eq. (4.1.6) is given by

$$
\begin{aligned}
\mathrm{Var}(G_H) &= E[(\mathcal{G}_i - G_H)^*(\mathcal{G}_i - G_H)] \\
&\approx \langle \mathrm{Re}(\mathcal{G}_i)^2 \rangle - G_H^2,
\end{aligned} \tag{4.1.9}
$$

where, by Eq. (4.1.7), we have used the relation $\langle \mathcal{G}_i^* \rangle \approx \langle \mathrm{Re}(\mathcal{G}_i) \rangle \approx G_H$. We can build upon this picture by noting that

$$2 \left\langle \mathrm{Re}(\mathcal{G}_i)^2 \right\rangle = \langle |\mathcal{G}_i|^2 \rangle + \langle \mathcal{G}_i^2 \rangle, \tag{4.1.10}$$

and so the variance becomes

$$\mathrm{Var}(G_H) = \frac{1}{2}\langle |\mathcal{G}_i|^2 \rangle + \frac{1}{2}\langle \mathcal{G}_i^2 \rangle - G_H^2. \tag{4.1.11}$$

The first term in Eq. (4.1.11) corresponds to the correlation function of a state with hadron-antihadron quantum numbers, whereas the second term represents the correlation function of a state containing hadron-hadron quantum numbers. The third term, being the square of the correlator, only corresponds to a single hadron.

There is no conservation law preventing the rearrangement of the quantum numbers in $\langle |\mathcal{G}_i|^2 \rangle$ to give the hadron-antihadron quantum numbers of some associated channel $\widetilde{H}$. Figure 4.4 shows how the quantum numbers of a proton-antiproton pair may be rearranged into three pions. If we choose a channel such that $M_{\widetilde{H}} < M_H$ then we find that, by Eq. (4.1.4)

$$\text{Var}(G_H) \approx e^{-2M_{\widetilde{H}}t} \tag{4.1.12}$$

and thus the signal to noise ratio goes as $e^{-(M_H - M_{\widetilde{H}})t}$ (i.e., our signal worsens with t). It is well-known that the signal to noise ratio for the proton on the lattice grows exponentially with $3/2m_\pi$ and is known colloquially as the "Golden Window" problem [81, 82].
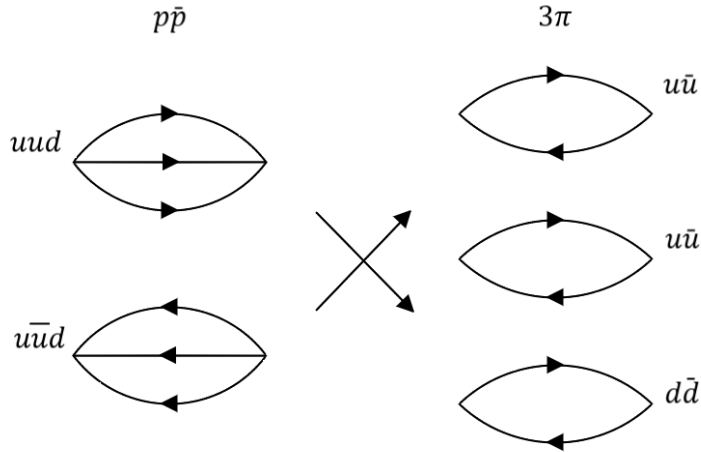
Figure 4.4: Diagram showing how a proton-antiproton pair may be rearranged to produce three pions.

The same principle outlined in Fig. 4.4 also holds for mesonic systems – however, the pictorial representation is no longer as persuasive as the quark structure is unchanged under the rearrangement of quantum number. Instead, consider the two-point correlator corresponding to some meson comprised of two quarks, where we explicitly denote the flavours by (1) and (2):

$$G_\Gamma(x, t) = \langle J_{x,t}^{(1,2)} J_0^{\dagger(1,2)} \rangle , \tag{4.1.13}$$

where $J_{x,t}^{(1,2)} = \bar{q}_{x,t}^{(1)} \Gamma q_{x,t}^{(2)}$ and $\Gamma \in \{\mathbb{1}, \gamma_i, \gamma_5, \gamma_i\gamma_5, \gamma_i\gamma_j\}$. The first term in Eq. (4.1.11) is then given by

$$
\begin{aligned}
\langle |\mathcal{G}_i|^2 \rangle &= \langle J_{x,t}^{(1,2)} J_0^{\dagger(1,2)} \left(J_{x,t}^{(1,2)} J_0^{\dagger(1,2)} \right)^{\dagger} \rangle \\
&= \langle \left(\bar{q}_{x,t}^{(1)} \Gamma q_{x,t}^{(2)} \right) \left(\bar{q}_0^{(2)} \Gamma q_0^{(1)} \right) \left(\bar{q}_0^{(2)} \Gamma q_0^{(1)} \right)^{\dagger} \left(\bar{q}_{x,t}^{(1)} \Gamma q_{x,t}^{(2)} \right)^{\dagger} \rangle \\
&= \langle \left(\bar{q}_{x,t}^{(1)} \Gamma q_{x,t}^{(2)} \right) \left(\bar{q}_0^{(2)} \Gamma q_0^{(1)} \right) \left(\bar{q}_0^{(1)} \Gamma q_0^{(2)} \right) \left(\bar{q}_{x,t}^{(2)} \Gamma_M q_{x,t}^{(1)} \right) \rangle \\
&= \langle \left(\bar{q}_{x,t}^{(2)} \Gamma q_{x,t}^{(1)} \right) \left(\bar{q}_{x,t}^{(1)} \Gamma q_{x,t}^{(2)} \right) \left(\bar{q}_0^{(2)} \Gamma q_0^{(1)} \right) \left(\bar{q}_0^{(1)} \Gamma q_0^{(2)} \right) \rangle \\
&= c_{PS} \langle \left(\bar{q}_{x,t}^{(2)} \gamma_5 q_{x,t}^{(2)} \right) \left(\bar{q}_{x,t}^{(1)} \gamma_5 q_{x,t}^{(1)} \right) \left(\bar{q}_0^{(2)} \gamma_5 q_0^{(2)} \right) \left(\bar{q}_0^{(1)} \gamma_5 q_0^{(1)} \right) \rangle + \text{add. terms,}
\end{aligned}
$$
$$(4.1.14)$$

where we have used $\gamma_5 \Gamma \gamma_5 = \pm \Gamma^{\dagger}$ and have obtained the last line in Eq. (4.1.14) by expanding the terms using the general Fierz identity [83] (see Appendix A.4 for details):

$$
\begin{aligned}
(\bar{\chi}\Gamma\psi)(\bar{\psi}\Gamma\chi) = {}& c_S(\bar{\chi}\chi)(\bar{\psi}\psi) + c_V(\bar{\chi}\gamma_\mu\chi)(\bar{\psi}\gamma_\mu\psi) + c_A(\bar{\chi}\gamma_\mu\gamma_5\chi)(\bar{\psi}\gamma_\mu\gamma_5\psi) \\
&+ c_{PS}(\bar{\chi}\gamma_5\chi)(\bar{\psi}\gamma_5\psi) + \frac{c_T}{2}(\bar{\chi}\sigma_{\mu\nu}\chi)(\bar{\psi}\sigma_{\mu\nu}\psi),
\end{aligned}
$$
$$(4.1.15)$$

where the coefficients, $c_S, c_V, c_A, c_{PS}, c_T$, are the respective scalar, vector, axial, pseudoscalar and tensor coefficients corresponding to Γ and are given in Table 4.2 (see Appendix A.4 for details of their calculation). We also define $\sigma_{\mu\nu} = \frac{1}{2}[\gamma_\mu, \gamma_\nu]$. The additional terms correspond to the additional bilinear products generated during expansion, such as scalar-scalar, vector-vector and also cross-terms such as scalar-vector, etc.

Table 4.2: Fierz identity coefficients for the bilinears of a product of spinors. The calculation of these coefficients is outlined in Appendix A.4.

	c_S	c_V	c_{PS}	c_A	c_T
Γ	$\mathbb{1}$	γ_μ	γ_5	$\gamma_\mu\gamma_5$	$\sigma_{\mu\nu}/\sqrt{2}$
SxS	$1/4$	$1/4$	$1/4$	$-1/4$	$-1/4$
VxV	1	$-1/2$	-1	$-1/2$	0
PSxPS	$1/4$	$-1/4$	$1/4$	$1/4$	$-1/4$
AxA	-1	$-1/2$	1	$-1/2$	0
TxT	$-3/2$	0	$-3/2$	0	$-1/2$

It is evident from the table of coefficients that every choice of Γ contains contributions from the pseudoscalar channel, which is the lightest allowed mesonic state.

Finally, using Wick's theorem,

$$\langle \eta_{i_1} \bar{\eta}_{j_1} \ldots \eta_{i_n} \bar{\eta}_{j_n} \rangle = \frac{1}{Z} \int \prod_{k}^{N} d\eta_k d\bar{\eta}_k \; \eta_{i_1} \bar{\eta}_{j_1} \ldots \eta_{i_n} \bar{\eta}_{j_n} \exp\left(\sum_{l,m}^{N} \bar{\eta}_l M_{lm} \eta_m \right) \qquad (4.1.16)$$

$$= (-1)^n \sum_{P\{n\}} \text{sign}(P)(M^{-1})_{i_1,j_{P_1}} \ldots (M^{-1})_{i_n,j_{P_n}} \qquad (4.1.17)$$

where $P\{n\}$ denotes the set of permutations, we may express $\langle |\mathcal{G}_i|^2 \rangle$ in terms of the quark propagator $S_{x,t} = M^{-1}$,

$$\langle |\mathcal{G}_i^2| \rangle = \langle \text{Tr}\left[(\gamma_5 S_{0;x,t}^{\dagger(2)} \gamma_5 S_{0;x,t}^{(1)})^2 \right] \rangle + \text{add. terms}, \qquad (4.1.18)$$

where the additional terms contain contributions from the other channels and also disconnected bubble contributions from the pseudoscalar channel along with spontaneous flavour-changing diagrams which are disallowed.

In Fig. 4.3 we can see this behaviour in action. For a set of meson channels with varying quantum numbers, the predicted mass from the variance tends toward the predicted value for the η_b (the pseudoscalar) meson mass as $a_\tau/\tau_2 \to 0$.

The signal-to-noise problem has attracted renewed interest in recent years, with studies of the magnitude-phase decomposition of the correlator[82] showing that the signal-to-noise problem is generated by the complex phase of the correlator, whereas the magnitude does not exhibit such behaviour. Furthermore, encouraged by improvements in high-performance computing and the onset of new machine-learning assisted approaches [84, 85] pure-gauge $SU(2)$ focuses on a technique known as *neural-network contour deformation*, wherein the path integral is deformed such that desired observables become transformed into new observables which posses the same expectation values but exhibit different variance properties.

The Coulomb-Gauge Gluon Propagator

5.1 Introduction

The gluon, being the mediator of the strong force, encodes much of the 'richness' of quantum chromodynamics. Yet, six or so decades after its existence was first postulated, there is still much which is unknown about its dynamics. It is believed in the physics community that the secret to color confinement should be contained within the properties of the gluon. However, so far no analytic proof of color confinement has been shown in *any* non-Abelian theory, let alone QCD. There exists a plethora of experimental evidence to support this behaviour, such as the absence of observed fractional charges (i.e. free quarks) and the production of hadron cascades in high energy particle-particle collisions. On the lattice, one may probe confinement via a variety of methods, some of which were touched upon in §1.4. Some of these approaches are based on simpler observables made up only of the link variables U_μ, such as the Polyakov loop expectation value, while other approaches include direct calculation of the inter-quark potential which also can act as a test of confinement [14].

In the next two chapters we attempt to test for a confinement signal via studies of the gluon propagator, first in the Coulomb gauge, before extending to the Landau gauge, both calculated using the Fastsum NRQCD ensembles.

5.2 Gauge Fixing, Gribov Copies and Confinement

There is much discussion (and even contention) surrounding the way in which the gluon propagator is expected to change as the system passes through the deconfinement transition. Part of this discussion is fuelled by the fact that the gluon propagator is not a gauge-invariant observable, since it is constructed from the two-

point correlator of the gluon fields, A_μ, and thus must be gauge-fixed, adding an additional layer of complexity to any analysis. Two popular gauges in the literature are the Coulomb gauge,

$$\vec{\nabla} \cdot \vec{A} = \sum_i \partial_i A_i = 0, \tag{5.2.1}$$

where $i = (1, 2, 3)$ and the Landau gauge,

$$\partial_\mu A_\mu = \sum_\mu \partial_\mu A_\mu = 0, \tag{5.2.2}$$

where $\mu = (1, 2, 3, 4)$.

Currently, there are several confinement scenarios based upon studies of the ghost propagator and BRST symmetry (the Kugo-Ojima scenario [86]). The gauge-variance of the quark-antiquark potential (the Gribov-Zwanziger scenario [87, 88]) predicts that the gluon propagator is expected to become suppressed in the infrared. A review of these scenarios and their relation to confinement is given in Ref. [89].

In this analysis, we focus solely on the gluon propagator and will defer discussion on the ghost propagator to a later point. We first consider the Gribov-Zwanziger confinement scenario and, to better understand the motivation of this scenario, we must discuss the Gribov ambiguity. The path integral contains an over-counting of the gauge fields A_μ which is caused by the presence of *gauge orbits*, defined as

$$\text{orb}[A_\mu] = \left\{ A_\mu^\Omega | A_\mu^\Omega = \Omega A_\mu \Omega^\dagger - \frac{i}{g_0} (\partial_\mu \Omega) \Omega^\dagger; \quad \Omega \in SU(N) \right\}. \tag{5.2.3}$$

which are sets of gauge fields that are equivalent under a gauge transformation. This over-counting was formally solved by Fadeev and Popov [90] by incorporating ghost-fields into the path integral to reduce the contributions from the gauge orbit to a single configuration (see Appendix A.5). This procedure is sufficient in the case of Abelian gauge theories such as QED, but it was discovered by Gribov [87] that for non-Abelian gauge theories there exist non-equivalent configurations which also obey a given gauge condition. These configurations are known as Gribov copies and are removed by restricting the path integral to the region where the Fadeev-Popov operator,

$$M[A_\mu^\Omega] = \frac{\delta F[A_\mu^\Omega]}{\delta \Omega}, \tag{5.2.4}$$

with $F[A_\mu^\Omega]$ our gauge condition, is strictly positive-definite. This *first Gribov region*

(FGR) is then denoted by the set

$$\Omega_{\text{Gribov}} = \{A_\mu | F[A_\mu] = 0 \cap M[A_\mu] > 0\}. \qquad (5.2.5)$$

However this still leaves remnant copies, which must be removed by demanding that $F[A_\mu^\Omega]$ be minimized *globally* within the FGR (this is called the *fundamental modular region*) and is in general non-trivial to locate [91].

The original Gribov-Zwanziger confinement scenario states that gauge configurations which lie close to the boundary of the FGR (called the *Gribov horizon*) contribute the most toward the infrared behaviour of the propagator [92], causing the gluon propagator to vanish and an enhanced ghost propagator. However, in the refined Gribov-Zwanziger scenario [93, 94] the gluon propagator is expected to become IR-finite and the ghost propagator divergent. The behaviour of the gluon propagator in the infrared limit is a point of contention in the literature, with several approaches to the study of the scenario yielding contrasting results. This is believed to be exacerbated in part due by the large lattice sizes required to probe the infrared limit [93].

Regardless, the two Gribov-Zwanziger scenarios inspire interest when one is reminded that deconfinement is an inherently gauge-invariant process, whereas the gluon propagator is a gauge-variant quantity. Thus, the essence of this approach is that we should be able to probe the deconfinement transition via measurements of the gluon propagator at different temperatures, regardless of our choice of gauge fixing.

For clarity, we will first discuss the gauge fixing process and subsequent gluon propagator calculation in terms of the Coulomb gauge given in Eq. (5.2.1), and will introduce necessary modifications to support the lattice anisotropy for Landau gauge (Eq. (5.2.2)) in Chapter 6. In the meantime, we shall make explicit the anisotropy of the lattice spacing (i.e., $a = a_\mu$) to support later discussion and highlight once more that a_s and a_τ represent the spatial and temporal lattice spacing, respectively.

The action of fixing the gauge condition given in Eq. (5.2.1) corresponds to (see Appendix A.6 for details) the maximisation of the continuum functional, [92, 95]

$$W[A_\mu] = \sum_\mu \int d^4x \text{Tr} \left[A_\mu^2\right], \qquad (5.2.6)$$

for the continuum gauge fields, A_μ. By discretizing the integral and using the lattice definition of the gluon field, $U_\mu(x) = e^{-ig_0 a_\mu A_\mu(x)}$, we have,

$$A_\mu(x) = \frac{\left\{U_\mu(x) - U_\mu^\dagger(x)\right\}_{\text{traceless}}}{2ig_0 a_\mu} \quad + \quad \mathcal{O}(a^2), \tag{5.2.7}$$

and thus can express the discretised, lattice gauge functional as

$$F[U_\mu^\Omega] = \frac{1}{|\Lambda| N_c(N_d - 1)} \sum_{x,\mu} \text{ReTr}\left[U_\mu^\Omega(x)\right], \tag{5.2.8}$$

which is then minimised with respect to the set of gauge transformations, $\{\Omega\}$, over the entirety of the lattice. The minimisation of Eq. (5.2.8) is not a trivial problem and in general we must use algorithmic approaches which iteratively converge on the maximum of $F[U^\Omega]$ to obtain the set of transformations, $\{\Omega\}$, which fix the gauge. In this work, we employ a pre-existing gauge fixing algorithm [96] based on the over-relaxation method (details of which are outlined in Ref. [97]). Since the process of maximising the gauge fixing functional exhibits stochastic convergence, we measure the progress of the gauge fixing algorithm using the criterion

$$(\vec{\nabla} \cdot \vec{A})^2 \equiv \frac{1}{|\Lambda|} \sum_{x \in \{\Lambda\}} \sum_{c=1}^{N_c^2 - 1} \left[\vec{\nabla}_{\text{latt}} \cdot \vec{A}^c(x)\right]^2, \tag{5.2.9}$$

where we have defined the lattice 3-divergence

$$\vec{\nabla}_{\text{latt}} \cdot \vec{A}^c(x) = \sum_i \frac{A_i^c(x + a_s \hat{i}) - A_i^c(x)}{a_s}, \tag{5.2.10}$$

with A_i^c the Gell-Mann components of the SU(3) gauge fields, A_i. The gauge fixing condition given in Eq. (5.2.8) is evaluated independently over each time slice, with the gauge fixing algorithm halting when $(\vec{\nabla} \cdot \vec{A})^2 \leq 10^{-16}$.

5.3 Calculating the Gluon Propagator

The instantaneous gluon propagator is defined as the two-point function of the A_μ fields at some time, t,

$$D_{ij}^{ab}(x - y; t) = \frac{1}{|\Lambda|} \langle A_j^a(x, t) A_j^b(y, t) \rangle, \tag{5.3.1}$$

and is tensor-like in the color components, $a, b \in \{1, \ldots, 8\}$ and the spatial Lorentz indices, i, j, where the color components of the gluon fields, A_i, are given by

$$A_\mu(x) = \sum_{a=1}^{N_c^2-1} A_\mu^a(x) T_a, \qquad (5.3.2)$$

with A_μ^a the real-valued color components of A_μ and T_a the set of $N_c \times N_c$ matrices which span the Lie algebra $\mathfrak{su}(N_c)$ and form a basis which define the adjoint representation of the group. For $N_c = 3$, $T_a = \lambda_a/2$, with λ_a the Gell-Mann matrices.

In momentum space, the unequal time gluon propagator is given by

$$D_{ij}^{ab}(p; p_4) = \frac{1}{|\Lambda|} \left\langle A_i^a(p, p_4) A_j^b(-p, -p_4) \right\rangle, \qquad (5.3.3)$$

where p is the 3-momentum and the gluon fields in momentum space are given by

$$A_i(p) = \frac{e^{-ig_0 \hat{p} a_s/2}}{2ig_0 a_s} \left[B_i(p) - \frac{1}{3} \mathrm{Tr} B_i(p) \right], \qquad (5.3.4)$$

where for brevity we have defined $B_i(p) \equiv U_i(p) - U_i^\dagger(-p)$, with $U_i(p) \equiv \sum_x e^{-ip \cdot x} U_i(x)$.

We may decouple the scalar propagator, $D(|p|)$, from the tensor-structure of D_{ij}^{ab} using

$$D_{ij}^{ab}(p) = \delta^{ab} \left(\delta_{ij} - \frac{p_i \cdot p_j}{|p|^2} \right) D(|p|), \qquad (5.3.5)$$

which when taking the trace over the color and Lorentz components yields

$$D(|p|) = \frac{2}{(N_c^2 - 1)(N_d - 1)|\Lambda|} \sum_{i,a} \mathrm{Tr} \left[\langle A_i^a(p, p_4) A_i^a(-p, -p_4) \rangle \right], \quad (p \neq 0), \quad (5.3.6)$$

$$D(|p|) = \frac{2}{(N_c^2 - 1) N_d |\Lambda|} \sum_{i,a} \mathrm{Tr} \left[\langle A_i^a(p, p_4) A_i^a(-p, -p_4) \rangle \right], \qquad (p = 0). \quad (5.3.7)$$

The lattice momentum, $\hat{p}_i$, which arises as the conjugate coordinate to x_i, is given by

$$\hat{p}_i = \frac{2\pi x_i}{a_s N_s} \qquad (5.3.8)$$

where $x_i \in \left(-\frac{N_s}{2}, \frac{N_s}{2} \right]$ and N_s represents the spatial extent of the lattice. It is also necessary to incorporate the one-loop momentum correction based on the form of the lattice action used. For the naive Wilson action, corrections to the (four-

dimensional) momentum pole $D(q) = 1/q^2$ go as

$$D(q) = \frac{a_\mu^2}{4 \sum_\mu \sin^2 (\hat{q}_\mu a_\mu / 2)}, \tag{5.3.9}$$

and thus we would define the (Wilson) corrected momentum

$$q_\mu^W = \frac{2}{a_\mu} \sin(\hat{q}_\mu a_\mu / 2). \tag{5.3.10}$$

We note that this correction still holds for the case of the three-momentum $|p|$. In the case of a Symanzik-improved action, such as the one used for the FASTSUM ensembles, the corresponding momentum correction is given by [3]

$$q_\mu^I = \frac{2}{a_\mu} \sqrt{\sin^2 \left(\frac{\hat{q}_\mu a_\mu}{2} \right) + \frac{1}{3} \sin^4 \left(\frac{\hat{q}_\mu a_\mu}{2} \right)}. \tag{5.3.11}$$

Unless otherwise specified, plots containing q correspond to the corrected momentum while $\hat{q}$ will correspond to the momentum as calculated in Fourier space (i.e. Eq. 5.3.8).

5.3.1 RENORMALIZATION IN THE COULOMB GAUGE

Since the Coulomb gauge has an inherent gauge freedom along the temporal axis, one may assume that the static propagator, given by

$$D_{\text{static}}(|p|) = \sum_{p_4} D(p_4, |p|), \tag{5.3.12}$$

correctly averages out any dependence on the temporal momentum p_4. However, previous studies [14, 98] suggest that this procedure is incorrect as the gluon propagator exhibits spurious scaling on finite lattices. In the continuum limit, we expect the gluon propagator to approach the leading-order (from perturbation theory at $|p| \to \infty$) form

$$D_{\text{tree}}(|p|) = \int dp_4 \, \frac{1}{|p|^2 + p_4^2} = \frac{1}{2|p|}. \tag{5.3.13}$$

On the lattice, one must integrate over the Brillouin zone corresponding to p_4, given by

$$D_{\text{latt}}(|p|) = \int_{-\pi/a_\tau}^{\pi/a_\tau} \frac{dp_4}{2\pi} \frac{1}{|p|^2 + p_4^2} = \frac{1}{|p|\pi} \arctan \left(\frac{\pi}{a_\tau |p|} \right). \tag{5.3.14}$$

The additional $|p|$ dependence means that the lattice analogue of the static propagator is no longer multiplicatively renormalized. It should be noted, however, that the propagator at fixed energy, p_4, should be free of such scaling violations and thus would allow one to study the gluon propagator at fixed p_4, at the expense of smaller statistics.

The authors of Ref. [98] suggest an alternative approach to the static propagator calculation which restores the multiplicative renormalizability. The idea is to factorise the 3-momentum and energy components using the relation

$$D(|p|) = f(|p|)g(z), \tag{5.3.15}$$

where we have defined $z = \xi p_4/|p|$, with ξ the lattice anisotropy. We can calculate the scaling factor $g(z)$ by comparing the bare propagator at some energy, p_4, with the zero-energy, $p_4 = 0$, propagator $D(|p|, 0)$,

$$g(z) = (1+z)^2 \frac{D(|p|, p_4)}{D(|p|, 0)}, \tag{5.3.16}$$

where we define $g(0) = 1$. Fitting the above with a function of the form

$$\hat{g}(z) = (1 + z^2)^\alpha, \tag{5.3.17}$$

for the exponent, α, allows one to remove the z-dependence from the bare propagator by calculating the f-factor

$$f(|p|) = \frac{1}{N_\tau} \sum_{p_4} \frac{D(|p|, p_4)}{\hat{g}(z)} = \frac{1}{N_\tau} \sum_{p_4}, D(|p|, p_4)(1 + z^2)^{-\alpha} \tag{5.3.18}$$

and thus we may express the static form of the bare gluon propagator as $D(|p|) = f(|p|)/|p|$. Once the p_4 dependence has been averaged out, we may renormalize the bare propagator via the usual approach by comparing with the leading order behaviour at some renormalization point, μ, far into the continuum:

$$D_\mu(|p|)\Big|_{\mu=\infty} = \frac{1}{2|p|}, \tag{5.3.19}$$

where we note that the gluon propagator is multiplicatively renormalized, i.e.

$$D_\mu(|p|)\Big|_{\mu=\infty} = Z(\mu) D_{\text{latt}}(|p|). \tag{5.3.20}$$

Table 5.1 shows the value for the fit parameter, α, versus lattice temperature and corresponding temporal extent. We wish to highlight how remarkably close each value of α is to unity, suggesting that the modifications from the method outlined above produce a static propagator not far removed from the naïve static propagator given in Eq. (5.3.12). It should be noted that this behaviour was also observed by the authors of the scheme, where they found that the modification was very small for a wide range of couplings [98]. Although this scheme was originally devised for use with the isotropic Coulomb gauge case, studies using anisotropic lattices [91] suggest that this scheme is still applicable when $\xi = a_s/a_\tau > 1$.

Table 5.1: Table of $g(z)$ fit parameters, α, (see Eq. (5.3.17)) versus lattice temperature.

T/T_c	0.28	0.57	0.76	1.01	
α	1.00025(34)	0.99990(66)	1.00031(89)	0.9996(12)	$\ldots$
N_{cfg}	185	241	224	334	
T/T_c	1.14	1.51	2.27	3.03	4.54
α	1.0000(14)	1.0003(20)	0.9993(35)	0.9987(54)	1.000(11)
N_{cfg}	450	235	196	124	123

5.4 ESTIMATING THE EFFECTIVE MASS OF THE GLUON

We can test the infra-red behaviour of the gluon propagator against that predicted by the various confinement scenarios by estimating the effective mass associated with the propagator. For a free, massless particle in three dimensional space, the propagator behaves as

$$D(p) \sim \frac{1}{2|p|}, \tag{5.4.1}$$

and diverges as $p \to 0$, whereas the free, massive particle contains a mass term

$$D(p) \sim \frac{1}{\sqrt{|p|^2 + m^2}}, \tag{5.4.2}$$

and is finite for $p \to 0$. The effective mass can be estimated via a variety of ways: the Gribov formula [87], derived from variational Hamiltonian approaches, gives a form for this effective mass in Coulomb gauge as a function of $|p|$:

$$\frac{D(|p|; \mu)}{|p|}\bigg|_{\mu=\infty} = \frac{1}{\sqrt{|p|^4 + M_{\mathrm{IR}}^4}}. \tag{5.4.3}$$

This is equivalent to the Yukawa-inspired form for a massive particle,

$$D(|p|; \mu)\Big|_{\mu=\infty} = \frac{1}{\sqrt{|p|^2 + m(|p|)^2}}, \tag{5.4.4}$$

when $m(|p|) = M_{\mathrm{IR}}^2/|p|$ (i.e. the effective mass is itself a function of the momentum). If $m(|p|)$ diverges as $|p| \to 0$, then one may conclude that the effective mass is infinite and the gluon no longer can propagate, thus becoming confined.

In our analysis we attempt to fit both Eqs. (5.4.3) and (5.4.4) to the infrared propagator. When fitting the infrared region, we (unless otherwise specified) fit the propagator in the region $|p| \in [0, p_{\mathrm{max}})$ and will measure the fit parameters as a function of p_{max}. Thistests any dependence of the effective mass on the momentum, as we expect to be the case for the fit corresponding to Eq. (5.4.4).

5.5   Averaging and data-cutting routines

In order to minimise the effect that discretisation artefacts have on the propagator calculation, we employ a series of averaging and slicing routines which are outlined in detail in Ref. [3]. As with the previous section, we shall first outline the data cutting routines as applicable in the case of Coulomb gauge and leave any modifications required to support Landau gauge until a subsequent section.

It is a well-known fact that the discretization procedure needed for the lattice formalism introduces artefacts caused by the finite lattice spacing. However, when working with vector-like quantities on the lattice an additional source of error arises due to the breaking of $O(N_d)$ rotational hypersymmetry by the finite spacing. This means that, for example, some quantity measured at a position $\boldsymbol{r} = (0, 0, 3, 4)$ is not expected to be equivalent to the same quantity measured at position $\boldsymbol{r'} = (0, 0, 0, 5)$, despite the fact that $|\boldsymbol{r}| = |\boldsymbol{r'}|$. This is because continuous rotational symmetry is explicitly broken. In general, we find that values for the propagator generated on-axis are affected the most by discretization errors, whereas the behaviour is more uniform for those close to the body-centred diagonal (BCD) vector, $\hat{x}_{\mathrm{BCD}} = 1/\sqrt{N_d} \sum_i^{N_d} \hat{n}_i$ with $\hat{n}_i$ the unit vector in the ith direction.

Although $O(N_d)$ symmetry is broken by the lattice, the subgroup $\mathbb{Z}(N_d)$ is preserved. For Coulomb gauge, where the time direction is explicitly unfixed, we anticipate permutations amongst the set of spatial coordinates to yield equivalent values for the gluon propagator. This gives rise to the first routine, which we shall call

$\mathbb{Z}(3)$ averaging. For example, if $q(x, y, z) = (3, 2, 1)$ then we expect the (static) propagator to obey

$$D(3, 2, 1) = D(1, 3, 2) = D(2, 1, 3) = D(1, 2, 3) = D(2, 3, 1) = D(3, 1, 2),$$

and so average over this set of equivalent points.

The second set of procedures involve slicing the data such that momenta which are far offset from the BCD (i.e. close to on-axis) are removed. This can be achieved by restricting momenta to within a certain defined radius, $\hat{r}$, of the three-dimensional BCD vector, $\hat{x}_{\text{BCD}} = 1/\sqrt{3}\,(1, 1, 1)$, in what is known in the literature as a *cylinder* cut. The radius is given by

$$\hat{r} = |\hat{p}| \sin(\theta_{\hat{p}}), \tag{5.5.1}$$

with the angle $\theta_{\hat{p}}$ measured with respect to the BCD vector,

$$\theta_{\hat{p}} = \arccos\left(\frac{\hat{p} \cdot \hat{x}_{\text{BCD}}}{|\hat{p}|}\right). \tag{5.5.2}$$

We can further restrict the momenta to produce a *cone* cut by limiting the angle $\theta_{\hat{p}}$. Following the procedure outlined in Ref. [3], we restrict the momenta to a radius of $1\hat{p}/a_s = 2\pi/a_s N_s$ for cylinder cuts and an angle of $\theta = 0.174$ rad. $\approx 10°$ for the cone cuts.

The cone cut is considered to be more of an ultraviolet cut by its construction, and so to preserve as much data as possible in the infra-red (in order to estimate the effective mass) we may employ a 'hybrid' cut where the angular restriction is dropped below when $q \lesssim 1$ GeV.

5.6 Results

In this section and the following, we use our value of the pseudo-critical transition temperature, T_{pc} (see Table 3.1), as a stand-in value for the 'confinement temperature', which we shall denote T_c. If our estimate of the pseudocritical transition temperature is a fair representation of the temperature at which the deconfinement transition is expected to occur, then we should observe a difference in the behaviour of the gluon propagator as our temperature passes through $T = T_c$. We also note that, unless otherwise stated, all plots showing multiple temperatures are given a small stagger in the momentum $|p|$ to aid the visual separation of overlapping data
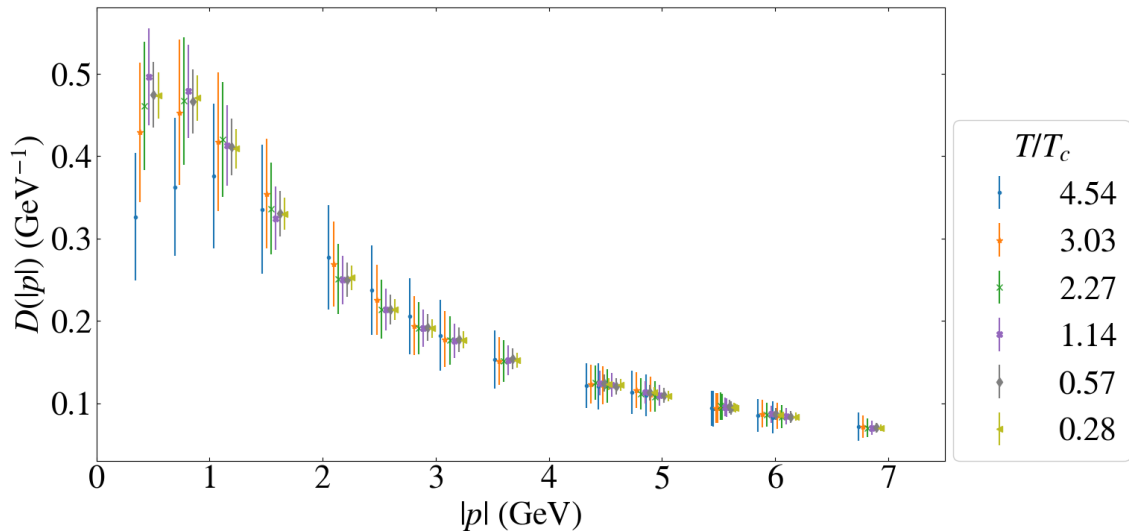
Figure 5.1: Values for the renormalized ($\mu = 6$ GeV) gluon propagator as a function of momentum for several temperatures. The number of data points shown has been thinned (see text for detail) and results for only some temperatures are shown to aid visual comparison.

and, where there is an abundance of data points, we omit results for intermediary temperatures and reduce the number of data points shown to maintain intelligibility. In cases where we perform fits to the data, we stress that all available data (subject to cutting routines) is used for the fit.

Figure 5.1 shows the gluon propagator (renormalized at $\mu = 6$ GeV) as a function of the 3-momentum $|p|$, for a range of temperatures spanning the transition temperature, T_c. There is a remarkable agreement in the form of $D(|p|)$ across the expected transition about $T = T_c$, with the propagator only departing in the infrared ($|\hat{p}| \lesssim \pi/a_s$) from the general trend beyond $T = 3T_c$. This corresponds to our smallest available lattices, $\Lambda_8 = 8 \times 32^3$ and $\Lambda_{12} = 12 \times 32^3$. Figure 5.2 shows the renormalized ($\mu = 6$ Gev) dressing function $Z(|p|) = 2|p|D(|p|)$ as a function of $|p|$ at several temperatures, which we expect to approach unity at large $|p|$. The spurious scaling of $D(|p|)$ is visible at large momenta as the dressing function departs from the expected one-loop result of $Z(|p|) \sim 1$. This 'drooping' effect seen at large $|p|$ has been previously attributed to inconsistencies between the momentum correction (Eq. (5.3.11)) and the leading-order behaviour at the continuum in the Landau gauge [99]. Figure 5.3 further probes the IR behaviour by plotting the propagator at select temperatures as a ratio of our zero-temperature ($T = 47$ MeV$= 0.3T_c$,
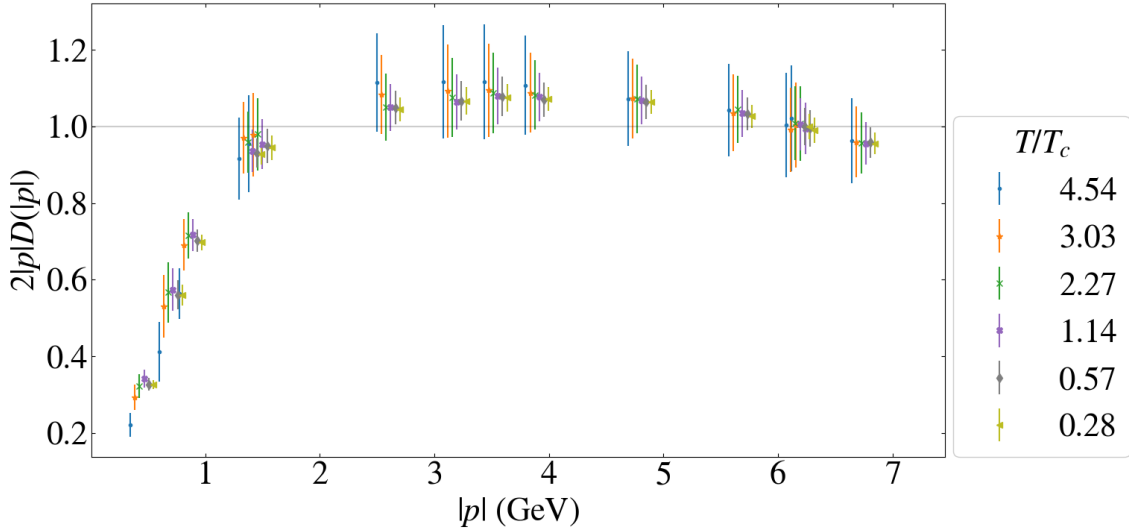
Figure 5.2: Renormalized ($\mu = 6$ GeV)Coulomb gauge gluon propagator as a ratio of the tree level form for several lattice temperatures. The number of data points shown has been thinned (see text for details) and results for only some temperatures are shown to aid visual comparison.

$\Lambda_{128} = 128 \times 32^3$) ensemble in the region $|p| < \pi/a_s$, where we define

$$R_{128}(|p|;T) = \frac{D(|p|;T)}{D(|p|, T = 0.3T_c)}. \tag{5.6.1}$$

The small-$|p|$ temperature effects are now readily highlighted by Figure 5.3.

Having shown a potential sensitivity of the propagator to temperature far above T_c, we now present the results of the effective mass fits. Figure 5.4 shows the Yukawa-inspired mass (Eq. (5.4.4)) as a function of $|p|$ for several values of the temperature. We can see that $m(|p|)$ appears to plateau below $|p| \sim 1$GeV for $T \lesssim 2T_c$, but rapidly increase for $T \gtrsim 2T_c$, suggesting that the effective mass may diverge at higher temperatures. In Figure 5.5 we plot the mass estimate corresponding to the Gribov formula, given in Eq. (5.4.3). Here, we fit the Gribov formula in the momentum window $|p| \in [0, |p|_{\max})$ and show the mass as a function of $|p|_{\max}$. Linearly extrapolating $M_{\mathrm{IR}}(|p|)$ from below $|p|_{\max} < 2$GeV to $|p|_{\max} = 0$ (shown in Figure 5.6 and detailed in Table 5.2) again suggests that the effective mass plateaus below $T = 2T_c$ whilst for $T > 2T_c$ we see an increase in M_{IR} proportional to T.
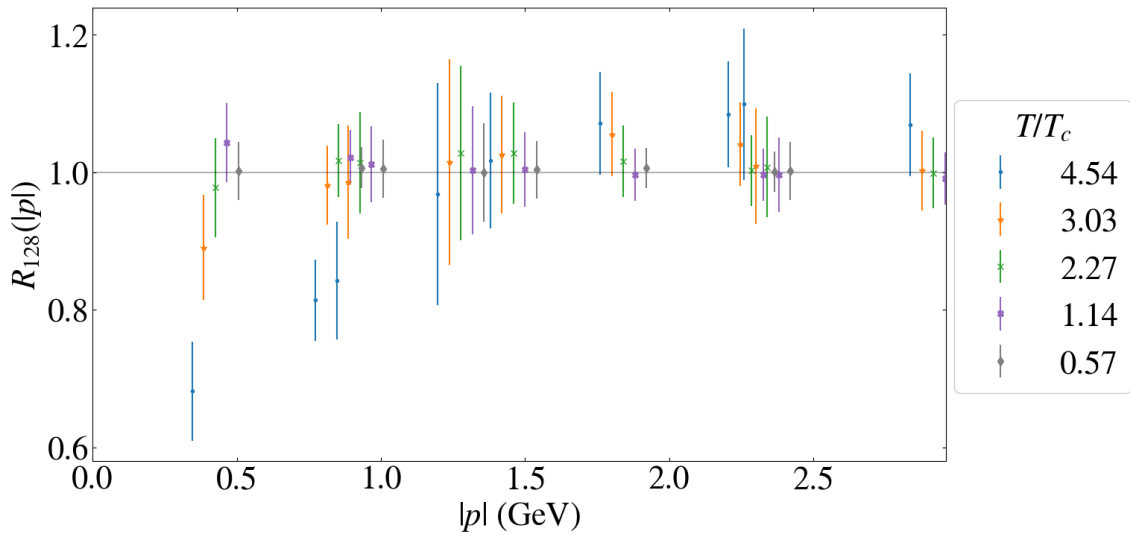
Figure 5.3: Values for the renormalized ($\mu = 6$ GeV) gluon propagator as a fraction of the zero-temperature ($T = 47$ MeV$=0.3T_c$) propagator for select values of T/T_c.
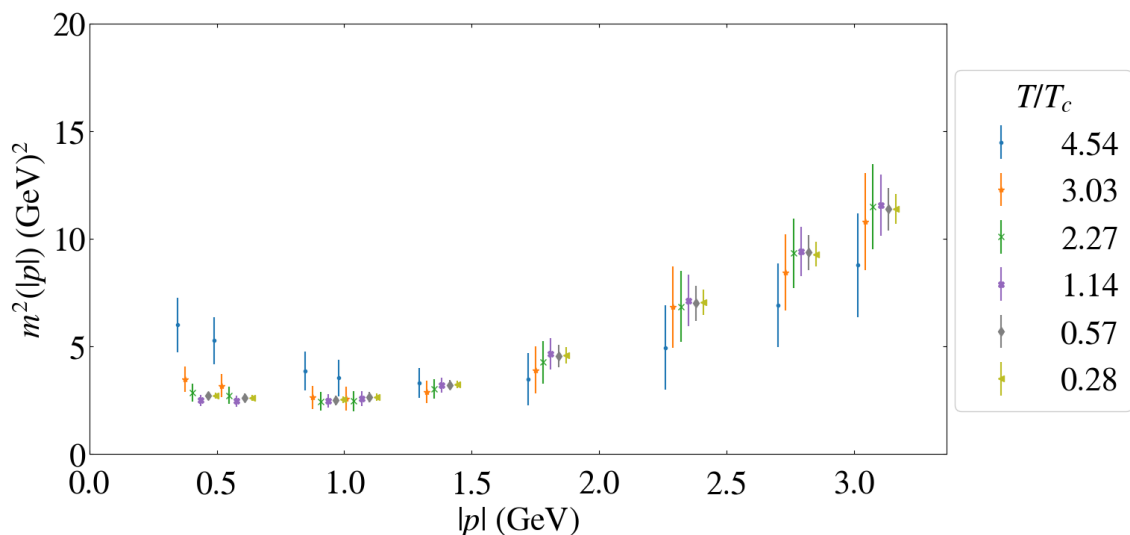
Figure 5.4: Yukawa-inspired mass fit parameter, $m(|p|)$, as a function of $|p|$ for a range of lattice temperatures.
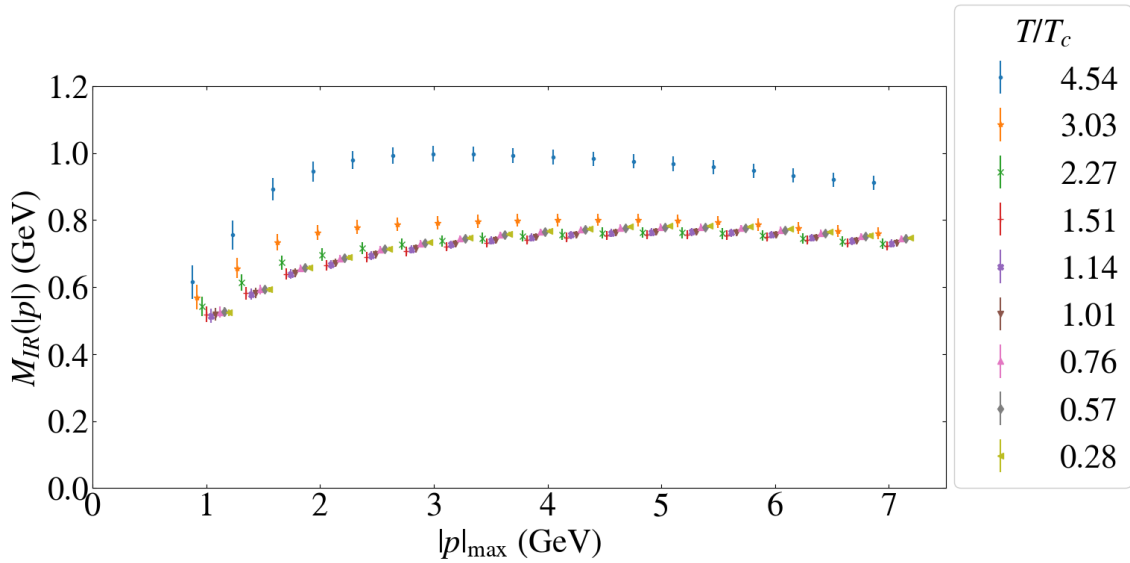
Figure 5.5: Gribov mass fit parameter, $M_{\text{IR}}(|p|)$, as a function of the fit cut-off, $|p|_{\max}$, for a range of lattice temperatures.
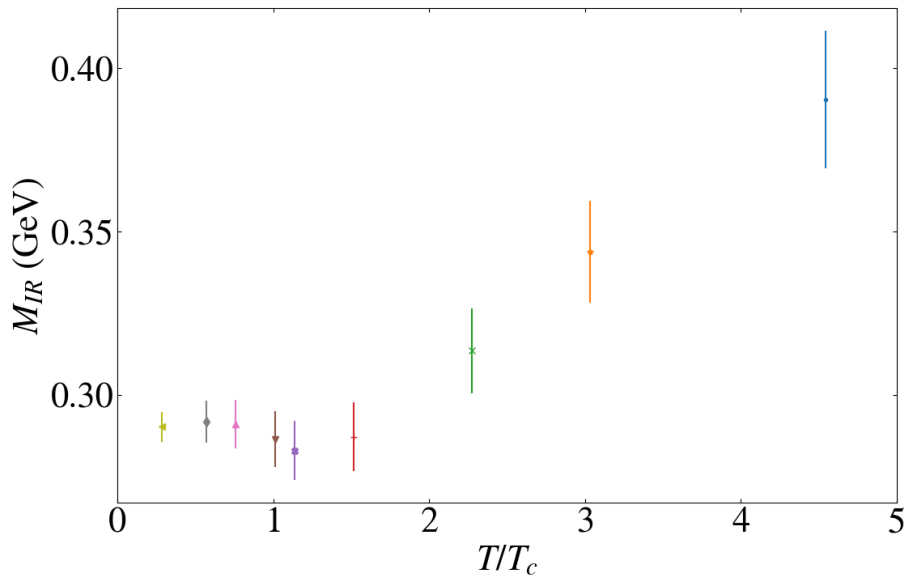
Figure 5.6: Extrapolated Gribov mass fit parameter, M_{IR}, for a range of lattice temperatures.

In this chapter we have discussed the different confinement scenarios for the gluon propagator and how they signal confining behaviour. We then calculated the gluon propagator in the Coulomb gauge, where we only observed temperature dependent behaviour far above the expected transition temperature T_c, instead departing from the low-temperature trend around $T = 3T_c$. This behaviour was also reported by the authors of Ref. [14] in SU(2) Yang-Mills, suggesting that this late onset of temperature dependent behaviour may instead be a facet of the choice of gauge,

Table 5.2: Table of the $|p|_{\max} \to 0$ extrapolated Gribov masses, M_{IR}, for each lattice temperature. The χ_ν^2 are the goodness-of-fit values and N_{cfg} the number of configurations used for the extrapolation.

T/T_c	0.28	0.57	0.76	1.01	1.14
M_{IR} (GeV)	0.2904(46)	0.2918(65)	0.2911(75)	0.2865(86)	0.2830(91)
χ_ν^2	12.93	6.33	4.56	3.04	2.64
N_{cfg}	185	241	224	334	450
T/T_c	1.51	2.27	3.03	4.54	
M_{IR} (GeV)	0.287(11)	0.314(13)	0.344(16)	0.391(21)	
χ_ν^2	1.82	1.69	2.37	4.23	
N_{cfg}	235	196	124	123	

rather than a property of the SU(2) theory. They cite previous investigations [100, 101] which posit that the Coulomb gauge propagators do not couple to the physical string tension but instead couple the spatial string tension of the reduced theory, which persists beyond T_c. A separate study into the phases of QC$_2$D suggested that this 'postponement' of deconfinement [102] is caused by an emergent chiral-spin symmetry phase which exists between $T \in [T_c, 3T_c]$, which is consistent with our observations.

CHAPTER 6

THE LANDAU-GAUGE GLUON PROPAGATOR

Table 6.1: Table of various publications on the gluon propagator from both dynamical and quenched lattice QCD methods, along with pure lattice Yang-Mills. Entries which do not use Landau gauge use Coulomb instead. We also remark that "Finite T" includes studies at a single (non-zero) temperature, along with studies at multiple temperatures [3, 7–16].

ArXiv ID	Dynamical	SU(3)	Landau	Finite T	Anisotropic	Year
This work	✓	✓	✓	✓	✓	2023
2206.02320	✓	✓	✓			2022
1912.12086	✓	✓	✓			2019
1401.6908			✓	✓		2014
1311.5707				✓	✓	2013
1212.1102	✓		✓	✓		2012
1207.3029		✓	✓	✓		2012
1105.6185		✓		✓	✓	2011
1011.0007		✓	✓	✓		2010
0811.4635		✓	✓		✓	2008
0008001			✓			2003
0008001		✓	✓	✓		2001
0008001			✓	✓	✓	2000
9803015		✓	✓			1998

In the previous section, we observed a delay in the onset of deconfinement, inferred from the form of the propagator, until at least $T = 3T_c$ in the Coulomb gauge. However, since the temporal extent of the lattice encodes temperature dependence, it is not such a naive assumption that the Coulomb gauge propagator should be expected to exhibit a more complex relationship with any temperature dependent behaviour, as hinted by the existence of the 'spatial' string tension which the Coulomb gauge has been purported to probe [100, 101].

In this chapter, we build upon our Coulomb gauge work by extending our gauge

fixing procedure to incorporate the time direction. This could either be achieved via an independent fixing of the temporal links in the Coulomb gauge to remove the residual gauge freedom, such as the Integrated Polyakov Gauge [98] (IPG) used by the authors of the SU(2) calculation described in [91], or a simultaneous fixing in all four directions which corresponds to the (continuum) Landau gauge condition,

$$\partial_\mu A_\mu = 0. \tag{6.0.1}$$

We will make use of the Landau gauge condition in this work as it is a natural extension of the Coulomb gauge to four dimensions, rather than the IPG which is a transformation upon the temporal links of the already Coulomb-fixed configuration.

For isotropic lattices, Landau gauge fixing is implemented in a similar manner to the Coulomb gauge. Table 6.1 lists a selection of lattice-based analyses which focus on Coulomb and/or Landau gauge gluon propagators on isotropic and/or anisotropic lattices. From our review of the current literature, it appears that there are few attempts at studying the gluon propagator in Landau gauge on anisotropic lattices, and this work is potentially the first to do so at several temperatures using dynamical QCD on anisotropic lattices.

6.1 Landau gauge for anisotropic lattices

Before we delve into the intricacies of modifying the gauge fixing functional to support space-time anisotropy, it is beneficial to discuss the naive anisotropic gauge action,

$$S_W[U; \gamma_g] = \beta \sum_{x \in \{\Lambda\}} \left[\frac{1}{\gamma_g} \sum_{i<j \leq 3} \text{ReTr}[1 - U_{ij}(x)] + \gamma_g \sum_{i \leq 3} \text{ReTr}[1 - U_{i4}(x)] \right], \tag{6.1.1}$$

where γ_g is the bare gauge anisotropy. Expanding the action in terms of the field strength, $F_{\mu\nu}$, for small a yields the tree-level anisotropy, $a_s/a_\tau = \gamma_g = \xi_0$. Just as the bare coupling, β, undergoes renormalization so too does the bare anisotropy. We denote the renormalized gauge anisotropy by $\xi_R = \xi_R(\xi_0, \beta)$.

Since the FASTSUM ensembles make use of anisotropic lattices, modifications must be make to support the difference in lattice spacing. The first necessary mod-
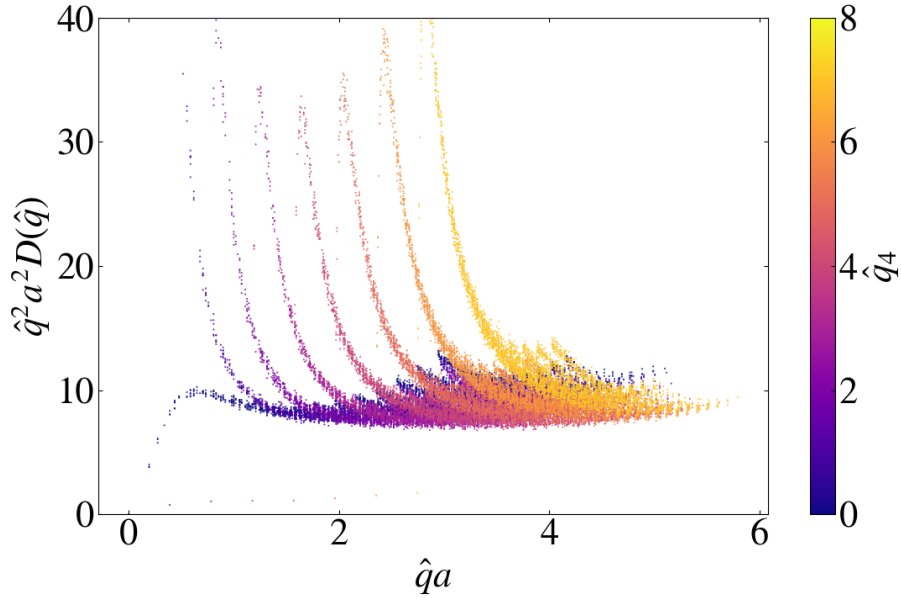
Figure 6.1: Uncut Landau gauge gluon propagator as a function of $\hat{q}a$ with anisotropy corrections applied. In this example, $N_\tau = 16$ ($T = 380$ MeV). Notice the "fanning" which worsens with increasing $\hat{q}_4$, caused by finite spacing errors[3]. The vertical, tendril-like curves are proportional to the temporal lattice extent N_τ and greatly effect the quality of the signal when the lattices are largest.

ifications pertain to the gauge fixing functional, that reads

$$W[A_\mu] = \sum_\mu \int d^4x \, \text{Tr}[A_\mu^2], \qquad (6.1.2)$$

and can be recast in terms of the lattice link variables, U_μ, via a small-a_μ expansion to give

$$F[U^\Omega, \xi] = \frac{1}{|\Lambda| N_c (N_d - 1)} \sum_{x,\mu} \xi_\mu^2 \text{ReTr} \left[U_\mu^\Omega(x) \right]. \qquad (6.1.3)$$

We have defined $\xi_\mu = (1, 1, 1, \xi_R)$. The anisotropic form of the Landau gluon propagator is then given by

$$D_{\mu\nu}^{ab}(q) = \frac{\xi_\mu \xi_\nu}{|\Lambda|} \left\langle A_\mu^a(q) A_\nu^b(-q) \right\rangle. \qquad (6.1.4)$$

Since the 4-momentum carries units of π/a, it must also be modified to account for the difference in lattice spacing:

$$\hat{q}^2 \equiv \sum_i \hat{q}_i^2 + (\xi_R \hat{q}_4)^2. \qquad (6.1.5)$$

6.2   MEASURING THE INFRARED EXPONENT

Studies into the Landau gauge gluon propagator using the Dyson-Schwinger formalism [103] suggest that the gluon dressing function, defined as

$$Z(q^2) = q^2 D(q^2), \tag{6.2.1}$$

exhibits the functional form

$$Z(q^2) \propto (q^2)^{2\kappa}, \tag{6.2.2}$$

in the infrared, with κ a parameter known as the Dyson-Schwinger exponent which is characteristic of the IR behaviour. A value of $\kappa = 0.5$ indicates a finite propagator, whereas values above and below represent infinite and vanishing gluon propagators, respectively [10]. Using the DS formalism, previous studies [103] have found $\kappa \approx 0.595$ and lattice approaches have reported an exponent of $\kappa \approx 0.5$ [10].

6.3   RESULTS

In the following subsection we present results for the gluon propagator in the Landau gauge. We remark that the data follows a similar data cutting routine as outlined in Chapter 5, albeit without the equivalent $\mathbb{Z}(4)$ averaging routine, which cannot be readily implemented in the anisotropic Landau case as the anisotropy term breaks Euclidean 4d hypercubic rotational symmetry. We also note that the cone cut has been extended to incorporate the temporal momentum p_4, adjusted by a factor of ξ_R to account for the anisotropy. It should be noted that this procedure causes a more dramatic cutting of the data, as now only values of p_4 which are approximately divisible by ξ_R are close enough to the BCD to satisfy the cone cut. Figure 6.1 shows the uncut gluon propagator for the 16×32^3 lattice, in which the dramatic discretisation error due to finite lattice spacing is readily apparent. The vertical 'fringes' become more frequent as the temporal momentum extent increases.

We also wish to draw comparisons between Fig. 6.1 and the isotropic Landau gauge propagator shown in Fig. 1 of [3], which shows a similar behaviour albeit without the large vertical 'curves' in $\hat{q}^2 a^2 D(\hat{q})$, which may be an artefact of the lattice anisotropy.

Since our analysis focuses explicitly on the infrared region, which is heavily suppressed by the cone cut, we employ for the Landau gauge propagator a hybrid cut
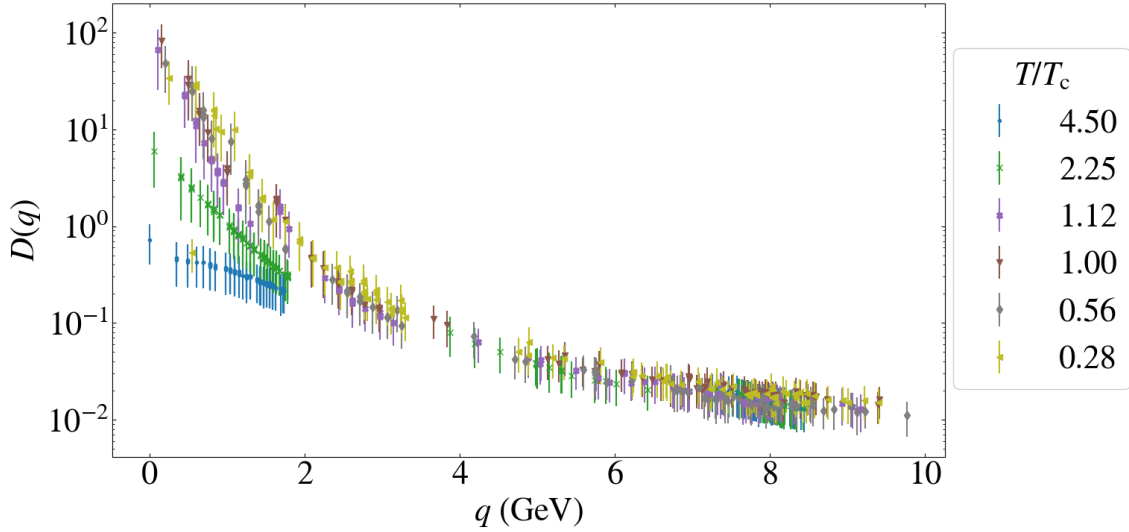
Figure 6.2: Renormalized ($\mu = 8$ GeV) Landau gauge gluon propagator $D(q)$ at several values of T/T_c. Note the logarithmic scale on the vertical axis to accentuate the IR behaviour. For $q < 3$ GeV all data satisfying the cutting routine is shown and for $q \geq 3$ GeV. We show a 'thinned' set of data for visual clarity.

wherein the only the radial restriction (the cylinder cut) is enforced below some $\hat{q}_{min}$, after which we use the cone cut outlined in §5.5. Empirical testing suggests that a cut radius of $\hat{q}_{min} \sim 1$ for the smallest lattices with a gradual decrease to $\hat{q}_{min} = 0$ for the largest lattices gives the best performance.

Figure 6.2 shows the renormalized ($\mu = 8$GeV) gluon propagator at several values of T/T_c. Comparing with the case of the Coulomb gauge propagator, we now see temperature dependent effects in the infrared at a slightly lower temperature, beginning between $T = T_c$ and $T = 2.25\,T_c$. This infrared behaviour is more visible in the dressing function $q^2 D(q)$, shown in Figure 6.3.

Fitting the Dyson-Schwinger exponent discussed in §6.2 proved more of a challenge than expected, possibly exacerbated by the harsh cutting of the data to avoid the finite spacing artefacts. Figure 6.4 shows the result of fitting Eq. 6.2.2 in the fit window $q \in [0, q_{max})$ and measuring the fit result for κ as a function of q_{max}. We note that the constant result for $T = 4.54\,T_c$ is due to a lack of data– the maximum attainable momentum for an 8×32^3 lattice is approximately 2 GeV. The lowest temperature (and most affected by discretization errors) at $T = 0.28\,T_c$ appears to predict a diverging exponent as $q_{max} \to 0$, whereas the remaining temperatures predict $\kappa \lesssim 0.5$.

We can also probe the DS exponent in a manner which is not dependent on the
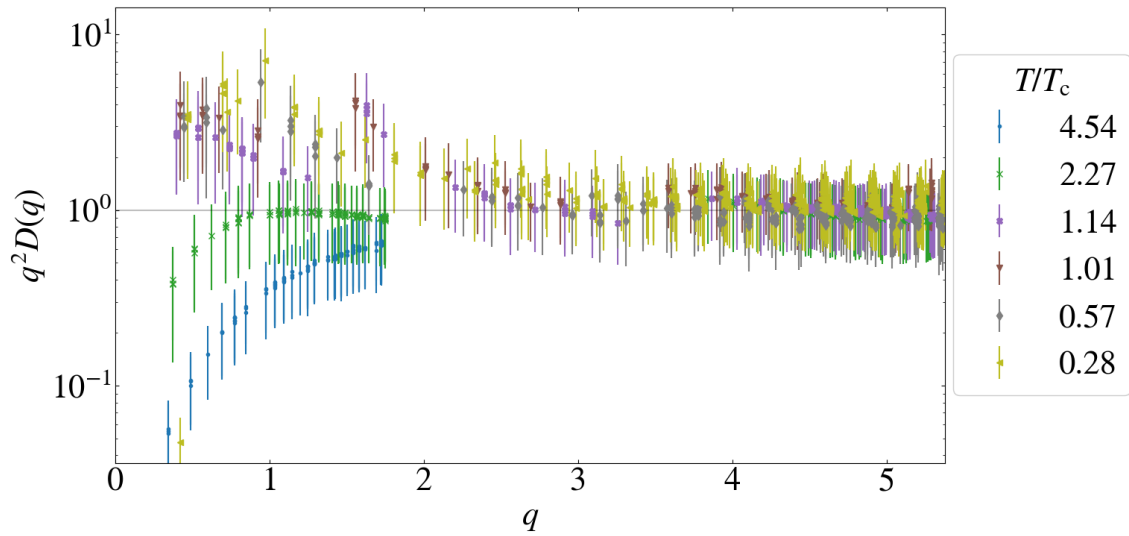
Figure 6.3: Renormalized ($\mu = 8$GeV) dressing function $q^2D(q)$ as a ratio of the tree level form for several values of T/T_c.
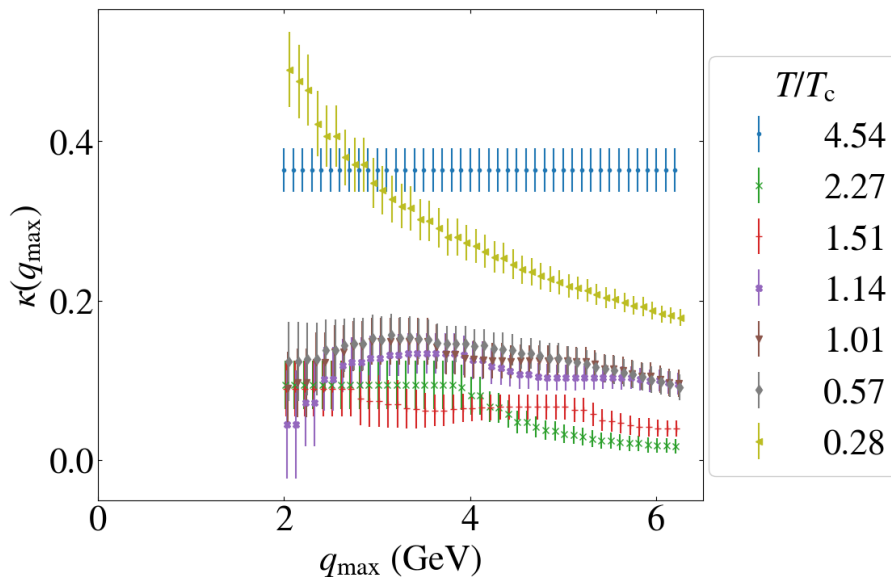
Figure 6.4: Fitted values for the DS exponent κ versus the maximum fitted momentum q_{max} for several values of T/T_c. Note the apparently diverging result for $T = 0.28$ MeV which may be caused by the distortion of the propagator in $q \in [0, q_{max}]$ by the cutting routine.
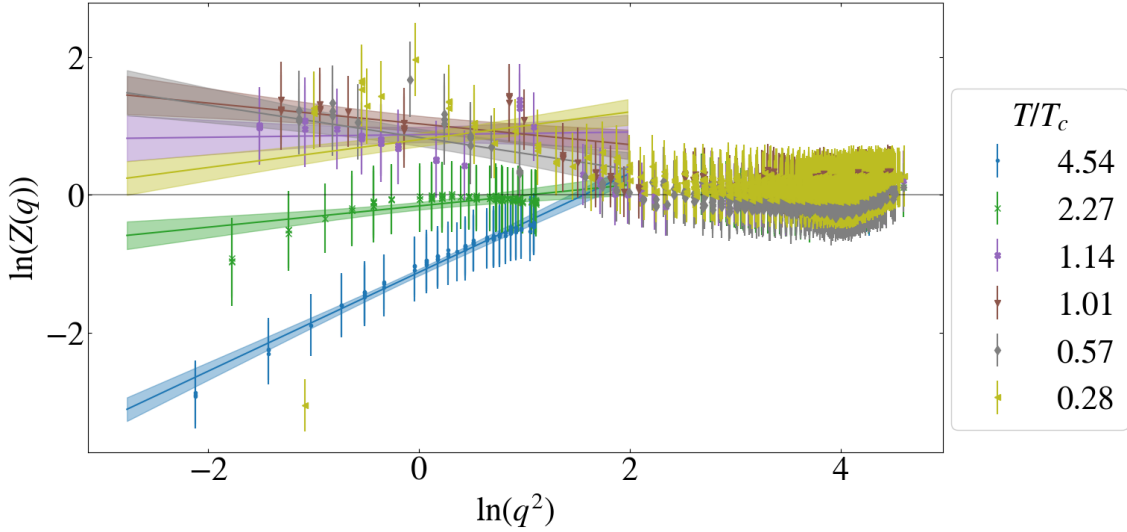
Figure 6.5: Linear fits to the logarithmic dressing function $\ln Z(q)$ for several values of T/T_c.

fit window by rearranging Eq. (6.2.2) into the linear form

$$\ln(Z(q)) = 2\kappa \ln(q^2) + \ln(A), \tag{6.3.1}$$

where A is the coefficient of proportionality corresponding to Eq. (6.2.2). Figure 6.5 plots this linear form for several values of T/T_c, including linear fits to $\ln(Z(q))$ in the range $\hat{q} \in [0, \pi/a_s)$. The values of κ predicted by this method, given in Table 6.2, produce similar results compared with Fig 6.4 where we now see a much smaller exponent, with a finite value for κ predicted for our coldest temperature. Overall, the values for the exponent given in Table 6.2 are much smaller than expected, with the exponents spanning $T \in [0.5\,T_c, 2.5\,T_c]$ being almost zero. This is further supported by effective mass fits in the style of Eq. (5.4.4), where for Landau gauge we now fit the propagator with a function of the form

$$D(q) = \frac{1}{q^2 + m(q)^2}. \tag{6.3.2}$$

Figure 6.6 shows the value of $m(q)^2$ as a function of q for several temperatures, where we can see that for most temperatures (aside from $T = 4.54\,T_c$) the effective mass is consistent with zero, suggesting that the propagator behaves as $D(q) \sim 1/q^2$ in the infrared and thus the corresponding DS exponent for the dressing function $Z(q) = q^2 D(q)$ should be zero, roughly in agreement with the values reported in Table 6.2.

Table 6.2: Values for the Dyson-Schwinger exponent, κ, obtained using the linear fit approach outlined in Eq. (6.3.1) with associated values of the reduced chi-square goodness-of-fit, χ_ν^2.

T/T_c	0.28	0.57	1.01	1.14	2.27	4.54
κ	0.269(55)	-0.117(54)	0.002(60)	0.005(60)	0.092(38)	0.370(32)
χ_ν^2	6.11	0.3	0.11	0.24	0.05	0.03
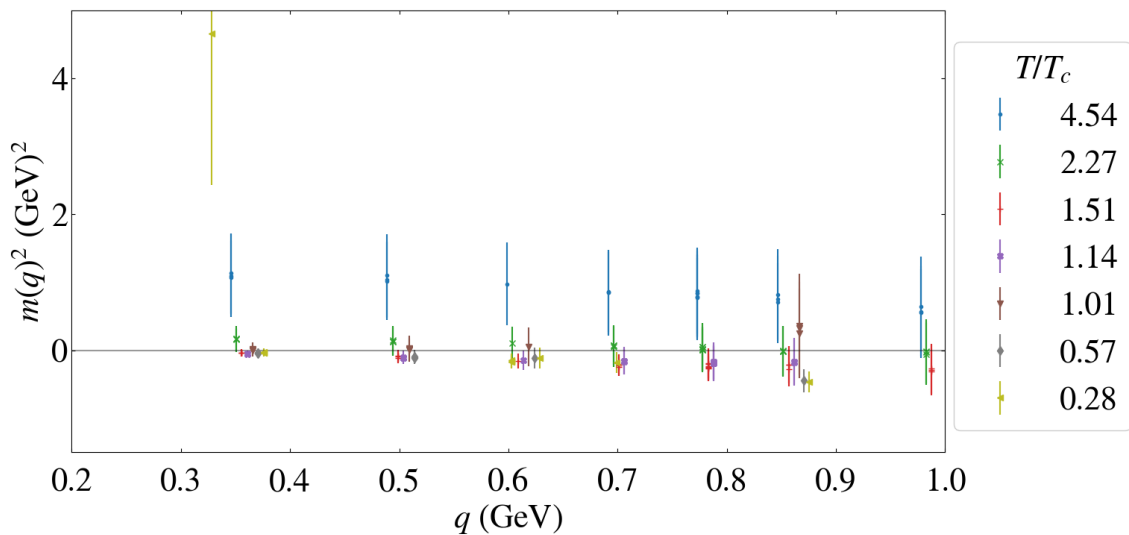
Figure 6.6: Yukawa-inspired mass function, $m^2(q)$, as a function of q for several values of T/T_c. Note that the $T = 0.28\ T_c$ result can probe a finer set of momenta due to the increased temporal extent, N_τ, which is why it can be seen more than once in some clusters of data.

In this chapter we extended our previous work in the Coulomb gauge to include the temporal direction by fixing to the Landau gauge condition, given in Eq. (5.2.2). We discussed the necessary modifications to the gauge-fixing procedure to support anisotropic lattices before motivating power-law fits to the gluon propagator from studies of the propagator in the Dyson-Schwinger formalism. Overall, we find that the Landau gauge gluon propagator suffers from an appreciable degradation in signal as $T \to 0$ due to finite spacing and anisotropy effects. The momentum cutting procedure employed to control the signal harshly reduces the available statistics, but the remaining signal exhibits some degree of thermal modification above T_c in the infrared.

CHAPTER 7

CONCLUSION

The work reported in this thesis may be classified by two research objectives. The first is to explore the bottomonium spectrum at finite temperature spanning the expected deconfinement transition and report any temperature dependence (or lack thereof) for the estimated values of the ground state mass and width.

In Chapter 1 we briefly introduced QCD and discussed how it can be modified to simulate the non-relativistic dynamics of bottomonia (NRQCD) and how it can be regularized and discretised using lattice field theory. In Chapter 2 we motivated bottomonia as a probe for deconfinement, discussed the process of spectral reconstruction and outlined potential techniques for approaching the inverse problem contained therein, highlighting the Backus-Gilbert method as an algebraic solution to the inversion of ill-posed data.

Within the context of the Backus-Gilbert method, we discussed two approaches differing by the definitions of the widths of the averaging functions (the spread and least-squares criteria). We compared them in terms of reconstructive power and computational complexity. We found that the least-squares definition produced narrower and more localised averaging functions, orders of magnitude faster than the spread definition, but at the expense of losing the ability to reconstruct the original correlator and a less-rigorous measure of the resolution width.

We then presented modifications to the Backus-Gilbert method to exploit the Laplacian nature of the NRQCD kernel function via the introduction of a new free parameter (the Laplace 'shift'), which was tested using correlator data corresponding to the η_b, Υ, χ_{b1} and h_b bottomonium. Initial results for the ground state mass and width using smeared quark sources appear promising, but the routine used to remove dependence on the new free parameter is marred by correlations from poor

statistics and does not adequately describe systematic effects due to changing the time-window. It was found that estimates derived from smeared quark sources performed far better than those obtained from local quark source data, which exhibited a non-trivial dependence on the shift and whitening parameters. Furthermore, the systematic error caused by the inclusion of predictions with a poor χ_ν^2 goodness-of-fit remains unaddressed. Overall, no significant dependence of the value of the ground state mass on the temperature was found, whilst the ground state width was found to increase proportionally with temperature. We believe this increase to be a facet of the time extent used to reconstruct the underlying meson spectrum, and our estimates for the width cannot be presented as being consistent with the true underlying state width without a further analysis of the time-window effects.

Our findings suggest that the unshifted form of the Backus-Gilbert method is not well-suited to spectral reconstruction due to the broad sampling functions which it generates for the values of N_τ used in current lattice simulations. However, promise does appear to lie in the Laplace shift transform approach where we have observed an improvement in the resolution of any ground state features from spectra which were previously poorly reconstructed in the unshifted approach, such as the χ_{b1}. It would be particularly interesting to see how this approach applies to other methods which also have a resolution width dependent on the position of the feature within the sampling window (as is the case with the MEM), especially in the context of the recent discussion [67–69] on the relationship between the minimum of the sampling window and the resulting resolution which suggest that there may be a deeper connection with the Laplace shift transform routine.

We concluded the discussion on the Backus-Gilbert method in Chapter 4, where we attempted to characterise the relationship between the error induced by the Laplace shift and the value of the shift parameter. A connection between this relationship and the signal to noise problem predicted by G. Parisi [79] and G.P. Lepage [80] was revealed, where we found that the theoretical upper bound on the Laplace shift is given by the mass of the psuedoscalar meson, regardless of the type of meson channel used for the spectral reconstruction.

Future research directions for the Backus-Gilbert analysis could include a comparative study with the HLT method [60], which is another novel approach to the Backus-Gilbert method which has become increasingly popular in the finite-

temperature community during the course of this work. The HLT method differs by specifying the form of the averaging functions as an input to the method, rather than having them being reconstructed by the kernel function. The advantage is that it does not suffer from the same position-dependent resolution problem as the original Backus-Gilbert approach which the Laplace shift method is based upon. Further work should be made towards understanding the systematic effects of Backus-Gilbert methods with respect to the concerns highlighted in Ref. [78] regarding improper consideration of systematic uncertainty. Comparisons of these two methods could further elucidate the mechanism by which the averaging functions propagate uncertainty through to the reconstructed spectrum, which has long been an unknown problem with Backus-Gilbert [56].

In Chapter 5 we motivated the gluon propagator as a second potential method of probing the deconfinement transition. Results were presented for the gluon propagator in the Coulomb gauge, where we attempted to infer confinement via the measurement of an 'effective gluon mass' in the infrared region using several techniques. It was discovered that the form of the gluon propagator $D(|p|)$ begins to exhibit a noticeable thermal modification around $T = 3\,T_c$ and above, well beyond the expected deconfinement temperature. The effective mass was found to be finite in the limit $|p| \to 0$ below $T \sim 1.5\,T_c$, consistent with confinement, and became increasingly large above $1.5\,T_c$. This postponement in temperature-dependent behaviour has been previously observed in two-color lattice studies [14] and studies into continuum QC$_2$D suggest that this behaviour is due to an emergent chiral-spin symmetry [102]. The appearance of such behaviour in our work incites interest and could potentially suggest that an equivalent mechanism may also occur in SU(3) QCD, but further analysis would be required before such a claim could be reasonably made.

We then extended our study of the gluon propagator by introducing Landau gauge fixing in Chapter 6, where we described the necessary modifications for the gluon propagator calculation to support gauge fields derived from anisotropic ensembles. A method for probing for temperature modification in the infrared was presented in the form of an exponent fit motivated by studies of the propagator using the Dyson-Schwinger formalism. We were able to reproduce similar results for the propagator seen in other studies on the isotropic Landau gauge, but with

a noticeable increase in noise which we believe are finite spacing artefacts brought on from the anisotropy. In conclusion, we determined that the Landau gauge gluon propagator experiences thermal modification above T_c , in contrast with the postponement in thermal effects until $T = 3\,T_c$ observed in the Coulomb gauge. Results obtained for the Dyson-Schwinger exponent were approximately consistent with zero for $T \in [0.5\,T_c, 2.5\,T_c]$ (in contrast to the value of $\kappa \sim 0.5$ observed in the literature) but were finite for $T = 0.3\,T_c, 4.5\,T_c$. The poor values of χ^2_ν goodness-of-fit recorded and the extreme data cutting required to clean the Landau gauge propagator signal suggest that the exponent approach requires further analysis. Measurements of the effective Yukawa mass for the Landau gauge propagator are approximately zero for $T < 1.5\,T_c$ and diverge for $T > 2\,T_c$, suggesting that the gluon propagates like a massless particle in the confined phase, which is in contention with the results predicted by the Coulomb gauge.

As mentioned in Chapter 6, the gluon only represents one half of the dynamics encoded by the gluonic sector of the action – the other being the ghost fields needed to counteract the Gribov copies in the theory. A potential future research direction for the gluon propagator analysis would be to extend the work to include studies of this ghost propagator, which represents the second 'component' of the Gribov-Zwanzinger scenario and is the focus of the Kujo-Ojima confinement scenario. In this case, one should also perform a concurrent study of the Gribov copy effects in a manner similar to that performed in Ref. [91] for the SU(2) theory, which attempted to probe the FMR via a direct calculation of the eigenvalues of the Fadeev-Popov operator. For both the Coulomb and Landau gauge gluon propagator calculations, further study should include larger lattices with a greater range of momentum which are able to more deeply probe the infrared region in an attempt to reconcile the disagreement observed between our Coulomb and Landau gauge results. The Landau gauge propagator in particular could benefit from a focused analysis on finite spacing artefacts in the anisotropic case, along with a study of the effects generated by the breaking of continuous rotational symmetry into hypercubic symmetry (by the lattice) and further breaking to cubic symmetry (by the anisotropy).

Bibliography

[1] M. G. Alford, K. Rajagopal, T. Schaefer and A. Schmitt, *Reviews of Modern Physics* **80** (November, 2008) 1455–1515, [`arXiv:0709.4635`]. 1.1

[2] Particle Data Group, R. L. Workman, V. D. Burkert, V. Crede, E. Klempt, U. Thoma et al., *Progress of Theoretical and Experimental Physics* **2022** (August, 2022) 083C01. 1.6, 2.1, 3.2, 3.2, 3.2

[3] F. D. R. Bonnet, P. O. Bowman, D. B. Leinweber, A. G. Williams and J. M. Zanotti, *Physical Review D* **64** (June, 2001) 034501, [`hep-lat/0101013`]. 5.3, 5.5, 5.5, 6.1, 6.1, 6.3

[4] G. Aarts, C. Allton, J. Glesaaen, S. Hands, B. Jäger, S. Kim et al., *arXiv* (July, 2020) , [`arXiv:2007.04188`]. 3.1, 3.1

[5] G. Aarts, C. Allton, R. Bignell, T. J. Burns, S. C. García-Mascaraque, S. Hands et al., `arXiv:2209.14681`. 3.1, 3.1

[6] P. Petreczky, *Journal of Physics G: Nuclear and Particle Physics* **32** (December, 2006) S293–S300, [`hep-lat/0606007`]. 4.1

[7] D. B. Leinweber, C. Parrinello, J. I. Skullerud and A. G. Williams, *Physical Review D* **58** (July, 1998) 031501, [`hep-lat/9803015`]. 6.1

[8] Y. Chen, B. He, H. Lin and J.-M. Wu, *Modern Physics Letters A* **15** (December, 2000) 2245–2256, [`hep-lat/0008001`].

[9] A. Cucchieri, T. Mendes and A. Taurines, *Physical Review D* **67** (May, 2003) 091502, [`hep-lat/0302022`].

[10] M. Gong, Y. Chen, G. Meng and C. Liu, *Modern Physics Letters A* **24** (August, 2009) 1925–1935, [`arXiv:0811.4635`]. 6.2

[11] H. Suganuma, T. Iritani, A. Yamamoto and H. Iida, "Lattice QCD Study for Gluon Propagator and Gluon Spectral Function." October, 2010, `arXiv:1011.0007`.

[12] Y. Nakagawa, A. Nakamura, T. Saito and H. Toki, *Physical Review D* **83** (June, 2011) 114503, [`arXiv:1105.6185`].

[13] O. Oliveira and P. J. Silva, *Physical Review D* **86** (December, 2012) 114513, [`arXiv:1207.3029`].

[14] H. Vogt, G. Burgio, M. Quandt and H. Reinhardt, "Coulomb gauge on the lattice: From zero to finite temperature." November, 2013, `arXiv:1311.5707`. 5.1, 5.3.1, 5.6, 7

[15] A. C. Aguilar, F. De Soto, M. N. Ferreira, J. Papavassiliou, J. Rodríguez-Quintero and S. Zafeiropoulos, *The European Physical Journal C* **80** (Febuary, 2020) 154, [`arXiv:1912.12086`].

[16] J. Biddle, W. Kamleh and D. Leinweber, "Impact of Dynamical Fermions on the Centre Vortex Gluon Propagator." June, 2022, `arXiv:2206.02320`. 6.1

[17] L. B. Okun, *Leptons and Quarks*. North Holland, 2 ed., 1984. A.1

[18] H. Yukawa, *Proceedings of the Physico-Mathematical Society of Japan. 3rd Series* **17** (1935) 48–57. 1.1

[19] C. M. G. Lattes, H. Muirhead, G. P. S. Occhialini and C. F. Powell, *Nature* **159** (1947) 694–697. 1.1

[20] Y. Ne'eman, *Nuclear Physics* **26** (1961) 222–229. 1.1

[21] M. Gell-Mann, "The eightfold way: A theory of strong interaction symmetry." 1961. , `https://www.osti.gov/biblio/4008239`. 1.1

[22] K. A. Brueckner, *American Physical Society* **86** (1952) 106–109. 1.1

[23] O. W. Greenberg, *Phys. Rev. Lett.* **13** (Nov, 1964) 598–602. 1.1

[24] M. Y. Han and Y. Nambu, *Phys. Rev.* **139** (Aug, 1965) B1006–B1010. 1.1

[25] M. G. Alford, A. Schmitt, K. Rajagopal and T. Schäfer, *Rev. Mod. Phys.* **80** (Nov, 2008) 1455–1515. 1.1

[26] S. Gottlieb, W. Liu, D. Toussaint, R. L. Renken and R. L. Sugar, *Phys. Rev. Lett.* **59** (Nov, 1987) 2247–2250. 1.3

[27] G. Parisi, *Physics Letters B* **131** (1983) 393–395. 1.3

[28] K. G. Wilson, *Physical Review D* **10** (October, 1974) 2445–2459. 1.4

[29] K. Symanzik, *Nuclear Physics B* **226** (Septemer, 1983) 187–204. 1.4

[30] B. Sheikholeslami and R. Wohlert, *Nuclear Physics B* **259** (September, 1985) 572–596. 1.4, 3.1

[31] Montvay, Istvan and Münster, Gernot, *Quantum Fields on a Lattice.* Cambridge Monographs on Mathematical Physics. Cambridge University Press, 1994. 1.4, 1.4, 1.4.1, 1.5

[32] Gattringer, Christof and Lang, Christian B., *Quantum Chromodynamics on the Lattice: An Introductory Presentation*, vol. 788 of *Lecture Notes in Physics.* Springer Berlin, Heidelberg, 1 ed., 2009. 1.4, 1.4.1, 1.5, 3.3

[33] G. Lepage and B. Thacker, *Nuclear Physics B - Proceedings Supplements* **4** (Aprril, 1988) 199–203. 1.6, 1.6

[34] G. P. Lepage, L. Magnea, C. Nakhleh, U. Magnea and K. Hornbostel, *Physical Review D* **46** (1992) 4052–4067. 1.6, 1.6, 1.6

[35] E. Braaten, `hep-ph/9702225`. 1.6

[36] G. Lepage, *Nuclear Physics B - Proceedings Supplements* **26** (1992) 45–56. 1.6

[37] G. Aarts, C. Allton, T. Harris, S. Kim, M. P. Lombardo, S. M. Ryan et al., *Journal of High Energy Physics* **2014** (July, 2014) 97. 1.6, 1.6, 1.6, 2.4, 3.2, 3.6

[38] C. T. H. Davies, K. Hornbostel, A. Langnau, G. P. Lepage, A. Lidsey, C. J. Morningstar et al., `hep-lat/9404012`. 1.6

[39] H. Satz, *Statistical Mechanics of Quarks and Hadrons: Proceedings of an International Symposium Held at the University of Bielefeld, F.R.G., August 24-31, 1980.* North-Holland, 1981. 2.1

[40] H. D. Politzer, *Physical Review Letters* **30** (June, 1973) 1346–1349. 2.1

[41] D. J. Gross and F. Wilczek, *Physical Review Letters* **30** (June, 1973) 1343–1346. 2.1

[42] T. Matsui and H. Satz, *Physics Letters B* **178** (October, 1986) 416–422. 2.1

[43] U. Heinz and M. Jacob, "Evidence for a New State of Matter: An Assessment of the Results from the CERN Lead Beam Programme." Febuary, 2000, `nucl-th/0002042`. 2.1

[44] J. G. McWhirter and E. R. Pike, *Journal of Physics A: Mathematical and General* **11** (September, 1978) 1729–1745. 2.2, 2.3, A.1

[45] A. N. Tikhonov, *Proceedings of the USSR Academy of Sciences* **39** (1943) 195–198. 2.3, 2.6, A.3

[46] S. Shi, L. Wang and K. Zhou, *Computer Physics Communications* **282** (January, 2023) 108547, [`arXiv:2201.02564`]. 2.3

[47] M. Asakawa, Y. Nakahara and T. Hatsuda, *Progress in Particle and Nuclear Physics* **46** (2001) 459–508. 2.4

[48] Y. Burnier and A. Rothkopf, *Physical Review Letters* **111** (October, 2013) 182003, [`arXiv:1307.6106`]. 2.4, 2.9

[49] T. Spriggs, G. Aarts, C. Allton, T. Burns, R. H. D'Arcy, B. Jäger et al., *Proceedings of Science* **LATTICE2021** (2022) 77, [`arXiv:2112.01599`]. 2.4

[50] S. Offler, G. Aarts, C. Allton, B. Jäger, S. Kim, M.-P. Lombardo et al., "Reconstruction of bottomonium spectral functions in thermal QCD using Kernel Ridge Regression." December, 2021, `arXiv:2112.02116`. 2.4

[51] B. J. Conrath, Tech. Rep. 19780004650, Goddard Space Flight Center, Greenbelt, MD, 1977. 2.4, 2.6

[52] D. W. Oldenburg, *IEEE Transactions on Geoscience and Remote Sensing* **GE-22** (November, 1984) 665–674. 2.5

[53] T. B. Yanovskaya, *Geophysical Journal International* **79** (October, 1984) 293–304. 2.6

[54] F. O'Sullivan, *Statistical Science* **1** (1986) 502–518.

[55] G. Nolet and R. Snieder, *Geophysical Journal International* **103** (1990) 565–568. 2.6

[56] T. B. Yanovskaya, Tech. Rep. IC-2003/54, Abdus Salam Intl. Centre, UNESCO, IAEA, Trieste, Italy, 2003. 2.4, 7

[57] G. Backus and F. Gilbert, *Geophysical Journal International* **16** (October, 1968) 169–205. 2.4, 2.5, 2.5, A.2

[58] B. B. Brandt, A. Francis, H. B. Meyer and D. Robaina, *Physical Review D - Particles, Fields, Gravitation and Cosmology* **92** (2015) 1–22. 2.4

[59] T. Harris, H. B. Meyer and D. Robaina, *Proceedings of Science* **Part F1285** (2016) 0–6.

[60] M. Hansen, A. Lupo and N. Tantalo, *Physical Review D* **99** (2019) 94508. 2.5.1, 7

[61] J. Bulava, *Proceedings of Science* **LATTICE2022** (January, 2023) 231, [`arXiv:2301.04072`]. 2.4

[62] R. M. Richardson and G. Zandt, *Inverse Problems in Geophysics GEOS 567*. University of Arizona, University of Arizona, 2003. 2.5, 2.6, A.2

[63] R. L. Parker, *Annual Review of Earth and Planetary Sciences* (1977) 35–64. 2.6

[64] M. Overton, *Numerical Computing with IEEE Floating Point Arithmetic*. Other Titles in Applied Mathematics. Society for Industrial and Applied Mathematics, 2001. 2.6

[65] A. Dresden, *Bulletin of the American Mathematical Society* **26** (1920) 385–396. 2.6

[66] R. Penrose, *Mathematical Proceedings of the Cambridge Philosophical Society* **51** (1955) 406–413. 2.6

[67] A. Rothkopf, *Proceedings of Science* **LATTICE2012** (August, 2012) 100, [`arXiv:1208.5162`]. 2.9, 7

[68] A. Rothkopf, "Laplace shift in the context of other reconstruction methods - private correspondence." 2022. 2.9

[69] B. Page, G. Aarts, C. Allton, B. Jäger, S. Kim, M. P. Lombardo et al., *Proceedings of Science* **LATTICE2021** (December, 2021) , [arXiv:2112.02075]. 2.9, 7

[70] R. G. Edwards, B. Joó and H.-W. Lin, *Physical Review D* **78** (Septemer, 2008) 054501, [arXiv:0803.3960]. 3.1

[71] D. J. Wilson, R. A. Briceno, J. J. Dudek, R. G. Edwards and C. E. Thomas, *Physical Review D* **92** (November, 2015) 094502, [arXiv:1507.02599]. 3.1

[72] D. J. Wilson, R. A. Briceno, J. J. Dudek, R. G. Edwards and C. E. Thomas, *Physical Review Letters* **123** (July, 2019) 042002, [arXiv:1904.03188]. 3.1

[73] S. Güsken, *Nuclear Physics B - Proceedings Supplements* **17** (September, 1990) 361–364. 3.3

[74] R. Bignell and S. Kim, "NRQCD quark source smearing parameters - private correspondence." 2024. 3.3

[75] G. Aarts, S. Kim, M. P. Lombardo, M. B. Oktay, S. M. Ryan, D. K. Sinclair et al., *Physical Review Letters* **106** (2010) 61602. 3.6

[76] T. Harris, S. M. Ryan, G. Aarts, C. Allton, S. Kim, M. P. Lombardo et al., "Bottomonium spectrum at finite temperature." November, 2013, arXiv:1311.3208. 3.6

[77] K. Suzuki, P. Gubler, K. Morita and M. Oka, *Nuclear Physics A* **897** (January, 2013) 28–41, [arXiv:1204.1173]. 3.6

[78] S. Kim, P. Petreczky and A. Rothkopf, *Journal of High Energy Physics* **2018** (November, 2018) 88, [arXiv:1808.08781]. 3.6, 7

[79] G. Parisi, *Physics Reports* **103** (January, 1984) 203–211. 4.1, 7

[80] G. P. Lepage, *Newman Laboritories of Nuclear Studies* (1989) . 4.1, 7

[81] M. L. Wagman and M. J. Savage, *Physical Review D* **96** (November, 2016) . 4.1

[82] M. L. Wagman, *EPJ Web of Conferences* **175** (2018) 5003. 4.1, 4.1

[83] M. Fierz, *Zeitschrift für Physik* **104** (July, 1937) 553–565. 4.1, A.4

[84] G. Kanwar, "Machine Learning and Variational Algorithms for Lattice Field Theory." June, 2021, `arXiv:2106.01975`. 4.1

[85] W. Detmold, G. Kanwar, Y. Lin, P. E. Shanahan and M. L. Wagman, "Signal-to-noise improvement through neural network contour deformations for 3D $SU(2)$ lattice gauge theory." September, 2023, `arXiv:2309.00600`. 4.1

[86] T. Kugo and I. Ojima, *Progress of Theoretical Physics Supplement* **66** (1979) 1–130. 5.2

[87] V. Gribov, *Nuclear Physics B* **139** (June, 1978) 1–19. 5.2, 5.2, 5.4

[88] D. Zwanziger, *Nuclear Physics B* **485** (Febuary, 1997) 185–240. 5.2

[89] R. Alkofer and L. von Smekal, *Physics Reports* **353** (November, 2001) 281–465, [`hep-ph/0007355`]. 5.2

[90] L. Faddeev and V. Popov, *Physics Letters B* **25** (July, 1967) 29–30. 5.2

[91] H. A. Vogt, *Strongly Coupled Theories in Lattice Coulomb Gauge.* PhD thesis, Universität Tübingen, Septemer, 2017. 10.15496/PUBLIKATION-19214. 5.2, 5.3.1, 6, 7

[92] D. Zwanziger, *Physics Letters B* **114** (1982) 337–339. 5.2, A.6

[93] T. Mendes and A. Cucchieri, "Systematic Effects at Criticality for the SU(2)-Landau-Gauge Gluon Propagator." January, 2014, `arXiv:1401.6908`. 5.2

[94] D. Dudal, J. Gracey, S. P. Sorella, N. Vandersickel and H. Verschelde, *Physical Review D* **78** (September, 2008) 065047, [`arXiv:0806.4348`]. 5.2

[95] G. Dell'Antonio and D. Zwanziger, *Communications in Mathematical Physics* **138** (1991) 291–299. 5.2, A.6

[96] J. Marques, "Gaugefix-coulomb." 2023. `https://github.com/jesuel-marques/GaugeFix-Coulomb`. 5.2, B.3

[97] J. Marques, G. Kalusche, T. Mendes, P. Silva, J.-I. Skullerud and O. Oliveira, *Proceedings of Science* (January, 2023) 280, [`arXiv:2301.10607`]. 5.2

[98] G. Burgio, M. Quandt and H. Reinhardt, *Physical Review Letters* **102** (January, 2009) 032002, [`arXiv:0807.3291`]. 5.3.1, 5.3.1, 5.3.1, 6

[99] F. D. R. Bonnet, P. O. Bowman, D. B. Leinweber and A. G. Williams, *Physical Review D* **62** (July, 2000) 051501, [`hep-lat/0002020`]. 5.6

[100] G. S. Bali, J. Fingberg, U. M. Heller, F. Karsch and K. Schilling, *Physical Review Letters* **71** (November, 1993) 3059–3062, [`hep-lat/9306024`]. 5.6, 6

[101] G. Boyd, J. Engels, F. Karsch, E. Laermann, C. Legeland, M. Luetgemeier et al., *Nuclear Physics B* **469** (June, 1996) 419–444, [`hep-lat/9602007`]. 5.6, 6

[102] L. Y. Glozman, `arXiv:1907.01820`. 5.6, 7

[103] L. von Smekal, A. Hauck and R. Alkofer, *Physical Review Letters* **79** (November, 1997) 3591–3594, [`hep-ph/9705242`]. 6.2, 6.2

[104] G. Aarts, C. Allton, J. Glesaaen, S. Hands, A. Nikolaev, B. Jäger et al., *Proceedings of Science* **363** (2019) 0–6.

[105] G. Aarts and J. M. M. Resco, *Journal of High Energy Physics* **6** (2002) 1319–1336.

[106] G. Aarts, C. Allton, S. Kim, M. P. Lombardo, S. M. Ryan and J. I. Skullerud, *Proceedings of Science* **29-July-20** (2013) .

[107] G. Aarts, C. Allton, S. Kim, M. P. Lombardo, M. B. Oktay, S. M. Ryan et al., *Journal of High Energy Physics* **2011** (November, 2011) 103.

[108] S. Aoki, Y. Kuramashi and S.-i. Tominaga, *Progress of Theoretical Physics* **109** (March, 2003) 383–414.

[109] R. Aouane, F. Burger, E.-M. Ilgenfritz, M. Muller-Preussker and A. Sternbeck, *Physical Review D* **87** (June, 2013) 114502, [`arXiv:1212.1102`].

[110] S. Bacchio, C. Stylianou, A. Angeli, R. Bignell and B. Page, "Lyncs-API/lyncs.io, I/O functions for Python and LQCD file formats." 2023. https://github.com/Lyncs-API/lyncs.io. B.3

[111] P. Bevington, *Data Reduction and Error Analysis for the Physical Sciences.* McGraw-Hill, 1969. B.1

[112] N. Brambilla, A. Pineda, J. Soto and A. Vairo, *Reviews of Modern Physics* **77** (December, 2005) 1423–1496, [hep-ph/0410047].

[113] G. Burgers, F. Karsch, A. Nakamura and I. Stamatescu, *Nuclear Physics B* **304** (January, 1988) 587–600.

[114] G. Burgio, M. Quandt and H. Reinhardt, *Physical Review D* **86** (August, 2012) 045029, [arXiv:1205.5674].

[115] A. Cucchieri and T. Mendes, *Computer Physics Communications* **154** (July, 2003) 1–48, [hep-lat/0301019].

[116] H. T. Ding, A. Francis, O. Kaczmarek, H. Satz, F. Karsch and W. Söldner, *Proceedings of Science* **105** (2010) .

[117] R. J. Dowdall, B. Colquhoun, J. O. Daldrop, C. T. H. Davies, I. D. Kendall, E. Follana et al., *Physical Review D* **85** (March, 2012) 054509, [arXiv:1110.6887].

[118] J. Fingberg, *Physics Letters B* **424** (Aprril, 1998) 343–354, [hep-lat/9707012].

[119] K. Fukushima and T. Hatsuda, *Reports on Progress in Physics* **74** (January, 2011) 014001, [arXiv:1005.4814].

[120] J. Gamboa and S. L. a. L. Vergara, *arXiv* (2000) 1–3, [hep-ph/0007089].

[121] F. Gilbert and G. Backus, *Philosophical Transactions of the Royal Society of London. Series A, Mathematical and Physical Sciences* **266** (1970) 123–192.

[122] L. Giusti, M. L. Paciello, C. Parrinello, S. Petrarca and B. Taglienti, *International Journal of Modern Physics A* **16** (August, 2001) 3487–3534, [hep-lat/0104012].

[123] J. Greensite, S. Olejnik and D. Zwanziger, *Journal of High Energy Physics* **2005** (May, 2005) 070–070, [`hep-lat/0407032`].

[124] Greiner, Walter, Schramm, Stefan and Stein, Eckart, *Quantum Chromodynamics.* Springer, 2 ed., 2002.

[125] F. Halzen and A. Martin, *QUARK & LEPTONS: AN INTRODUCTORY COURSE IN MODERN PARTICLE PHYSICS.* Wiley Student Edition. Wiley India Pvt. Limited, 2008.

[126] P. C. Hansen, *Inverse Problems* **10** (1994) 895–904.

[127] J. Heffner, H. Reinhardt and D. R. Campagnari, *Physical Review D* **85** (June, 2012) 125029, [`arXiv:1206.3936`].

[128] U. M. Heller, . F. Karsch and J. Rank, *Physics Letters B* **355** (August, 1995) 511–517, [`hep-lat/9505016`].

[129] A. Hulsebos, *Nuclear Physics B - Proceedings Supplements* **30** (March, 1993) 539–542.

[130] K.-H. Ilk, *Proc. Int. Symp. Figure and Dynamics of the Earth, Moon, and Planets, Prague* (January, 1987) 365.

[131] T. R. Klassen, *Nuclear Physics B* **533** (November, 1998) 557–575, [`hep-lat/9803010`].

[132] M. Laine and A. Vuorinen, *Basics of Thermal Field Theory*, vol. 925. 2016.

[133] D. Leinweber, C. Parrinello, J. Skullerud and A. Williams, *Nuclear Physics B - Proceedings Supplements* **73** (March, 1999) 629–631.

[134] D. B. Leinweber, C. Parrinello, J. I. Skullerud and A. G. Williams, *Nuclear Physics B - Proceedings Supplements* **73** (March, 1999) 626–628, [`hep-lat/9809030`].

[135] P. Lepage, C. Gohlke and D. Hackett, "Gplepage/gvar: Gvar version 11.11.13." August, 2023. , `https://github.com/gplepage/gvar`. B.3

[136] C. Lerche and L. von Smekal, *Physical Review D* **65** (June, 2002) 125006, [`hep-ph/0202194`].

[137] J. Mandula and M. Ogilvie, *Physics Letters B* **201** (January, 1988) 117–122.

[138] H. Mellin, *Zur Theorie Zweier Allgemeinen Klassen Bestimmter Integrale.*
No. no. 2 in Suomen Tiedeseura. Acta Societatis Scientiarum Fennicæ. T. 22.
1897. A.1, A.1

[139] C. A. Meyer and Y. Van Haarlem, *Physical Review C* **82** (August, 2010)
025208, [`arXiv:1004.5516`].

[140] Y. Nakagawa, A. Voigt, E.-M. Ilgenfritz, M. Müller-Preussker, A. Nakamura,
T. Saito et al., *Physical Review D* **79** (June, 2009) 114504,
[`arXiv:0902.4321`].

[141] Y. Nakagawa, A. Nakamura, T. Saito and H. Toki, `arXiv:0911.2550`.

[142] H. Nakajima, S. Furui and A. Yamaguchi, *Nuclear Physics B - Proceedings
Supplements* **94** (March, 2001) 558–561.

[143] V. Paiva, P. J. Silva and O. Oliveira, "Deconfinement, Center Symmetry and
the Ghost Propagator in Landau Gauge Pure SU(3) Yang-Mills Theory."
July, 2023, `arXiv:2307.08662`.

[144] A. SaiToh, *Computer Physics Communications* **184** (March, 2013) . B.3

[145] M. Schröck and H. Vogt, *Computer Physics Communications* **184** (August,
2013) 1907–1919, [`arXiv:1212.5221`].

[146] H.-T. Shu, H.-T. Ding, O. Kaczmarek, S. Mukherjee and H. Ohno,
`arXiv:1510.02901`.

[147] P. J. Silva, O. Oliveira, D. Dudal, P. Bicudo and N. Cardoso, *Few-Body
Systems* **58** (May, 2017) 127, [`arXiv:1611.04966`].

[148] P. J. Silva, O. Oliveira, D. Dudal, P. Bicudo and N. Cardoso, "Many faces of
the Landau gauge gluon propagator at zero and finite temperature:
Positivity violation, spectral density and mass scales." January, 2014,
`arXiv:1401.1554`.

[149] J. Soto, *European Physical Journal A* **31** (2007) 705–710.

[150] G. 'T Hooft, *Nuclear Physics B* **138** (June, 1978) 1–25.

[151] A. N. Tikhonov, *Proceedings of the USSR Academy of Sciences* **151** (1963) 501–504.

[152] R. A. Tripolt, P. Gubler, M. Ulybyshev and L. von Smekal, *Computer Physics Communications* **237** (2019) 129–142.

Appendix A

Mathematical Appendix

A.1 Deriving the eigenvalues of the Laplace transform

The following is a derivation of the eigenvalues of the Laplace transform, based on the derivation given in Ref. [44]. Consider a function of the form

$$G(\tau) = \int_0^\infty K(\tau, \omega)\rho(\omega). \tag{A.1.1}$$

The eigenproblem associated with Eq. (A.1.1) is given by

$$\int_0^\infty K(\tau, \omega)\phi_s(\omega)d\omega = \lambda_s\phi_s(\tau), \tag{A.1.2}$$

where ϕ_s are the eigenfunctions of the system. Let us now assume that the eigenfunctions take the form

$$\phi_s(\omega) = A\omega^{-s} + B\omega^{s-1}, \tag{A.1.3}$$

(with $A, B, s \in \mathbb{C}$) where the insertion of the above into the original problem Eq. (A.1.1) yields

$$G_s(\tau) = \int_0^\infty K(\tau, \omega)\left[A\omega^{-s} + B\omega^{s-1}\right]d\omega. \tag{A.1.4}$$

Substituting $z = \omega\tau$ allows us to express the kernel as a single-variable function $K(z)$:

$$G_s(\tau) = \int_0^\infty K(z)\left[A\left(\frac{z}{\tau}\right)^{-s} + B\left(\frac{z}{\tau}\right)^{s-1}\right]\frac{dz}{\tau}. \tag{A.1.5}$$

The integral over $K(z)$ and z is a type of Mellin transform [138], $\mathcal{M}\{\cdot\}$, which in the case of a Laplacian kernel $K(x)$ gives the Γ function,

$$\mathcal{M}\left\{K(x)\right\}(s) = \int_0^\infty x^{s-1} K(x) dx, \tag{A.1.6}$$

$$\Gamma(s) = \int_0^\infty x^{s-1} e^{-x} dx, \tag{A.1.7}$$

where we demand that $\mathrm{Re}(s) > 0$ for convergence, but further restrict to $0 < \mathrm{Re}(s) < 1$, to also ensure the proper convergence of $\Gamma(1-s)$. Eq. (A.1.5) in terms of the continuous label s is given by:

$$G_s(\tau) = A\Gamma(1-s)\tau^{s-1} + B\Gamma(s)\tau^{-s}, \tag{A.1.8}$$

where we are free to make a choice of constants A, B:

$$A = \sqrt{\Gamma(s)}, \quad \text{and} \quad B = \pm\sqrt{\Gamma(1-s)}, \tag{A.1.9}$$

such that $G_s(\tau)$ becomes

$$G_s(\tau) = \pm\sqrt{\Gamma(s)\Gamma(1-s)}\ \phi_s(\tau). \tag{A.1.10}$$

The eigenvectors ϕ_s are given by

$$\phi_s^\pm(\omega) = \sqrt{\Gamma(s)}\omega^{-s} \pm \sqrt{\Gamma(1-s)}\omega^{s-1}, \tag{A.1.11}$$

and the corresponding eigenvalues are

$$\lambda_s^\pm = \pm\sqrt{\Gamma(s)\Gamma(1-s)}. \tag{A.1.12}$$

By the Mellin inversion theorem [138], the inverse of $\Gamma(s)$, defined by

$$e^{-x} = \mathcal{M}^{-1}\left\{\Gamma(s)\right\} = \frac{1}{2\pi i}\int_{c-i\infty}^{c+i\infty} x^{-s}\Gamma(s) ds, \tag{A.1.13}$$

converges absolutely for any real value $a < c < b$ provided that $\Gamma(s)$ is analytic in the fundamental strip $a < \mathrm{Re}(s) < b$ and $\Gamma(s)$ tends uniformly to zero as $\mathrm{Im}(s) \to \pm\infty$. Thus, we are free to consider solutions which lie on the line $s = \frac{1}{2} + i\nu$, where $\nu \in \mathbb{R}$,

which yields

$$\lambda_\nu^\pm = \pm \left| \Gamma \left(\frac{1}{2} + i\nu \right) \right|, \tag{A.1.14}$$

$$|\lambda_\nu^\pm|^2 = \left| \Gamma \left(\frac{1}{2} + i\nu \right) \right|^2 \equiv \frac{\pi}{\cosh(\pi\nu)}. \tag{A.1.15}$$

It is now evident that as the continuous variable $\nu \to \infty$ the eigenvalues $\lambda_\nu^\pm$ become arbitrarily small, thus making the problem ill-posed.

A.2 Minimisation of the Backus-Gilbert Spread Function

The spread criterion [57] is defined in Eq. (2.5.7) as

$$W(\omega_0) = 12 \int_a^b (\omega - \omega_0)^2 A(\omega, \omega_0)^2 d\omega, \tag{A.2.1}$$

where the factor of 12 facilitates the geometric interpretation of the width [62]. The value of $W(\omega_0)$ calculated from Eq. (A.2.1) represents the box-car estimate of the resolution (i.e., the error in ω at ω_0 is $\pm W(\omega_0)/2$). The factor of $(\omega - \omega_0)^2$ is the localisation factor and is often replaced by functions which serve a similar purpose in the literature.

Minimising Eq. (A.2.1) with respect to the averaging coefficients c_τ,

$$\partial_{c_{\tau'}} W(\omega_0) = 24 \sum_\tau \int_a^b (\omega - \omega_0)^2 c_\tau K(\tau, \omega) K(\tau', \omega) d\omega = 0, \tag{A.2.2}$$

reveals the trivial solution $c_\tau(\omega_0) = 0, \quad \forall \tau$. Demanding that the minimisation be subject to the constraint that $\int A(\omega, \omega_0) = 1$ allows us to rewrite Eq. (A.2.1) using a Lagrange multiplier:

$$\widetilde{W}(\omega_0, \lambda) = 12 \int_a^b (\omega - \omega_0)^2 A(\omega, \omega_0)^2 d\omega + \lambda \left[\int_a^b A(\omega, \omega_0) d\omega - 1 \right]. \tag{A.2.3}$$

Minimisation with respect to $c_\tau(\omega_0)$ then gives

$$\partial_{c_{\tau'}} \widetilde{W}(\omega_0, \lambda) = 24 \sum_\tau \int_a^b (\omega - \omega_0)^2 c_\tau K(\tau, \omega) K(\tau', \omega) d\omega + \lambda \int_a^b K(\tau', \omega) d\omega = 0. \tag{A.2.4}$$

Equation (A.2.4) together with the unimodularity constraint may be expressed in

matrix form by defining the kernel width matrix, $\mathcal{K}_{\tau\tau'}$,

$$\mathcal{K}_{\tau\tau'}(\omega_0) = 12 \int_a^b (\omega - \omega_0)^2 K(\tau, \omega) K(\tau', \omega) d\omega, \qquad (A.2.5)$$

and the kernel constraint vector, $\mathcal{C}_\tau$,

$$\mathcal{C}_\tau = \int_a^b K(\tau, \omega) d\omega, \qquad (A.2.6)$$

such that we may write Eq. (A.2.4) in the form of a matrix-vector product

$$\begin{pmatrix} 2\mathcal{K} & \mathcal{C} \\ \mathcal{C}^\mathsf{T} & 0 \end{pmatrix} \cdot \begin{pmatrix} c(\omega_0) \\ \lambda \end{pmatrix} = \begin{pmatrix} \mathbf{0} \\ 1 \end{pmatrix}, \qquad (A.2.7)$$

encodes both the width minimsation and the unimodularity constraint of Eq. (A.2.3). This system of equations can then be directly solved for the Lagrange multiplier λ

$$\lambda = -\frac{2}{\mathcal{C}^\mathsf{T} \mathcal{K}^{-1} \mathcal{C}}, \qquad (A.2.8)$$

and the Backus-Gilbert averaging coefficients, given by

$$c_\tau(\omega_0) = \frac{\mathcal{K}^{-1} \mathcal{C}}{\mathcal{C}^\mathsf{T} \mathcal{K}^{-1} \mathcal{C}}. \qquad (A.2.9)$$

The values of $c_\tau(\omega_0)$ associated with the spread function result in averaging functions that are relatively broad with small, smoothly varying side lobes. One drawback of the spread function is that the width matrix $\mathcal{K}$ explicitly depends on ω_0 and so must be regenerated for each point in ω-space which is sampled. This represents an intense computational burden and is often the cause of the spread function being overlooked when a high sampling rate is needed. This issue may be remedied by shifting the localisation dependence to a lower-dimension object (i.e. a vector).

A.3   Tikhonov Matrix Regularisation

Consider some matrix A which acts upon some unknown vector x to give b:

$$Ax = b. \qquad (A.3.1)$$

If b is known, we can determine x via a least-squares minimisation of the residuals r, where

$$r = ||Ax - b||^2 \qquad (A.3.2)$$

which is trivially minimised when $x = A^{-1}b$. Tikhonov regularization [45] acts to give preference to a particular estimate $\hat{x}$ by introducing a regularization term to the residuals:

$$r_\Gamma = ||Ax - b||^2 + ||\Gamma x||^2, \qquad (A.3.3)$$

where Γ is known as a Tikhonov matrix. The regularised estimate, $\hat{x}$, is then given by

$$\hat{x} = (A^T A + \Gamma^T \Gamma)^{-1} A^T b. \qquad (A.3.4)$$

Consider the case where $\Gamma = \alpha \mathbb{1}$. Using the singular value decomposition of A,

$$A = U\Sigma V^T, \qquad (A.3.5)$$

we may write Eq. (A.3.4) as

$$\hat{x} = (V\Sigma^T U^T U\Sigma V^T)V\Sigma^T U^T b. \qquad (A.3.6)$$

Introducing the Tikhonov matrix, $\Gamma = \alpha \mathbb{1}$, then yields

$$\hat{x} = (V\Sigma^T\Sigma V^T + \alpha VV^T)^{-1}V\Sigma^T U^T b \qquad (A.3.7)$$

$$= V(\Sigma^T\Sigma + \alpha^2 \mathbb{1})^{-1}V^T V\Sigma^T U^T b \qquad (A.3.8)$$

$$= VDU^T b, \qquad (A.3.9)$$

where we have defined

$$D = (\Sigma^T\Sigma + \alpha^2 \mathbb{1})^{-1}\Sigma^T. \qquad (A.3.10)$$

The diagonal elements of D are given by

$$D_{ii} = \frac{\sigma_i}{\sigma_i^2 + \alpha^2}. \qquad (A.3.11)$$

The whitening procedure adopted by our approach uses a similar style of whitening where the Tikhonov matrix is directly applied to the target matrix before inversion, leading to an increase in the inverse singular values in a similar manner to

Table A.1: Table of matrix contractions corresponding to each current component in the Fierz identity, for a given Γ_M [17].

	Γ_M				
	$\mathbb{1}$	γ_ρ	γ_5	$\gamma_\rho\gamma_5$	$\sigma_{\rho\lambda}/\sqrt{2}$
$\Gamma_M\Gamma_M$	$\mathbb{1}$	$4\cdot\mathbb{1}$	$\mathbb{1}$	$-4\cdot\mathbb{1}$	$-6\cdot\mathbb{1}$
$\Gamma_M\gamma_\mu\Gamma_M$	γ_μ	$-2\gamma_\mu$	$-\gamma_\mu$	$-2\gamma_\mu$	0
$\Gamma_M\gamma_5\Gamma_M$	γ_5	$-4\gamma_5$	γ_5	$-4\gamma_5$	$-6\gamma_5$
$\Gamma_M\gamma_\mu\gamma_5\Gamma_M$	$\gamma_\mu\gamma_5$	$2\gamma_\mu\gamma_5$	$-\gamma_\mu\gamma_5$	$2\gamma_\mu\gamma_5$	0
$\Gamma_M\sigma_{\mu\nu}\Gamma_M$	$\sigma_{\mu\nu}$	0	$\sigma_{\mu\nu}$	0	$-2\sigma_{\mu\nu}$

Eq. (A.3.11).

A.4 General Fierz Identities

The Fierz identity [83] allows one to rewrite the bilinears of the product of two spinors as a linear combination of the products of the bilinears of the individual spinors. The general decomposition of some bilinear $\psi\bar{\chi}$ in the space of Dirac matrices is given by:

$$\psi\bar{\chi} = \frac{1}{4}\left[(\bar{\chi}\psi)\mathbb{1} + (\bar{\chi}\gamma_\mu\psi)\gamma_\mu - \frac{1}{2}(\bar{\chi}\sigma_{\mu\nu}\psi)\sigma_{\mu\nu} - (\bar{\chi}\gamma_\mu\gamma_5\psi)\gamma_\mu\gamma_5 + (\bar{\chi}\gamma_5\psi)\gamma_5\right]. \quad \text{(A.4.1)}$$

From Eq. (A.4.1) one can calculate the scalar contraction of the product of any two general bilinears by pre and post-multiplying by the relevant gamma matrix-spinor pairs. Consider some particle M which has the corresponding interpolating matrix $\Gamma_M \in [\mathbb{1}, \gamma_\rho, \gamma_5, \gamma_\rho\gamma_5, \sigma_{\rho\lambda}]$, then we may write the product of its bilinears as

$$(\bar{\psi}\Gamma_M\psi)(\bar{\chi}\Gamma_M\chi) = \frac{1}{4}\Big[(\bar{\chi}\psi)(\bar{\psi}\Gamma_M^2\chi) + (\bar{\chi}\gamma_\mu\psi)(\bar{\psi}\Gamma_M\gamma_\mu\Gamma_M\chi)$$
$$- \frac{1}{2}(\bar{\chi}\sigma_{\mu\nu}\psi)(\bar{\psi}\Gamma_M\sigma_{\mu\nu}\Gamma_M\chi) - (\bar{\chi}\gamma_\mu\gamma_5\psi)(\bar{\psi}\Gamma_M\gamma_\mu\gamma_5\Gamma_M\chi)$$
$$+ (\bar{\chi}\gamma_5\psi)(\bar{\psi}\Gamma_M\gamma_5\Gamma_M\chi)\Big]. \quad \text{(A.4.2)}$$

The gamma matrix algebra in the second factor of each term may be simplified by using the contractions in Table A.1 for some Γ_M. Inserting the relevant factors from Table 4.2 into Eq. (A.4.2) then produces the correct Fierz coefficients given in Table 4.2.

A.5   THE FADEEV-POPOV PROCEDURE

For simplicity, consider the partition function associated with the Yang-Mills Lagrangian, given by

$$\mathcal{Z}_{\text{YM}} = \int \mathcal{D}A_\mu e^{iS_{\text{YM}}[A_\mu]}. \tag{A.5.1}$$

Each gauge field, A_μ, is a member of a gauge-orbit comprised of fields equivalent under a gauge transformation. We can then break the path integral over the fields, A_μ, into an integral over each gauge orbit using

$$\mathcal{Z}_{\text{YM}} = \int \mathcal{D}\Omega \mathcal{D}A_\mu^\Omega, e^{iS_{\text{YM}}[A_\mu^\Omega]} \tag{A.5.2}$$

where A_μ^Ω is a singular member of the gauge orbit. Using the fact that the action is invariant under a gauge transformation, we can rewrite the partition function as

$$\mathcal{Z}_{\text{YM}} = \int \mathcal{D}A_\mu^\Omega e^{iS_{\text{YM}}[A_\mu^\Omega]} \int \mathcal{D}\Omega, \tag{A.5.3}$$

where we can now see that $\int \mathcal{D}\Omega$ is precisely the factor by which the partition function is over-counted. Given some gauge condition $F[A_\mu]$, Fadeev and Popov proposed the insertion of the unitary quantity

$$\mathbb{1} = \det\left(\frac{\delta F[A_\mu^\Omega]}{\delta \Omega}\right) \int \mathcal{D}\Omega \delta F[A_\mu^\Omega], \tag{A.5.4}$$

into Eq. (A.5.3) such that it becomes

$$\mathcal{Z}_{\text{YM}} = \int \mathcal{D}A_\mu^\Omega \det\left(\frac{\delta F[A_\mu^\Omega]}{\delta \Omega}\right) \int \mathcal{D}\Omega \delta F[A_\mu^\Omega] e^{iS_{\text{YM}}[A_\mu^\Omega]}. \tag{A.5.5}$$

The partition function $\mathcal{Z}_{YM}$ is now given by an integration over physically distinct fields, where gauge-equivalent fields along the gauge orbit are removed by the $\delta F[A_\mu^\Omega]$ term.

A.6   DERIVING THE GAUGE FUNCTIONAL

It is a long-established [92, 95] fact that the isotropic Coulomb and Landau gauge conditions may be fixed on the lattice via the maximisation of the gauge functional:

$$W[A] = \sum_\mu \int d^4x \, \text{Tr}[A_\mu^2]. \tag{A.6.1}$$

Consider the application of an infinitesimal gauge transformation, which on the lattice is represented via

$$U_\mu(x) \to \Omega(x)U_\mu(x)\Omega^\dagger(x+\mu), \tag{A.6.2}$$

where $\Omega(x) = e^{i\varepsilon H(x)}$, with ε small and $H(x)$ traceless and Hermitian. Under Eq. (A.6.2) the A_μ fields transform as

$$A_\mu(x) \to A_\mu(x) + \varepsilon \left(i[H(x), A_\mu(x)] - \partial_\mu H(x)\right), \tag{A.6.3}$$

correct to $\mathcal{O}(\varepsilon^2)$. Inserting the above into the gauge functional Eq. (A.6.1) yields

$$W[A] \to \sum_\mu \int d^4x \, \text{Tr}\left[A_\mu^2 + 2i\varepsilon A_\mu[H, A_\mu] - 2\varepsilon A_\mu\partial_\mu H\right] + \mathcal{O}(\varepsilon^2) \tag{A.6.4}$$

$$\to W[A] - 2\varepsilon \sum_\mu \int d^4x \, \text{Tr}\left[A_\mu\partial_\mu H\right] + \mathcal{O}(\varepsilon^2), \tag{A.6.5}$$

where we have used $\text{Tr}[A+B] = \text{Tr}[A] + \text{Tr}[B]$ in Eq. (A.6.4) to separate each term in A_μ and have used periodicity of the trace to remove the commutator. Integrating Eq. (A.6.5) by-parts allows us to write

$$W[A] \to W[A] - 2\varepsilon \sum_\mu \left([AH]_{-\infty}^{\infty} - \int d^4x \, \text{Tr}[(\partial_\mu A_\mu)H]\right) + \mathcal{O}\varepsilon^2 \tag{A.6.6}$$

$$\to W[A] + 2\varepsilon \sum_\mu \int d^4x \, \text{Tr}[(\partial_\mu A_\mu)H] + \mathcal{O}(\varepsilon^2) \tag{A.6.7}$$

where we have explicitly assumed that $H(x)$ vanishes in the limit $x \to \infty$. If the transform in Eq. (A.6.2) maximises the functional $W[A]$, then we must have

$$\sum_\mu \int d^4x \, \text{Tr}[(\partial_\mu A_\mu)H] = 0. \tag{A.6.8}$$

Since the above is valid for any arbitrary (traceless Hermitian) choice of $H(x)$, we may set $H(x) = \mathbb{1}$ and thus we find that Eq. (A.6.1) corresponds to a minimisation of the Landau gauge condition,

$$\partial_\mu A_\mu = 0, \tag{A.6.9}$$

across the lattice. We note that the above prescription holds for the Coulomb gauge condition $\partial_i A_i = 0$ via the simple modification $\mu = \{1, 2, 3, 4\} \to i = \{1, 2, 3\}$.

Appendix B

Technical Appendix

B.1 Goodness-of-Fit Determination

In our analysis we make use of the reduced chi-square statistic as a means of determining the goodness-of-fit associated with a particular fitting routine. The reduced chi-square statistic is defined as

$$\chi_\nu^2 = \frac{\chi^2}{\nu}, \tag{B.1.1}$$

with ν the number of degrees of freedom for the model and χ^2 the weighted sum of squared deviations, given by

$$\chi^2 = \sum_i \frac{(y_i^{\text{obs}} - y_i^{\text{fit}})^2}{\sigma_i^2}, \tag{B.1.2}$$

where y_i^{obs} and y_i^{fit} are the observed and modelled data values respectively, and σ_i the standard deviation of the observed data. In the case where there is appreciable correlation between observations, we use the correlated chi-square statistic defined by

$$\chi_\nu^2 = \frac{\boldsymbol{r}^T \boldsymbol{W} \boldsymbol{r}}{\nu}, \tag{B.1.3}$$

where $r_i = (y_i^{\text{obs}} - y_i^{\text{fit}})$ and $\boldsymbol{W}$ is the weight matrix, equal to the inverse of the covariance matrix of y_{obs}.

Generally, $\chi_\nu^2 \gg 1$ signals a poor fit of the model to the underlying data, whereas $\chi_\nu^2 < 1$ signals overfitting or potential overestimation of the error of the observations. Fits with $\chi_\nu^2 \sim 1$ are considered a fair fit to the underlying data and its error[111].

B.2 Operation Counting for the Backus-Gilbert Method

The least-squares criterion only requires a single matrix inversion to calculate a complete set of coefficients c_τ, whereas the spread criterion requires N_ω inversions

where N_ω is the number of sampling points ω_0. To perform the inverse, the singular value decomposition (SVD) is first calculated at a cost of $\mathcal{O}(N^3)$ operations.

Figure B.1 compares the time required to calculate one complete set of $N_\omega \times N_\tau$ coefficients for both the least-squares (Eq. (2.5.8)) and spread (Eq. (2.5.7)) criteria. The ratio of the two curves approaches the value of N_ω as $N_\tau \to \infty$.
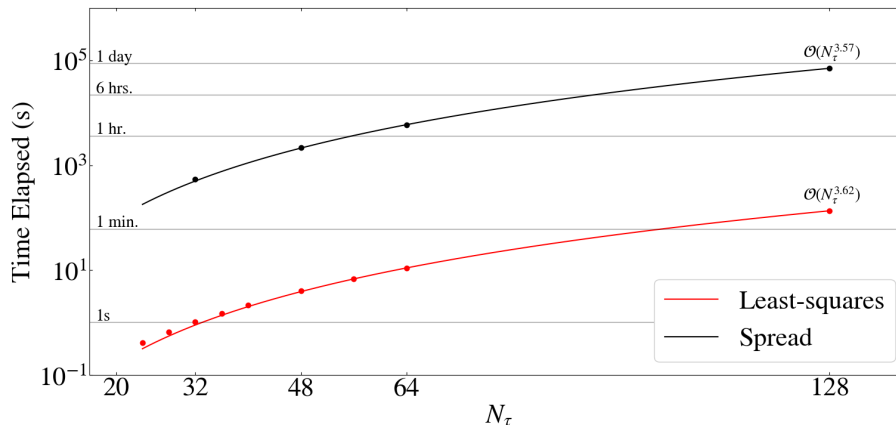

Figure B.1: Comparison of time to calculate $N_\omega \times N_\tau = 500N_\tau$ coefficients for the least-squares versus spread criteria. The horizontal lines represent some example times for reference.

B.3 Use of open-source libraries

This work makes use of several open-source libraries. Along with the standard Python libraries which are commonplace in numerical analysis (`numpy`, `pandas`, and `matplotlib`) we also use several external libraries, details of which we shall outline below.

The code created to generate the Backus-Gilbert coefficients depends largely on two open-source software libraries: GNU MP and MPFR, and ZKCM [144]. GNU MP (Multi-Precision) and MPFR (Multi-Precision Floating Reliable) are C libraries which allow the user to reliably define arbitrary precision variables when needing to calculate quantities beyond the maximum allowed by the compiler[1]. ZKCM (Komplexezahl Complex Multiprecision) is a C++ extension of the GNU MP and MPFR libraries designed for complex matrix calculations and is used to accurately perform the singular-value decomposition of the kernel weight matrices.

For both the Backus-Gilbert and gluon propagator codes, we make use of the `gvar` Python package [135] for the propagation of statistical errors and correla-

---

[1]For C, this is typically `double` precision (64-bit) but most modern compilers also support `long double` as quadruple precision (128-bit) floating point.

tion through complex functions. GVar assumes that the data represents Gaussian-random variables, which is valid under the assumptions of the central limit theorem.

The gauge fixing algorithm we have used for the calculation of the gluon propagator in both the Coulomb and Landau gauges was created by J. Marques [96] for use with the FASTSUM Gen-2 ensembles, and was adapted in a minor way to support the Gen-2L ensembles in this work. The ensembles themselves are manipulated using the `lyncs.io` package[110] which enables the I/O of OpenQCD gauge field data directly in Python.